Long-Term Vulnerability Assessment and Adaptation Planning for the San Francisco Public Utilities Commission Water Enterprise

Technical Report 1: Weather Generator Module

Prepared for:

Water Research Foundation and San Francisco Public Utilities Commission

Prepared by:

University of Massachusetts Amherst, Hydrosystems Research Group

National Center for Atmospheric Research

November, 2018

Table of Contents

Purpose

This Technical Report describes the climate-weather generator (ClixWGen) and the background climate analysis that was performed to inform the development of the weather generator as part of the Long-Term Vulnerability Assessment and Adaptation Planning for the San Francisco Public Utilities Commission Water Enterprise. The weather generator described in this document is used to produce time series of temperature and precipitation at locations of weather stations used for hydrologic (Bay Area and Sierra Nevada) and demand (retail and wholesale service area) modeling. These output time series will help explore the effects of variations similar to observed historical conditions, as well as climate variability beyond the historical record due to changes in future temperature and precipitation. The weather generator is a component of the climate stress test, which creates time series of temperature and precipitation that systematically sample the plausible climate conditions that may occur in the future. It is specifically designed to create equally probable time series that represent realizations of natural variability. Output from this module will be used to evaluate effects of warmer temperatures and associated changes in snowmelt on reservoir operations and assess impact of changes in frequency and magnitude of extreme weather events. This module enables evaluation of the Regional Water System performance over a range of possible drought and variability sequences. The tool will develop drought sequences stochastically based on observed variability and use our recently developed method for ranking their severity and recurrence interval.

1. Introduction

Climate change is having a profound impact on California water resources, as evidenced by changes in temperature, precipitation, snowpack, and river flows (Vicuna et al. 2007). These changes are expected to continue in the future, with more precipitation expected to fall as rain instead of snow. This potential change in weather patterns will exacerbate both drought and flood risks and add additional challenges for water supply reliability (Sicke et al. 2013). These accelerated changes in climate underscore the need for climate change risk assessment and adaptation. Vulnerability-based approaches to climate change risk assessment are increasingly desired. In a bottom-up or vulnerability-based approach, performance of system is systematically evaluated over a range of plausible future climates to identify climatic conditions that can cause a system to fail (Brown et al. 2012). This is in contrast to scenario-based approaches where system performance is only tested for a given set of climate model projections that may not necessarily highlight a system's vulnerabilities, and where results are contingent on the projections and downscaling approach that happen to be used. In the bottom-up approach, once the system's vulnerabilities to climate states have been identified, then the level of concern associated with those climate states can be assessed using climate projections (e.g., general circulation models or GCMs), historical observations or palaeoclimatological simulations. This separation of the articulation of system response to climate using climate stress testing from the use of GCM projections of future climate conditions allows a comprehensive understanding of the effects of climate changes on the water resource system. When projections of future climate conditions are updated based on the best scientific understanding, new downscaling method, etc., the expected risk can be updated using the new climate information without having to repeat the entire model simulations and assessment.

Stochastic weather generators (SWGs) are mathematical algorithms that produce long series of synthetic weather data at desired spatial and temporal resolution. The parameters of the model are conditioned on existing meteorological records to ensure that the characteristics of historical weather emerge in the daily stochastic process. Weather generators provide various functions in water resources management studies such as extending meteorological records (Richardson 1985); supplementing weather data in a region of data scarcity (Hutchinson 1995); disaggregating seasonal hydroclimatic forecasts (Wilks 2002); and downscaling coarse, long-term climate projections to fine resolution, daily data need in climate impact studies (Kilsby et al. 2007). SWGs can also be used to perform exhaustive assessments of a system's vulnerability to climate conditions across multiple temporal scales, including changes in mean climate and variability (Steinschneider and Brown 2013). SWGs can be used to produce a new realization of a time series of weather variables that exhibit the same statistics as the original historical record, thus producing an ensemble of time series that samples the historical or "natural" variability. By incrementally manipulating one or more parameters in a weather generator, one can simulate many climate scenarios that exhaustively explore potential futures that exhibit slight differences in nuanced climate characteristics, such as the intensity and frequency of daily precipitation, the serial correlation of extreme heat days, or the recurrence of long-term droughts.

CliWxGen is developed to support bottom-up vulnerability assessment of the San Francisco Public Utilities Commission (SFPUC) Regional Water System (RWS) to different aspects of climate variability and change. The weather generation process using CliWxGen consists of a number of subsequent phases. In the first phase, a large ensemble of new realizations of historical climate record to sample the natural (stochastic) climate variability in the region. This first step is done using a wavelet autoregressive model (WARM) to reproduce a time series of climate variables exhibiting a similar spectral structure (low-frequency variability) to the observed data. In the second phase, the simulated ensemble of climate realizations are perturbed to alter the historical climate characteristics and to represent possible long-term changes in future climate both uniformly and differentially across space and time. This approach allows for an assessment beyond the traditional methods of climate sensitivity analysis through exhaustive exploration and systematic sampling of climate uncertainties to identify future conditions that may lead to vulnerable outcomes regarding system performance.

There are some important considerations associated with development of weather generators. Weather generators should be able to replicate and perturb climate variability important for a given system reasonably. For instance, for this vulnerability assessment, low-frequency variability (Dettinger and Cayan, 2014) that has been identified in the literature as a characteristic of regional climate needs to be replicated. Furthermore, given the geographic and topographic differences in the sources of water for the SFPUC, the weather generator needs to produce synthetic time series where the covariance structure between weather variables and across sites is maintained.

2. Historical Climate of the Regional Water System

System Description

A preliminary step for the weather generator development is gaining a good understanding of the climatology of the study area. This typically includes analyses of past trends in the relevant climate variables such as precipitation and temperature, spatial and temporal correlations across different climate variables and meteorological stations, and low-frequency variability or persistence in annual precipitation, which may result from atmospheric teleconnections such El Niño–Southern Oscillation (ENSO).

The SFPUC RWS consists of three distinct regions, which differ based on their climatological characteristics (Figure 1). These are:

- *Upcountry region*, consisting of Hetch Hetchy, Eleanor, and Cherry Valley watersheds. Hetch Hetchy reservoir is located in this region provides about 85% of the SFPUC's total water supply.
- *Peninsula region*, consisting of two reservoirs, Crystal Springs and San Andreas that collect runoff from the San Mateo Creek watershed.
- *East Bay region*, consisting of two reservoirs, San Antonio and Calaveras, which collect water from the San Antonio Creek, Upper Alameda Creek, and Arroyo Hondo watersheds in the Alameda County. San Antonio Reservoir also receives water from the Upcountry region.

Together, these watersheds and reservoirs provide high-quality municipal drinking water to the SFPUC region. The East Bay and Peninsula watersheds, collectively referred to as the Bay Area watersheds, exhibit a similar climatology that is significantly different from the Upcountry watersheds.

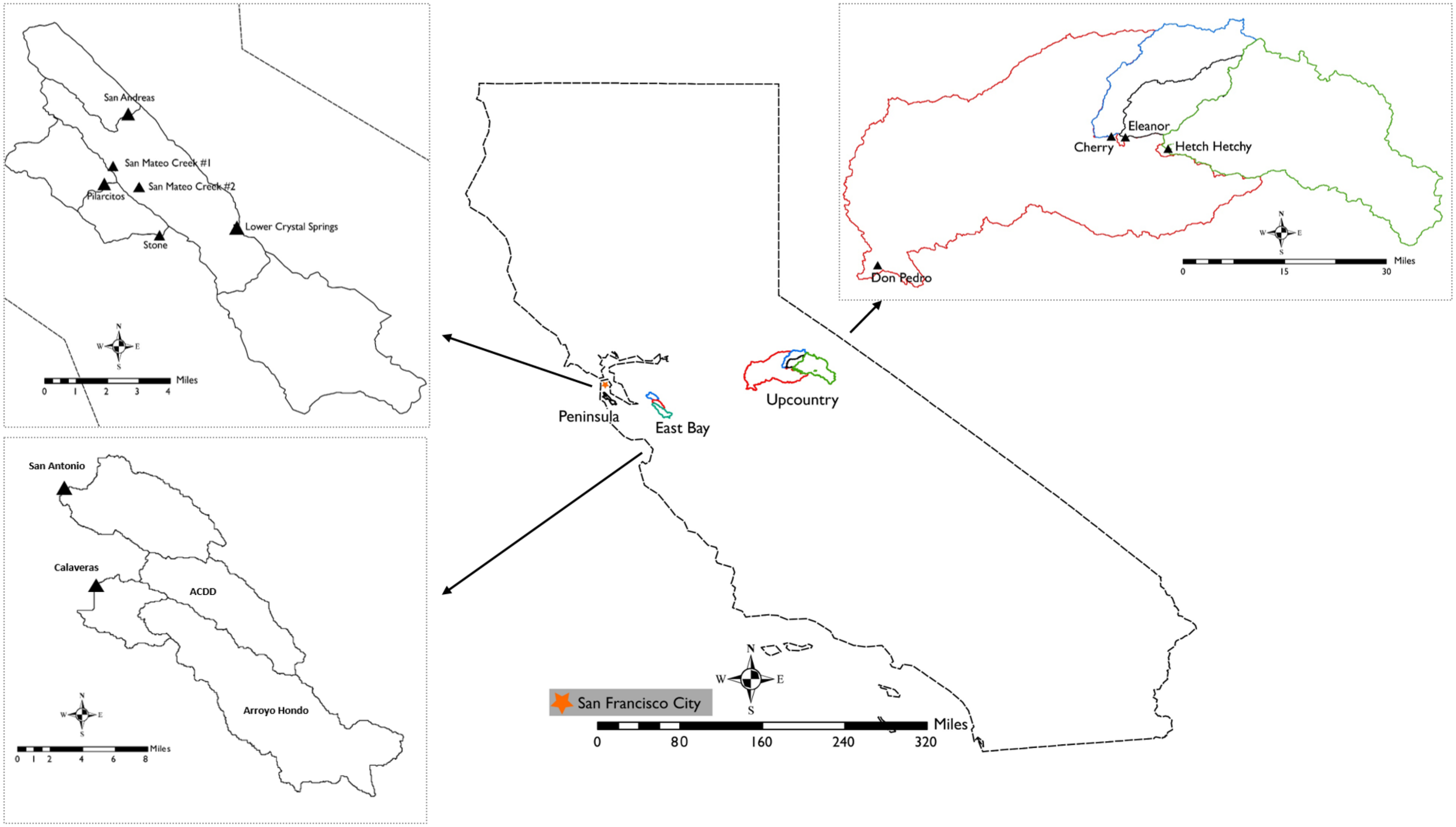

Figure 1. Map of SFPUC RWS showing the watersheds in the Upcountry, Eastbay, and Peninsula regions

2.1. Meteorological Stations

The meteorological data considered for this study includes daily time-series of precipitation from thirty gages and daily time-series of minimum and maximum temperature from twenty-two gages. These climate data come from a number of different agencies and institutions including SFPUC, California Department of Water Resources (CADWR), the National Weather Services (NWS), Alameda County Water District (ALWD), East Bay Regional Park District (EBRD), and Tuolumne Utilities District (TUD), and Pacific Gas and Electric (PG&E).

Error! Reference source not found. and three display the geographic locations of these precipitation and temperature gage across the Peninsula, Eastbay and Upcountry regions.

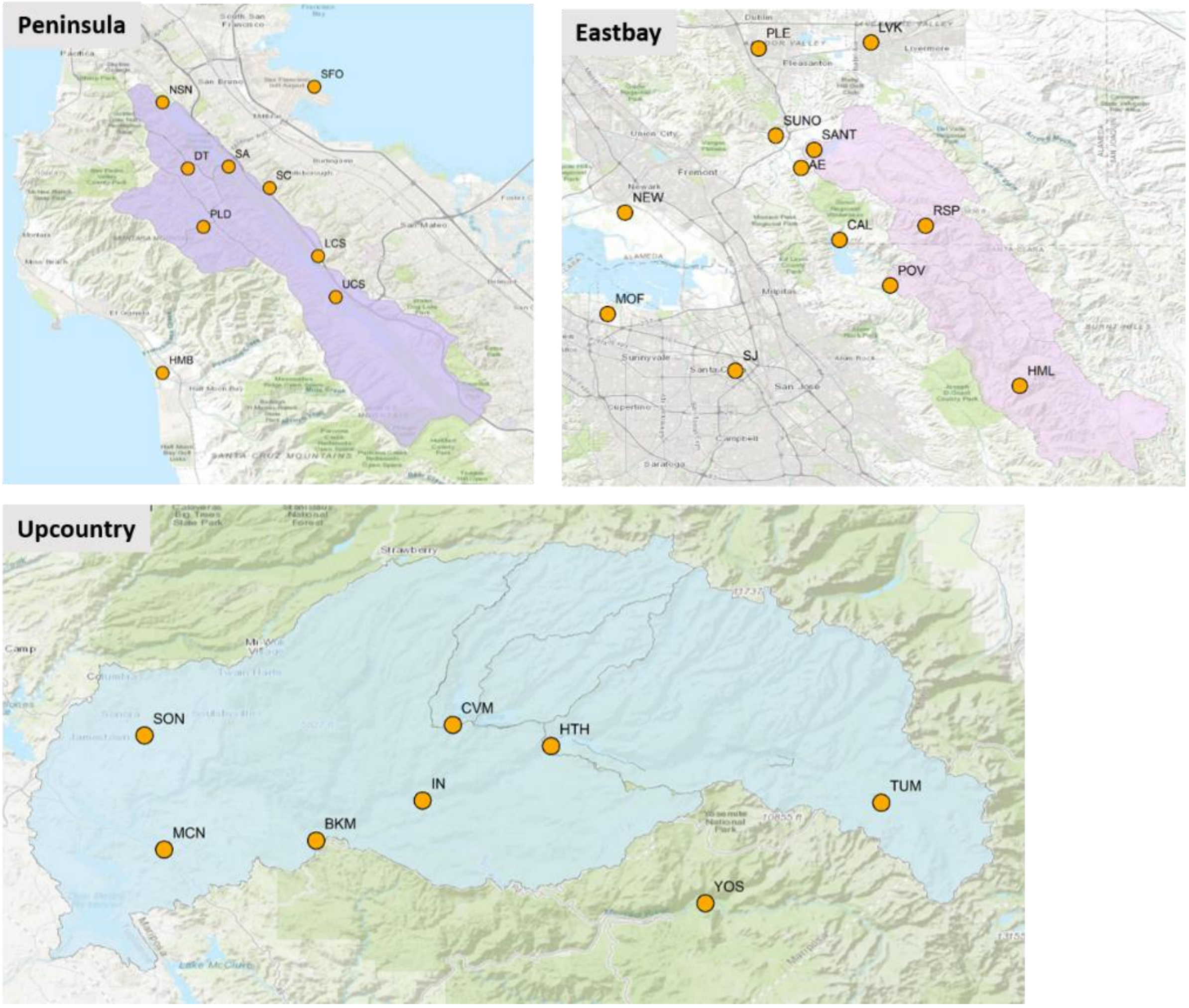

Figure 2. Precipitation gage locations in the SFPUC RWS across the Peninsula, Upcountry and Eastbay regions

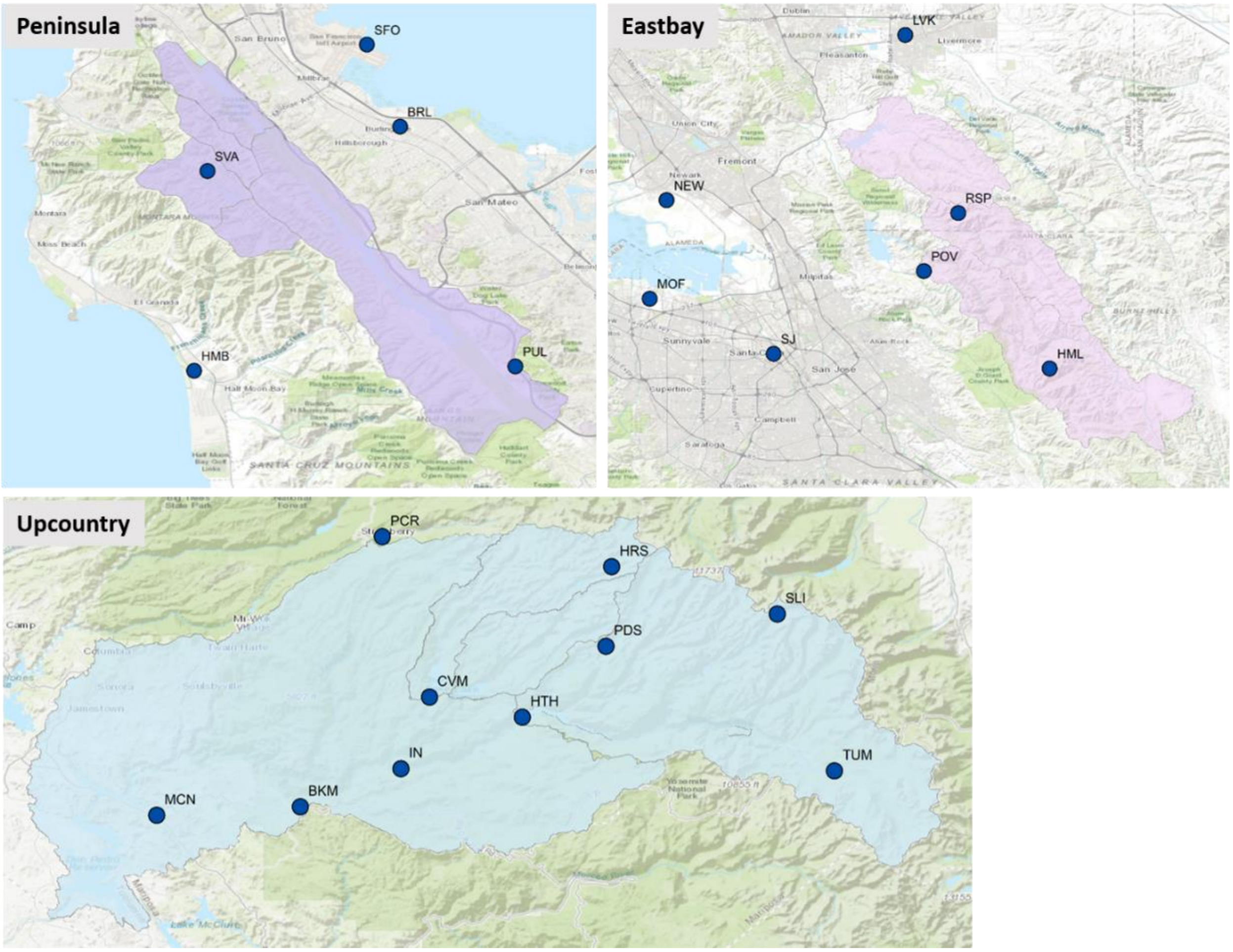

Figure 3. Temperature gage locations in the SFPUC RWS across the Peninsula, Upcountry and Eastbay regions

General information regarding these gage stations, including the geographic region and coordinates, altitude, and the starting and ending year of the data collection periods are presented in Table 1 (Precipitation) and Table 2 (Temperature) respectively. Descriptive statistics associated with the meteorological data from the same gages, including annual means, minimums, maximum and coefficient of variations are shown in Appendix I.

Table 1. Summary information for the precipitation gages in the SFPUC system

	Station	Label	Agency	Region	Latitude (°)	Longitude (°)	Altitude (ft.)	Start year	End year	Period (yrs)
1	Hetch Hetchy	HTH	SFPUC	Upcountry	37.948	-119.787	3858	1930	2017	87
2	Early Intake	IN	SFPUC	Upcountry	37.876	-119.957	2355	1930	2017	87
3	Moccasin	MCN	SFPUC	Upcountry	37.811	-120.299	938	1930	2017	87
4	Cherry Valley	CVM	SFPUC	Upcountry	37.976	-119.917	4765	1952	2017	65
5	Yosemite	YOS	NWS	Upcountry	37.740	-119.583	3985	1956	2017	61
6	Sonora	SON	TUD	Upcountry	37.962	-120.325	1750	1956	2017	61
7	Buck Meadows	BKM	SFPUC	Upcountry	37.823	-120.098	3200	1999	2017	18
8	Tuolumne Meadows	TUM	CADWR	Upcountry	37.873	-119.350	8600	1985	2017	32
9	Pilarcitos	PLD	SFPUC	Peninsula	37.548	-122.422	700	1909	2017	108
10	San Andreas Res	SA	SFPUC	Peninsula	37.579	-122.409	452	1908	2017	109
11	Lower Crystal Springs	LCS	SFPUC	Peninsula	37.533	-122.363	424	1915	2017	102
12	Upper Crystal Springs	UCS	SFPUC	Peninsula	37.512	-122.354	373	1908	2017	109
13	Sawyer Camp	SC	SFPUC	Peninsula	37.568	-122.388	344	1979	2017	38
14	North San Andreas	NSN	SFPUC	Peninsula	37.612	-122.443	617	1979	2017	38
15	Davis Tunnel	DT	SFPUC	Peninsula	37.578	-122.430	758	1979	2017	38
16	Half Moon Bay	HMB	NWS	Peninsula	37.473	-122.443	27	1939	2017	78
17	San Antonio R	SANT	SFPUC	East Bay	37.577	-121.846	498	1968	2017	49
18	Calaveras	CAL	SFPUC	East Bay	37.488	-121.821	822	1915	2017	102
19	Alameda East Portal	AE	SFPUC	East Bay	37.559	-121.859	334	1987	2017	30
20	Sunol	SUNO	SFPUC	East Bay	37.591	-121.884	242	1907	2017	110
21	Poverty	POV	SFPUC	East Bay	37.443	-121.771	2066	1998	2017	19
22	Rose Peak	RSP	EBRP	East Bay	37.502	-121.736	3060	1995	2017	22
23	Livermore Airport	LVK	NWS	East Bay	37.683	-121.790	437	-	2017	-
24	San Jose	SJ	NWS	East Bay	37.359	-121.924	51	1998	2017	19
25	Mt Hamilton	HML	NWS	East Bay	37.344	-121.643	4206	1948	2017	69
26	San Francisco Int. Airport	SFO	NWS	Peninsula	37.620	-122.365	8	1945	2017	72
27	Fremont	FRE	ACWD	East Bay	-	-	-	1871	2017	146
28	Moffett Federal Airfield	MOF	NWS	South Bay	37.415	-122.050	32	1945	2017	72
29	Newark	NEW	NWS	East Bay	37.515	-122.033	10	1942	2017	75
30	Pleasanton	PLE	SFPUC	East Bay	37.677	-121.901	-	1914	2001	87

Table 2. Summary information for the temperature gages in the SFPUC system

	Station	Label	Agency	Region	Latitude (°)	Longitude (°)	Altitude (ft.)	Start year	End year	Period (yrs)
1	Hetch Hetchy	HTH	SFPUC	Upcountry	37.948	-119.787	3858	1930	2017	87
2	Early Intake	IN	SFPUC	Upcountry	37.876	-119.957	2355	1930	2017	87
3	Moccasin	MCN	SFPUC	Upcountry	37.811	-120.299	938	1930	2017	87
4	Cherry Valley	CVM	SFPUC	Upcountry	37.976	-119.917	4765	1952	2017	65
5	Buck Meadows	BKM	SFPUC	Upcountry	37.823	-120.098	3200	2005	2017	12
6	Tuolumne Meadows	TUM	CADWR	Upcountry	37.873	-119.350	8600	1985	2017	32
7	Paradise Meadow	PDS	CADWR	Upcountry	38.047	-119.670	7650.00	1987	2017	30
8	Slide Canyon	SLI	CADWR	Upcountry	38.092	-119.430	9200.00	2005	2017	12
9	Horse Meadows	HRS	CADWR	Upcountry	38.158	-119.662	8400.00	2005	2017	12
10	Pinecrest	PCR	PG&E	Upcountry	38.200	-119.983	5600.00	1996	2017	21
11	Poverty	POV	SFPUC	East Bay	37.443	-121.771	2066	1998	2017	19
12	Rose Peak	RSP	EBRP	East Bay	37.502	-121.736	3060	1997	2017	20
13	Livermore Airport	LVK	NWS	East Bay	37.683	-121.790	437	1903	2017	114
14	San Jose	SJ	NWS	East Bay	37.359	-121.924	51	1998	2017	19
15	Spring Valley	SVA	SFPUC	Peninsula	37.563	-122.437	1075	1998	2017	19
16	Pulgas	PUL	SFPUC	Peninsula	37.475	-122.298	644	1997	2017	20
17	Half Moon Bay	HMB	NWS	Peninsula	37.473	-122.443	27	1939	2017	78
18	San Francisco Int. Airport	SFO	NWS	Peninsula	37.620	-122.365	8	1945	2017	72
19	Mt Hamilton	HML	NWS	East Bay	37.344	-121.643	4206	1948	2017	69
20	Moffett Federal Airfield	MOF	NWS	South Bay	37.415	-122.050	32	1945	2017	72
21	Burlingame	BRL	NWS	Peninsula	37.583	-122.350	10.00	1946	1978	32
22	Newark	NEW	NWS	East Bay	37.515	-122.033	10	1942	2017	75

As Table 1 and Table 2 show, available meteorological data from the temperature and precipitation gages vary substantially based on their length of records. Long time-series of daily meteorological data (e.g., 50 years or longer), which is useful to assess the regional climatology is available for only seventeen precipitation gages and nine temperature gages (Figure 4).

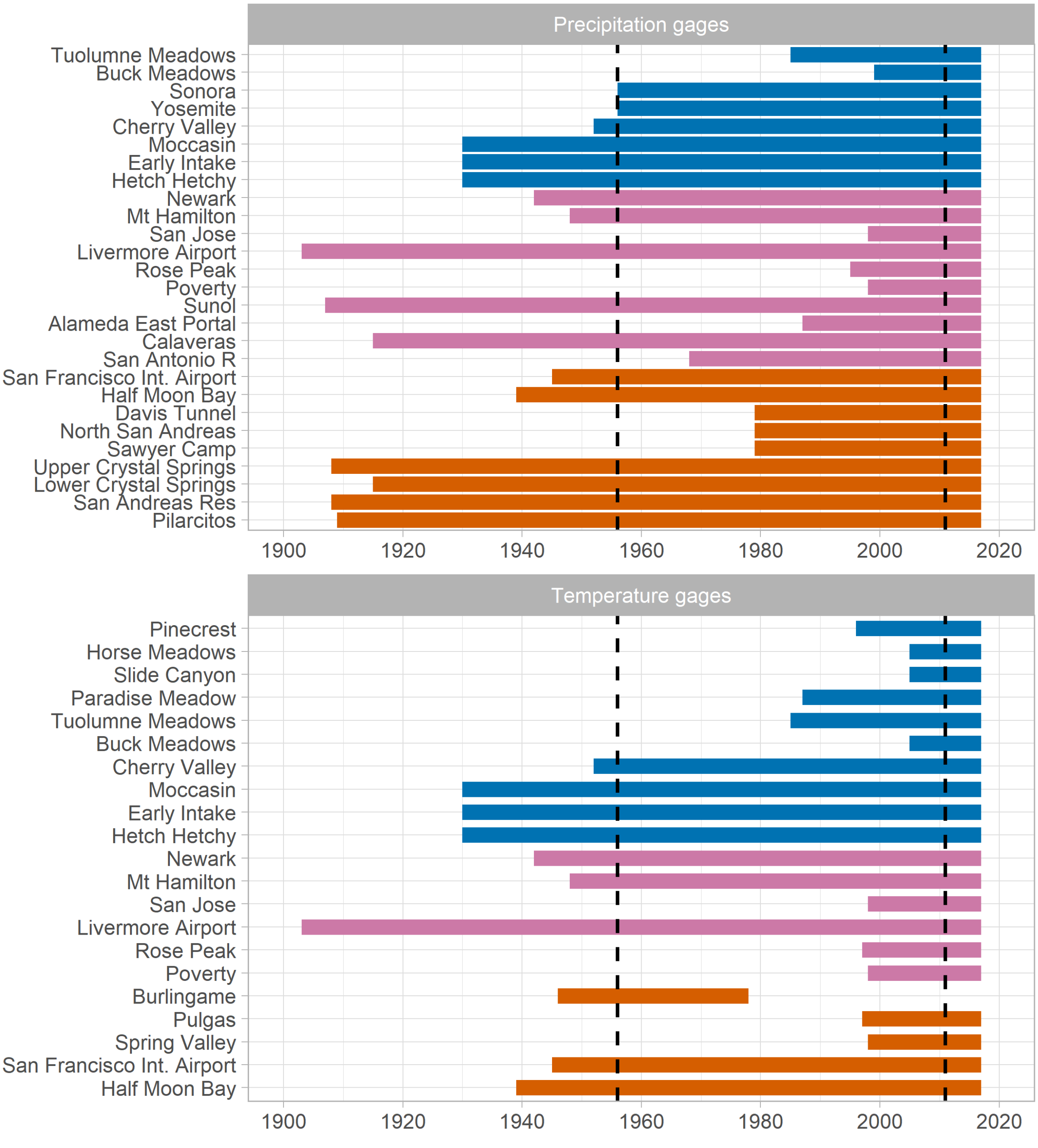

Figure 4. Length of records for the considered precipitation and temperature gages in study region. The stations in the Upcountry, Peninsula and East Bay regions are shown in blue, orange, and pink colors respectively. Vertical lines mark the analysis period from 1955-2011.

There are also substantial altitudinal differences between the gage stations across the three regions. The gage elevations range from about 1000 to 9200 feet in the Upcountry region, 0 to 4200 feet in East Bay region, and 0 to 1075 feet in the Peninsula region respectively (Figure 5).

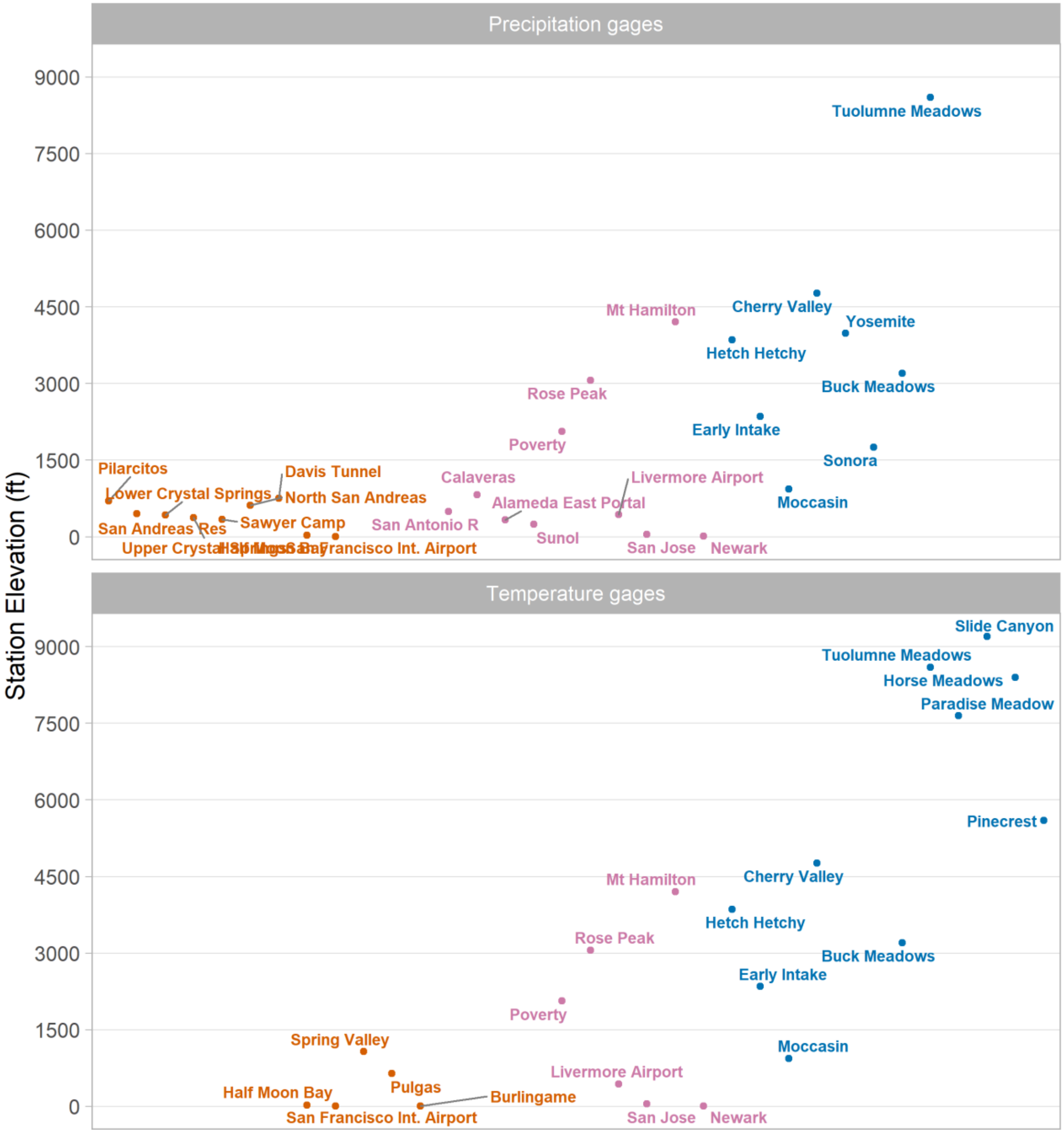

Figure 5. Station elevations for the precipitation and temperature metereological gage in the study region. The stations in the Upcountry, Peninsula and East Bay are shown in blue, orange, and pink colors respectively.

2.2. Spatial Correlations of Climate Variables

The correlational structure of daily precipitation and temperature is explored to understand the spatial heterogeneity across the three regions. The correlation analysis is carried out using the Pearson correlation coefficient, which measures the linear dependence between two time-series of climate variables from different locations. A Pearson's r-value of 1 means that the time-series move in perfect unison (total positive linear correlation), whereas a correlation of -1 means the time-series move in the complete opposite direction (total negative linear correlation). A correlation of 0 means no relationship. Due to the relatively short length of the common observation periods of climate variables, the spatial correlations analysis is carried over twenty-six out of thirty precipitation gages and fifteen out of twenty-two temperature gages.

Figure 6 shows the correlation matrix of daily precipitation from the twenty-six gage stations with sufficiently long records. A blue color indicates a high degree of correlation (Pearson's r ~ 0.5 to 1), whereas and a red color indicates a lower degree of correlation (Pearson's r ~ 0 to 0.5) between the weather variables from different stations. The gages from the same geographical region are highly correlated (Pearson's r > 0.75). Daily precipitation in the Peninsula and East Bay regions is also observed to correlate well (Pearson's r ~ 0.6 – 0.8). Stations in the Upcountry region are not correlated well with the stations in the Peninsula or East Bay regions although the correlations are still positive (Pearson's r ~ 0.2 - 0.3).

Similarly, Figure 7 displays the spatial correlations between daily temperatures from the fifteen gage stations. In contrast to the spatial correlations shown for precipitation (Figure 6), daily temperature is highly correlated within the study area across all three regions (Pearson's r > 0.8). The only exception is the Half Moon Bay (HMB), which is found to be less correlated with all the other stations (r > 0.65).

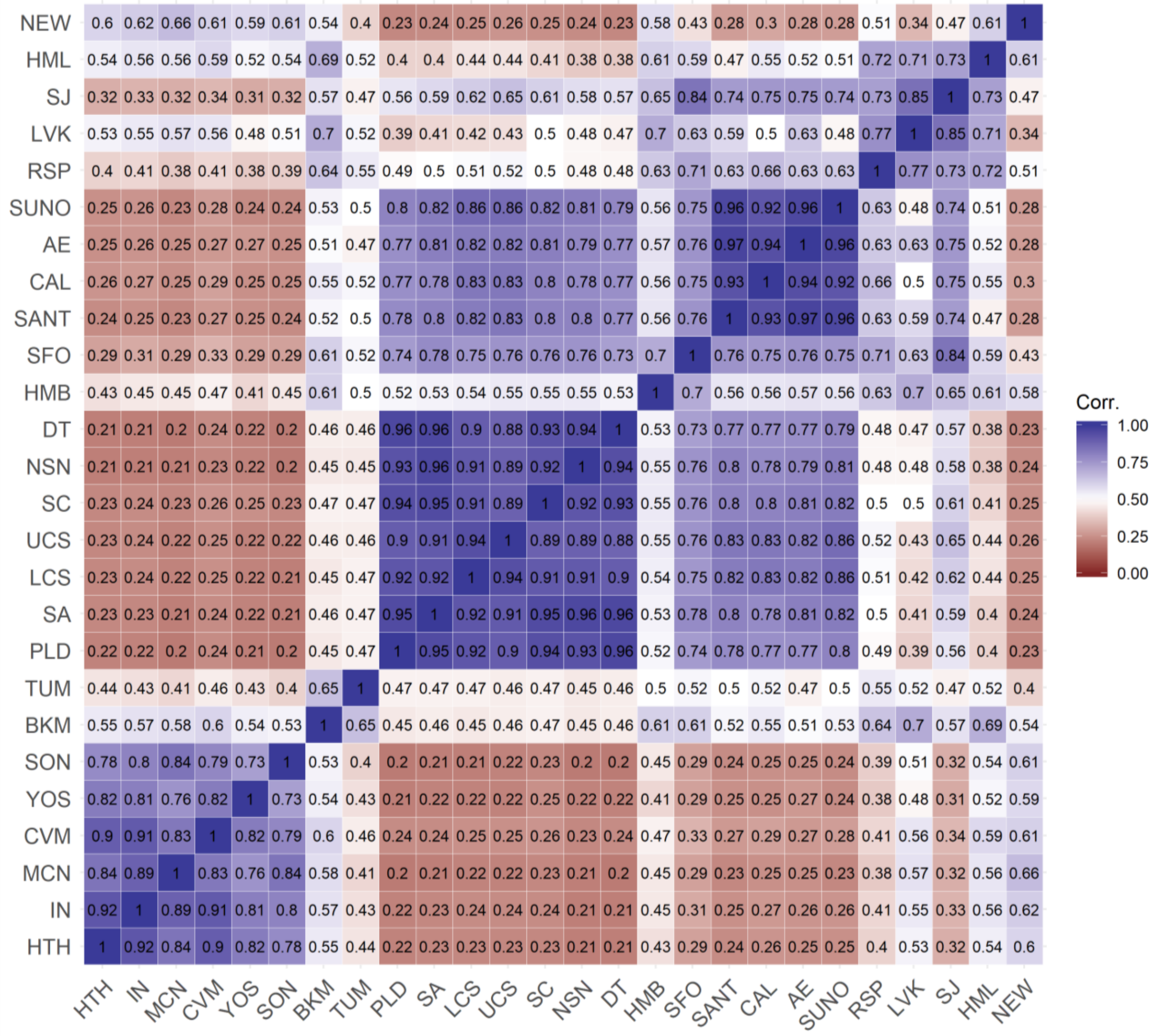

	HTH	IN	MCN	CVM	YOS	SON	BKM	TUM	PLD	SA	LCS	UCS	SC	NSN	DT	HMB	SFO	SANT	CAL	AE	SUNO	RSP	LVK	SJ	HML	NEW
NEW	0.6	0.62	0.66	0.61	0.59	0.61	0.54	0.4	0.23	0.24	0.25	0.26	0.25	0.24	0.23	0.58	0.43	0.28	0.3	0.28	0.28	0.51	0.34	0.47	0.61	1
HML	0.54	0.56	0.56	0.59	0.52	0.54	0.69	0.52	0.4	0.4	0.44	0.44	0.41	0.38	0.38	0.61	0.59	0.47	0.55	0.52	0.51	0.72	0.71	0.73	1	0.61
SJ	0.32	0.33	0.32	0.34	0.31	0.32	0.57	0.47	0.56	0.59	0.62	0.65	0.61	0.58	0.57	0.65	0.84	0.74	0.75	0.75	0.74	0.73	0.85	1	0.73	0.47
LVK	0.53	0.55	0.57	0.56	0.48	0.51	0.7	0.52	0.39	0.41	0.42	0.43	0.5	0.48	0.47	0.7	0.63	0.59	0.5	0.63	0.48	0.77	1	0.85	0.71	0.34
RSP	0.4	0.41	0.38	0.41	0.38	0.39	0.64	0.55	0.49	0.5	0.51	0.52	0.5	0.48	0.48	0.63	0.71	0.63	0.66	0.63	0.63	1	0.77	0.73	0.72	0.51
SUNO	0.25	0.26	0.23	0.28	0.24	0.24	0.53	0.5	0.8	0.82	0.86	0.86	0.82	0.81	0.79	0.56	0.75	0.96	0.92	0.96	1	0.63	0.48	0.74	0.51	0.28
AE	0.25	0.26	0.25	0.27	0.27	0.25	0.51	0.47	0.77	0.81	0.82	0.82	0.81	0.79	0.77	0.57	0.76	0.97	0.94	1	0.96	0.63	0.63	0.75	0.52	0.28
CAL	0.26	0.27	0.25	0.29	0.25	0.25	0.55	0.52	0.77	0.78	0.83	0.83	0.8	0.78	0.77	0.56	0.75	0.93	1	0.94	0.92	0.66	0.5	0.75	0.55	0.3
SANT	0.24	0.25	0.23	0.27	0.25	0.24	0.52	0.5	0.78	0.8	0.82	0.83	0.8	0.8	0.77	0.56	0.76	1	0.93	0.97	0.96	0.63	0.59	0.74	0.47	0.28
SFO	0.29	0.31	0.29	0.33	0.29	0.29	0.61	0.52	0.74	0.78	0.75	0.76	0.76	0.76	0.73	0.7	1	0.76	0.75	0.76	0.75	0.71	0.63	0.84	0.59	0.43
HMB	0.43	0.45	0.45	0.47	0.41	0.45	0.61	0.5	0.52	0.53	0.54	0.55	0.55	0.55	0.53	1	0.7	0.56	0.56	0.57	0.56	0.63	0.7	0.65	0.61	0.58
DT	0.21	0.21	0.2	0.24	0.22	0.2	0.46	0.46	0.96	0.96	0.9	0.88	0.93	0.94	1	0.53	0.73	0.77	0.77	0.77	0.79	0.48	0.47	0.57	0.38	0.23
NSN	0.21	0.21	0.21	0.23	0.22	0.2	0.45	0.45	0.93	0.96	0.91	0.89	0.92	1	0.94	0.55	0.76	0.8	0.78	0.79	0.81	0.48	0.48	0.58	0.38	0.24
SC	0.23	0.24	0.23	0.26	0.25	0.23	0.47	0.47	0.94	0.95	0.91	0.89	1	0.92	0.93	0.55	0.76	0.8	0.8	0.81	0.82	0.5	0.5	0.61	0.41	0.25
UCS	0.23	0.24	0.22	0.25	0.22	0.22	0.46	0.46	0.9	0.91	0.94	1	0.89	0.89	0.88	0.55	0.76	0.83	0.83	0.82	0.86	0.52	0.43	0.65	0.44	0.26
LCS	0.23	0.24	0.22	0.25	0.22	0.21	0.45	0.47	0.92	0.92	1	0.94	0.91	0.91	0.9	0.54	0.75	0.82	0.83	0.82	0.86	0.51	0.42	0.62	0.44	0.25
SA	0.23	0.23	0.21	0.24	0.22	0.21	0.46	0.47	0.95	1	0.92	0.91	0.95	0.96	0.96	0.53	0.78	0.8	0.78	0.81	0.82	0.5	0.41	0.59	0.4	0.24
PLD	0.22	0.22	0.2	0.24	0.21	0.2	0.45	0.47	1	0.95	0.92	0.9	0.94	0.93	0.96	0.52	0.74	0.78	0.77	0.77	0.8	0.49	0.39	0.56	0.4	0.23
TUM	0.44	0.43	0.41	0.46	0.43	0.4	0.65	1	0.47	0.47	0.47	0.46	0.47	0.45	0.46	0.5	0.52	0.5	0.52	0.47	0.5	0.55	0.52	0.47	0.52	0.4
BKM	0.55	0.57	0.58	0.6	0.54	0.53	1	0.65	0.45	0.46	0.45	0.46	0.47	0.45	0.46	0.61	0.61	0.52	0.55	0.51	0.53	0.64	0.7	0.57	0.69	0.54
SON	0.78	0.8	0.84	0.79	0.73	1	0.53	0.4	0.2	0.21	0.21	0.22	0.23	0.2	0.2	0.45	0.29	0.24	0.25	0.25	0.24	0.39	0.51	0.32	0.54	0.61
YOS	0.82	0.81	0.76	0.82	1	0.73	0.54	0.43	0.21	0.22	0.22	0.22	0.25	0.22	0.22	0.41	0.29	0.25	0.25	0.27	0.24	0.38	0.48	0.31	0.52	0.59
CVM	0.9	0.91	0.83	1	0.82	0.79	0.6	0.46	0.24	0.24	0.25	0.25	0.26	0.23	0.24	0.47	0.33	0.27	0.29	0.27	0.28	0.41	0.56	0.34	0.59	0.61
MCN	0.84	0.89	1	0.83	0.76	0.84	0.58	0.41	0.2	0.21	0.22	0.22	0.23	0.21	0.2	0.45	0.29	0.23	0.25	0.25	0.23	0.38	0.57	0.32	0.56	0.66
IN	0.92	1	0.89	0.91	0.81	0.8	0.57	0.43	0.22	0.23	0.24	0.24	0.24	0.21	0.21	0.45	0.31	0.25	0.27	0.26	0.26	0.41	0.55	0.33	0.56	0.62
HTH	1	0.92	0.84	0.9	0.82	0.78	0.55	0.44	0.22	0.23	0.23	0.23	0.23	0.21	0.21	0.43	0.29	0.24	0.26	0.25	0.25	0.4	0.53	0.32	0.54	0.6

Figure 6. Spatial correlations in the observed daily precipitation across the gages. Values indicate the Pearson's r value for the given pair of gage stations in the x and y-axes. A Pearson's r-value of 1 means strong positive correlation between the stations, whereas a value of -1 means strong negative correlation. A Pearson's r-value of 0 means no linear correlation.

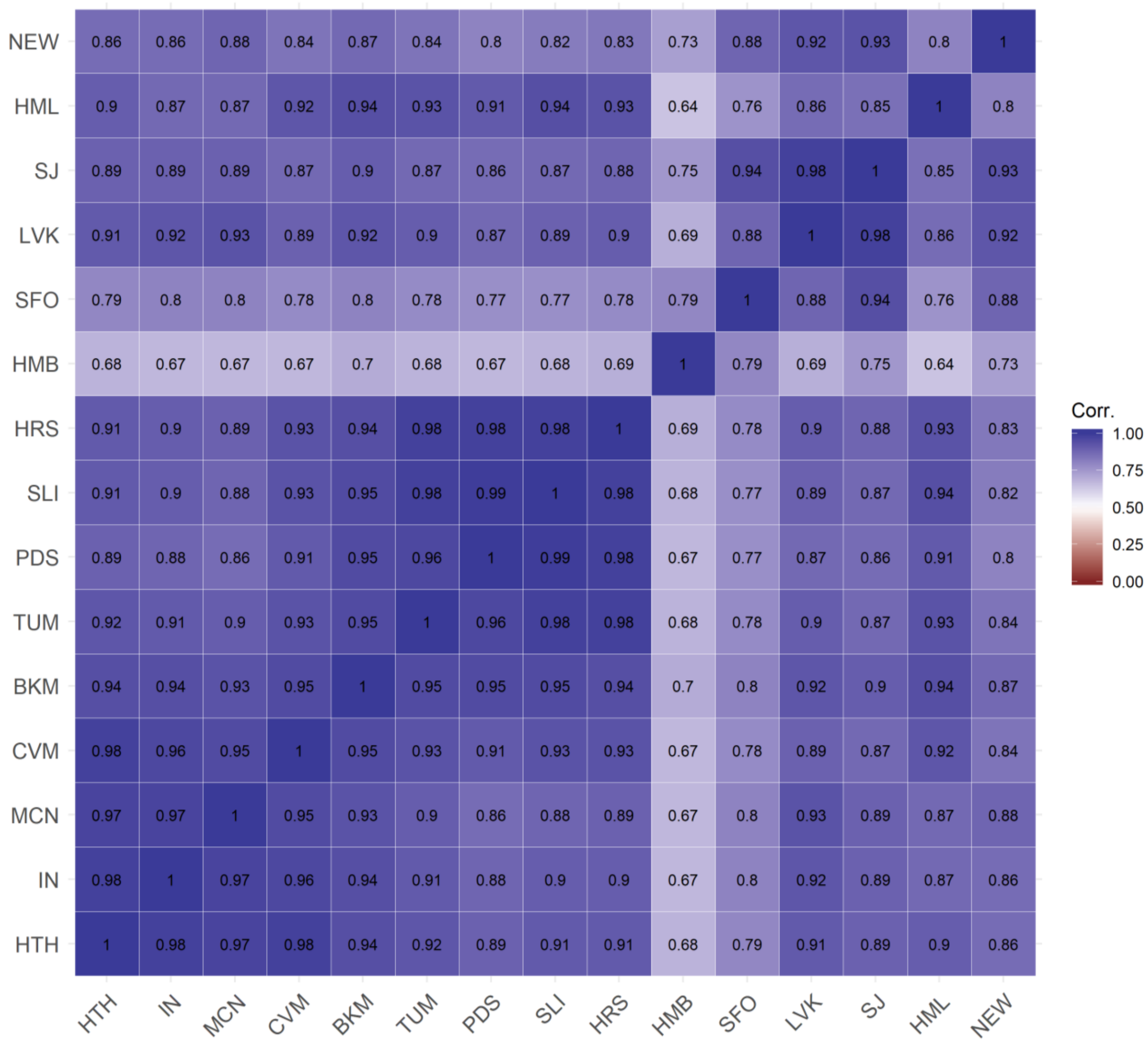

	HTH	IN	MCN	CVM	BKM	TUM	PDS	SLI	HRS	HMB	SFO	LVK	SJ	HML	NEW
NEW	0.86	0.86	0.88	0.84	0.87	0.84	0.8	0.82	0.83	0.73	0.88	0.92	0.93	0.8	1
HML	0.9	0.87	0.87	0.92	0.94	0.93	0.91	0.94	0.93	0.64	0.76	0.86	0.85	1	0.8
SJ	0.89	0.89	0.89	0.87	0.9	0.87	0.86	0.87	0.88	0.75	0.94	0.98	1	0.85	0.93
LVK	0.91	0.92	0.93	0.89	0.92	0.9	0.87	0.89	0.9	0.69	0.88	1	0.98	0.86	0.92
SFO	0.79	0.8	0.8	0.78	0.8	0.78	0.77	0.77	0.78	0.79	1	0.88	0.94	0.76	0.88
HMB	0.68	0.67	0.67	0.67	0.7	0.68	0.67	0.68	0.69	1	0.79	0.69	0.75	0.64	0.73
HRS	0.91	0.9	0.89	0.93	0.94	0.98	0.98	0.98	1	0.69	0.78	0.9	0.88	0.93	0.83
SLI	0.91	0.9	0.88	0.93	0.95	0.98	0.99	1	0.98	0.68	0.77	0.89	0.87	0.94	0.82
PDS	0.89	0.88	0.86	0.91	0.95	0.96	1	0.99	0.98	0.67	0.77	0.87	0.86	0.91	0.8
TUM	0.92	0.91	0.9	0.93	0.95	1	0.96	0.98	0.98	0.68	0.78	0.9	0.87	0.93	0.84
BKM	0.94	0.94	0.93	0.95	1	0.95	0.95	0.95	0.94	0.7	0.8	0.92	0.9	0.94	0.87
CVM	0.98	0.96	0.95	1	0.95	0.93	0.91	0.93	0.93	0.67	0.78	0.89	0.87	0.92	0.84
MCN	0.97	0.97	1	0.95	0.93	0.9	0.86	0.88	0.89	0.67	0.8	0.93	0.89	0.87	0.88
IN	0.98	1	0.97	0.96	0.94	0.91	0.88	0.9	0.9	0.67	0.8	0.92	0.89	0.87	0.86
HTH	1	0.98	0.97	0.98	0.94	0.92	0.89	0.91	0.91	0.68	0.79	0.91	0.89	0.9	0.86

Figure 7. Spatial correlations in the observed daily temperature across the gages. Values indicate the Pearson's r value for the given pair of gage stations in the x and y-axes. A Pearson's r-value of 1 means strong positive correlation between the stations, whereas a value of -1 means strong negative correlation. A Pearson's r-value of 0 means no linear correlation.

2.3. Trends in Observed Temperature and Precipitation

Across California, temperatures have shown a warming trend in the past century, with the state as a whole experiencing an increase of 1.1 to 2°F in mean temperature over the past century (i.e., from early 1900s to 2010s) (CA DWR 2015). Seasonal trends indicate a greater temperature increase in summer months than in winter months. Studies of precipitation trend in the state have yielded inconclusive results. While northern California shows increases in both mean annual precipitation and number of rainfall days, these increases are not statistically significant. Given these well-documented trends in the 20th century in California's climate (Killam et al. 2014), we conduct time-series analyses on the trends for annual and seasonal temperature and precipitation averages across the SFPUC watersheds to determine the nature of the trends (i.e. deterministic or stochastic), and understand the spatial and temporal variation in these trends.

In this study, we evaluate the annual and seasonal trends in minimum temperature (T_{min}) and maximum temperature (T_{max}) from the year 1956 to 2011. For the trend analysis, we only consider the stations with long-enough data, i.e., over the 56-year analysis period. These stations are: Half Moon Bay (HMB) and San Francisco Airport (SFO) for the Peninsula region; Mt Hamilton (HML), Livermore (LVK) and Newark (NEW) for the East Bay region; and Moccasin (MCN), Early Intake (IN), and Hetch Hetchy (HTH) for the Upcountry region respectively. For annual trend analysis, we average daily T_{min} and T_{max} values from each station over each water year (October to September). In the case of seasonal trend analysis, we average the same daily T_{min} and T_{max} values over a dry season (from April to September) and a wet season (from October to March).

Annual trends in T_{min} over the Upcountry, Peninsula, and East Bay regions is shown in Figure 8. A positive trend is observed in all three regions, with the East Bay trend being the strongest.

Annual trends in T_{max} over the same three regions are shown in Figure 9. Unlike T_{min}, the trend directions is not the same over the three regions, i.e., a positive trend is observed for Upcountry and Peninsula regions, whereas no major trend is detected for East Bay.

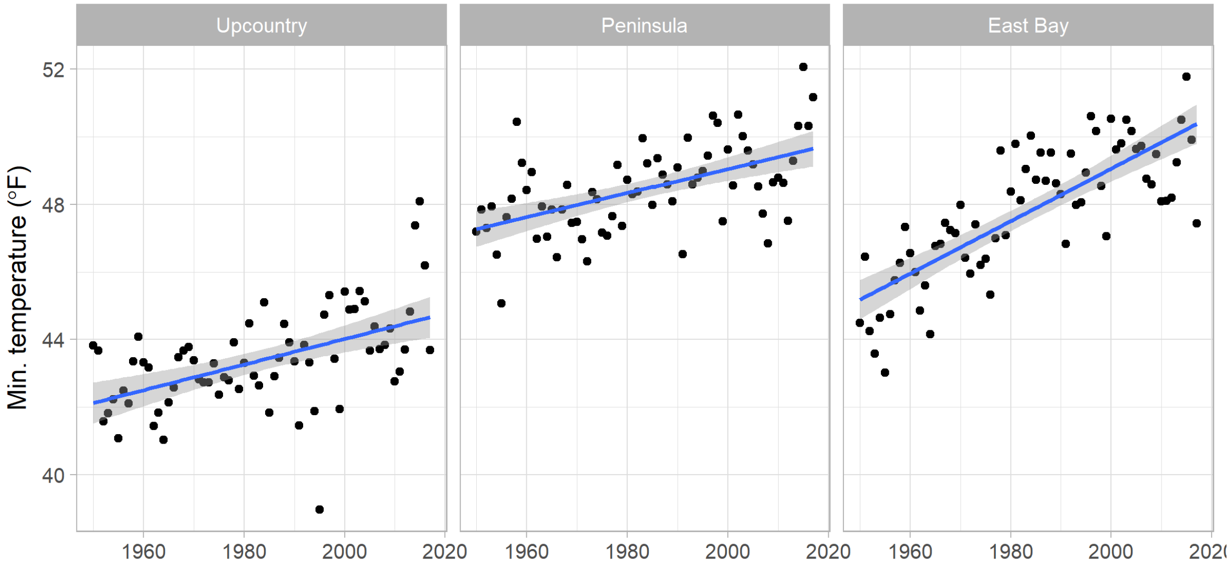

Figure 8. Annual averages of daily minimum temperatures (T_{min}) across the Upcountry, Peninsula, and East Bay regions. Results are shown for the analysis period from the year 1956 to 2011. The blue lines indicate the linear trend fitted to the underlying data. The shaded regions show the 95% confidence interval for the associated trend line.

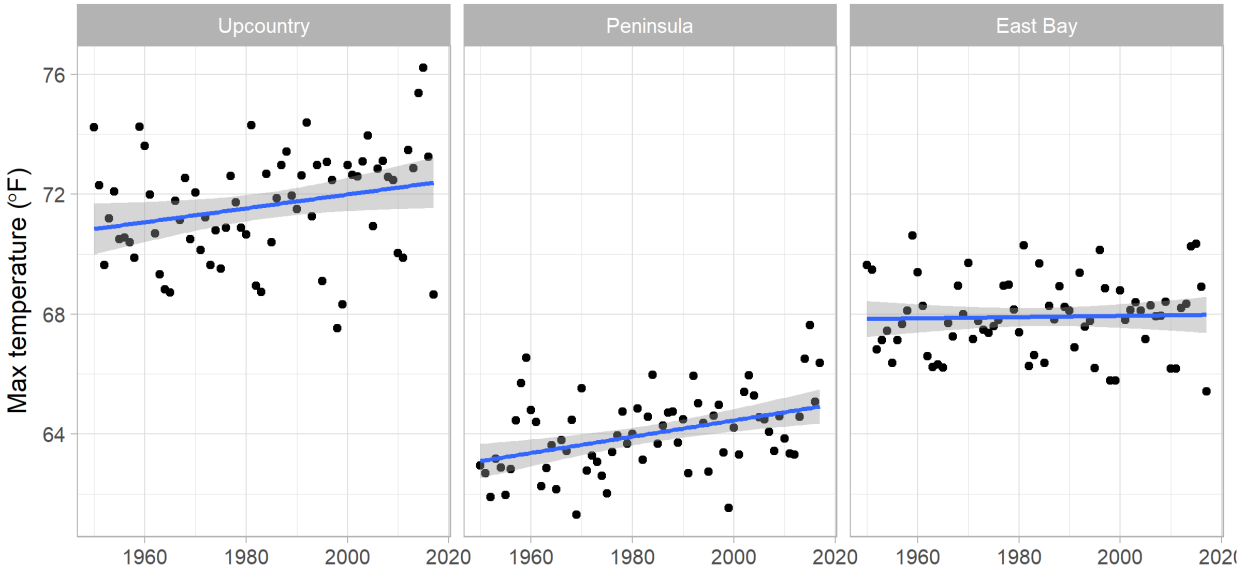

Figure 9. Annual averages of daily maximum temperatures (T_{max}) across the Upcountry, Peninsula, and East Bay regions. Results are shown for the analysis period from the year 1956 to 2011. The blue lines indicate the linear trend fitted to the underlying data. The shaded regions show the 95% confidence interval for the associated trend line.

Historical trends in T_{min} and T_{max} from the same gages are also evaluated for the dry and wet seasons separately for further analysis. T_{min} exhibits a positive trend in all three regions and both seasons (Figure 10). The strongest trends are observed in the East Bay region. In contrast, a positive T_{max} trend is observed for the Upcountry and Peninsula regions, whereas the direction of the trend for the East Bay region is unclear (Figure 11).

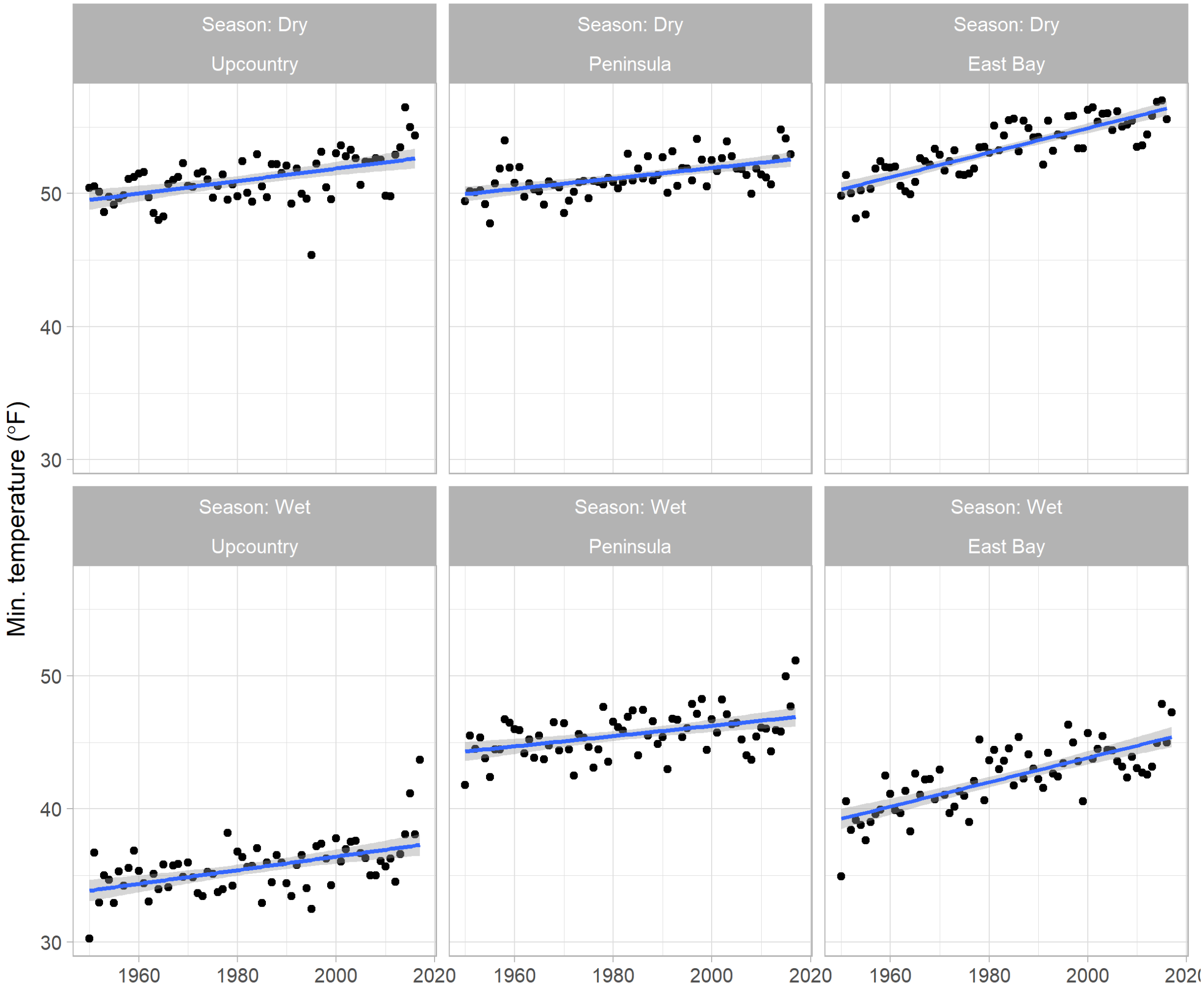

Figure 10. Dry season (April to September) and wet season (October to March) averages of daily minimum temperatures (T_{min}) across the Upcountry, Peninsula, and East Bay regions. Results are shown for the analysis period from the year 1956 to 2011. Blue lines show linear trend fitted over the data. Shaded regions show 95% confidence interval for the fitted trend line.

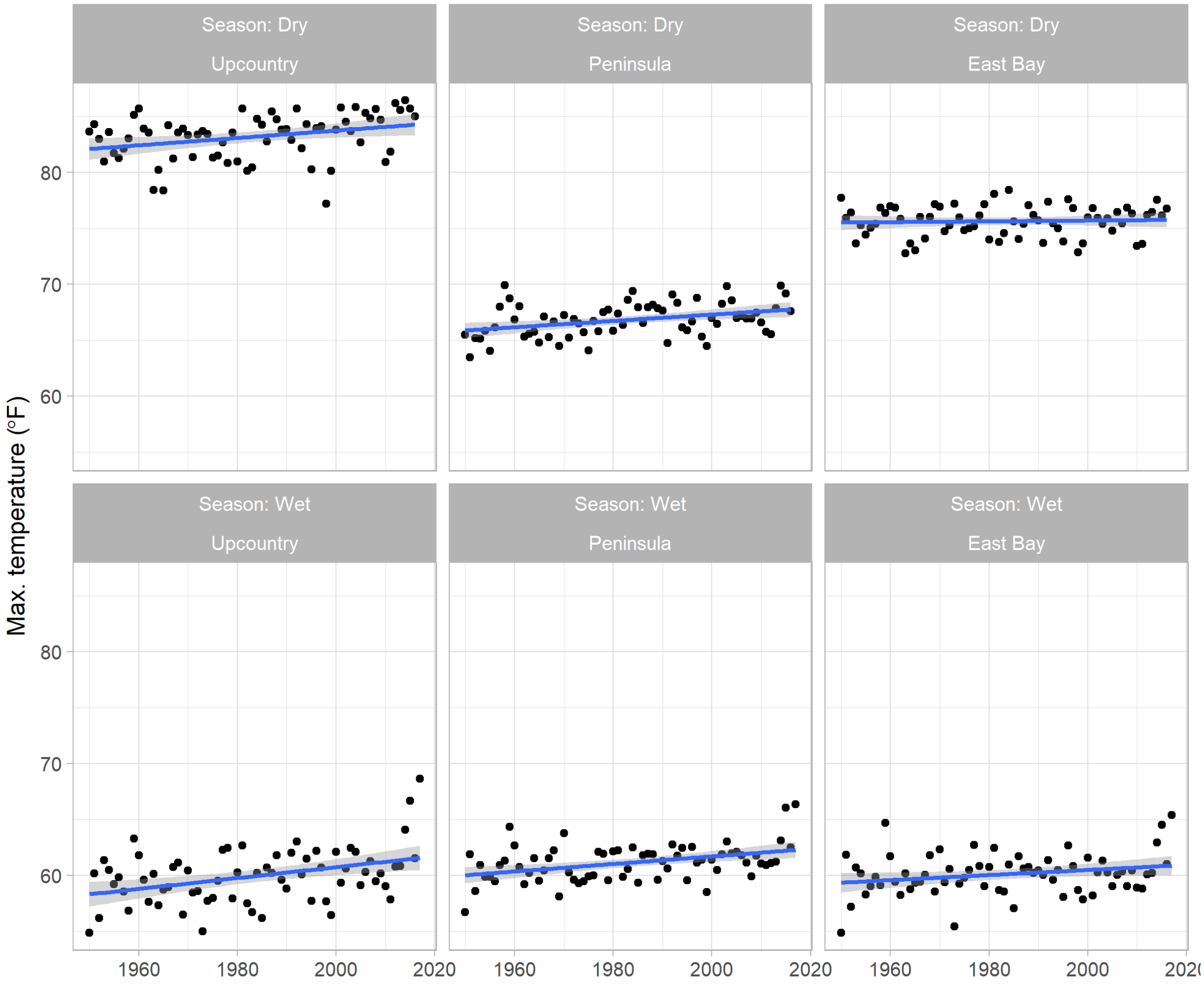

Figure 11. Dry season (April to September) and wet season (October to March) averages of daily maximum temperatures (T_{max}) across the Upcountry, Peninsula, and East Bay regions. Results are shown for the analysis period from the year 1956 to 2011. Blue lines show linear trend fitted over the data. Shaded regions show 95% confidence interval for the fitted trend line.

Finally, the annual and seasonal trends in daily T_{min} and T_{max} across the three regions are tested for statistical significance. For this purpose, we apply a nonparametric Mann Kendall trend test. Results from the Mann Kendall test show that all annual and seasonal trends previously identified for T_{min} are statistically significant, i.e., results in a p.value of less than 0.05. For $T_{max,}$ all trends identified for Upcountry and Peninsula regions are statistically significant (Table 3).

Table 3. Mann Kendall trend analysis results on annual and seasonal averages of daily T_{min} and T_{max} for the Upcountry, Peninsula, and East Bay regions. Results are based on the analysis period from the year 1956 to 2011. Columns 4 and 5 show the computed value of Man Kendall's tau statistic and the associated p-p-value of 0.05 or higher means that the null hypothesis (i.e., no trend) cannot be rejected.

Variable	Region	Season	tau	p-value
T_{min}	Upcountry	Dry	0.368	< 0.0001
		Wet	0.349	< 0.0001
		Annual	0.375	< 0.0001
	Peninsula	Dry	0.419	< 0.0001
		Wet	0.268	0.0013
		Annual	0.38	< 0.0001
	East Bay	Dry	0.618	< 0.0001
		Wet	0.542	< 0.0001
		Annual	0.565	< 0.0001
T_{max}	Upcountry	Dry	0.245	0.0035
		Wet	0.227	0.0064
		Annual	0.199	0.0165
	Peninsula	Dry	0.256	0.0023
		Wet	0.249	0.0027
		Annual	0.29	0.0005
	East Bay	Dry	0.038	0.6494
		Wet	0.123	0.1397
		Annual	0.062	0.4554

Overall, the T_{min} and T_{max} trends shown in Figure 8 through Figure 11 and in Table 3 are important to understand the possible range of changes in the spatial and temporal availability of water resources. The positive trends detected for the Upcountry region is especially important because it can affect the phase of precipitation and thus not only the volume but also the timing of flows into the Upcountry reservoirs (e.g. change in precipitation from snow to rain). Earlier analyses have shown that over the last several decades, rising temperatures in the Sierra Nevada and northern California trigger decreasing snowpack and earlier snowmelt (Barnett et al. 2008). For the SFPUC, these changes change water availability based on the structure of their water rights.

These results generally agree with the previous studies done by SFPUC, which concluded that the average daily temperatures have increased over the 79-year period from 1930 to 2008, but increases were not consistent. According to SFPUC, there are no apparent trends in average daily temperatures from about 1930 to 1960. From about 1960 to the present average daily temperatures at Hetch-Hetchy (HTH) and Cherry Valley (CHV) increase, but the increase is due to an increase in daily minimum temperatures. Daily maximum temperatures show no significant trend. Also, temperature records at Moccasin at 938 ft. Elevation do not show preferential increases in daily minimum temperatures relative to daily average or daily maximum temperatures. These findings by the SFPUC also similar to the results from other climatic studies in the region. Daily minimum temperatures in the Sierras have generally increased since 1900, with most of the increase occurring before 1930 and since 1960 (Behnke, R. 2011). Daily minimum winter temperatures in the Sierras increased over 1.5ºC (2.7ºF) between 1950 and 1999, while winter average daily maximum temperatures increased over 0.8ºC (1.4ºF) (Bonfils et al. 2008).

Similar trend analyses were also conducted for daily precipitation records across the different stations (see Appendix III, shown for each calendar month). None of the gages showed statistically significant trends in precipitation, a finding consistent with that in the existing literature (Killam et al. 2014).

2.4. Low-Frequency Variability in Annual Precipitation

The impact of large-scale climate patterns on precipitation in California is well documented (Dettinger et al. 1998). El-Nino Southern Oscillation (ENSO) has been shown to influence precipitation in the State, especially in Southern California. Evidence for the effect of ENSO on precipitation in the Delta region is inconclusive. Understanding these effects is important because they are typically the source of structured low frequency variability found in an observed weather time series. Since low frequency variability is a key factor in the occurrence of drought, preserving these effects is required to create a weather generator that reproduces the local climate conditions.

We investigate the historical annual precipitation record for presence of low frequency variability. In the common practice, there are two major methods for identifying persistence characteristics in time series: those which measure autocorrelation and those which perform a Fourier or wavelet analysis.

Autocorrelation-based methods have known limitations in reproducing the spectral signature of the time series, i.e., observed frequencies at specific wavelengths. Wavelet-based methods, on the other hand, are known to be better at preserving periodic or quasiperiodic behaviors seen in climate time-series (Kwon et al. 2007). In this work, we apply the latter method of wavelet analysis to assess the historical low-frequency variability of annual precipitation.

In simple terms, wavelet analysis or transform is a common tool for orthogonal decomposition of a time-series across the time-frequency domain. By applying a wavelet analysis, one can determine both the dominant modes of variability (low-frequency signals) and how those modes change over time. A continuous wavelet transform of a time-series is applied by estimating the wavelet power spectrum in the Fourier space using a discrete Fourier transform (for a detailed description, see Torrence and Compo (1988)).

Using wavelet analysis, one can explore the dominant periods of the time series and also determine how these dominant periods vary over time. For doing this, a wavelet analysis provides two outputs: a scale-integrated (or local) and a global (time-integrated) wavelet power spectrum. The former output (local spectrum) shows the variance of computed power coefficients over time, whereas the latter output (global spectrum) show the time-integrated variance of power coefficients at every scale. Global wavelet spectra are obtained by averaging the wavelet power over all local wavelet spectrum along the time axis.

Figure 12 shows the results from the wavelet analysis of annual precipitation for the Hetch Hetchy station in the Upcountry region. The local wavelet spectrum is shown on the left (Figure 12-a) and the global wavelet spectrum is shown on the right (Figure 12-b). The local wavelet spectrum shows significant power spectra at Fourier periods of about 5 and 15 years respectively (marked by the black contours), with respect to a 90% confidence level compared to "red noise". The temporal structure of the entire time series is assessed using by global wavelet spectrum that shows statistically significant low-frequency signals at Fourier periods of 11, 12 and 13, corresponding to frequency values of 12.1, 13.6 and 14.9 years respectively. A similar low-frequency variability pattern is also shown for the Pilarcitos gage station in the Peninsula region (Figure 13). In contrast to the results from Hetch Hetchy station, annual precipitation from the Pilarcitos station shows a relatively stronger multi-decadal variability signal at about 15 years.

The quasi-periodic 15-year cycle in the precipitation signal for the Hetch Hetchy (Figure 12) and Pilarcitos (Figure 13) stations has been identified previously in the literature but surprisingly has received little further attention. This signal is also visible in the paleo-records for the past 200 years, but not before that (Meko et al. 2014). The climatic patterns responsible for this signal are not currently well understood. In addition to the strong signal at 15-year frequency, results also show a 'bump' at about five years (Figure 13). While not significant at the 90% confidence level, this second signal is likely to be associated with the ENSO phenomena.

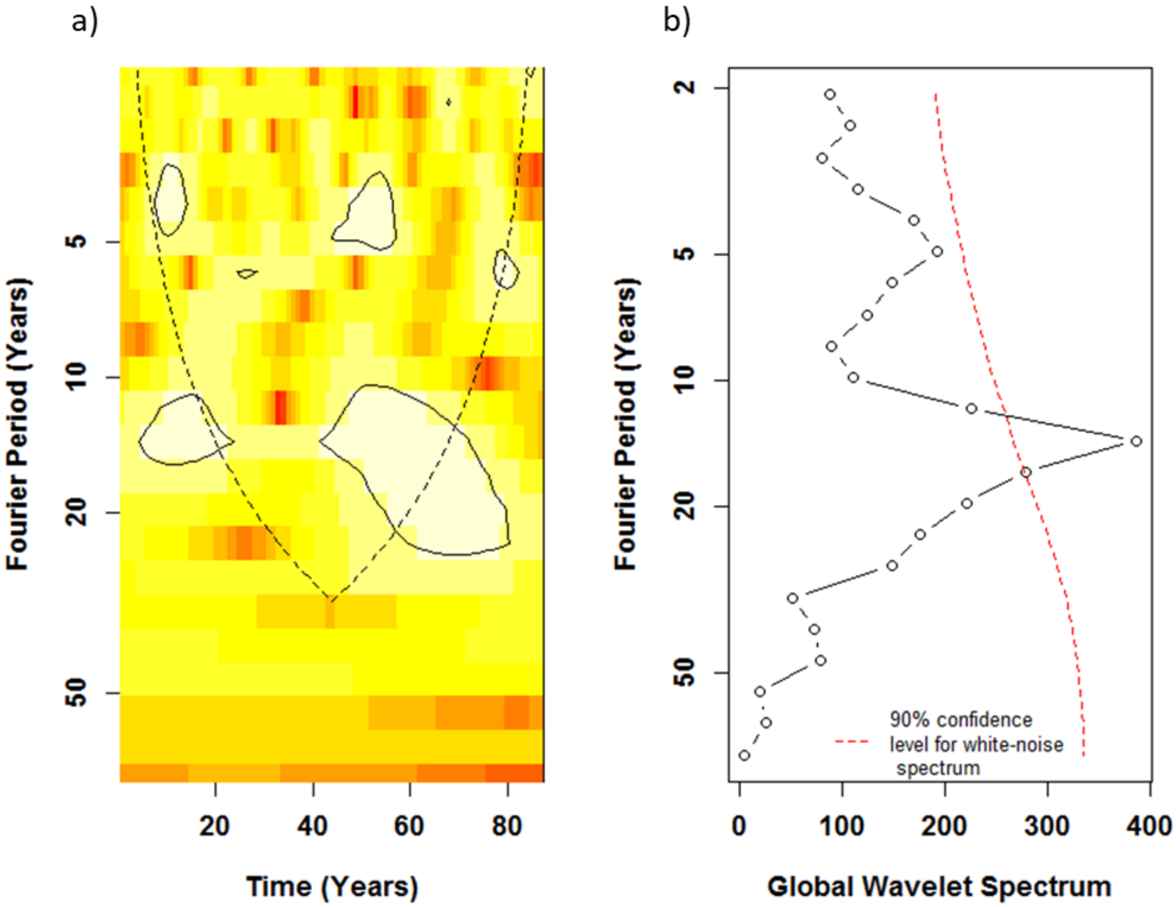

Figure 12. Wavelet analysis results for the Hetch Hetchy gage station (1930-2016): a) Local wavelet power spectrum plot for annual precipitation, b) Global wavelet spectrum plot for the same precipitation data. The local wavelet spectrum (a) displays the strength of each signal (shown in y-axis) locally around the given time (shown in x-axis). The strength of the signal increases in the color direction of from red to yellow. The black contours show the scales at which power spectra appear greater than 90% confidence for a white-noise process. The cross-hatched regions on either end indicate the "cone of influence," where edge effects become important. The global wavelet plot (b) summarizes the local information by removing the time-dimension. The dashed red line shows the significance level for the global wavelet spectrum.

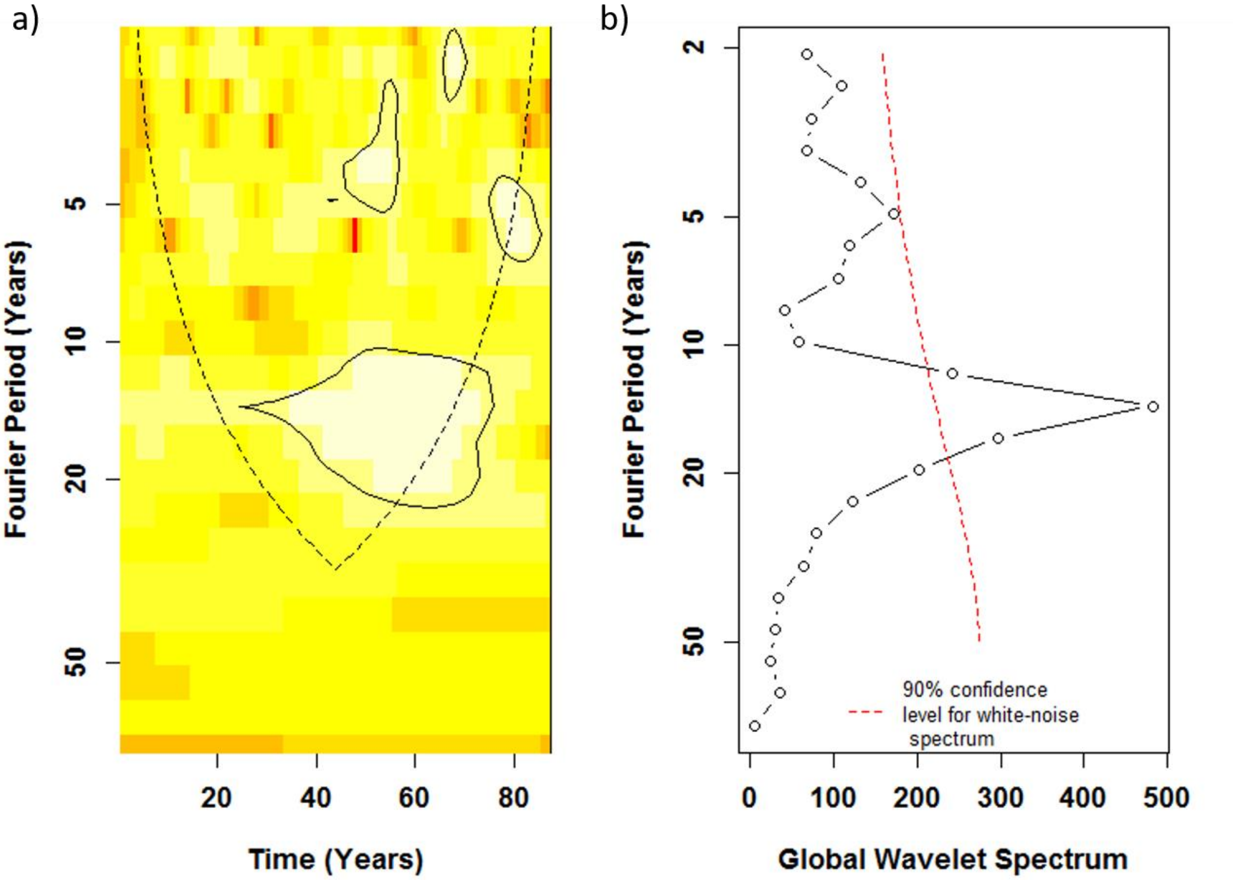

Figure 13. Wavelet analysis results for the Pilarcitos gage station (1930-2016): a) Local wavelet power spectrum plot for annual precipitation, b) Global wavelet spectrum plot for the same precipitation data. The local wavelet spectrum (a) displays the strength of each signal (shown in y-axis) locally around the given time (shown in x-axis). The strength of the signal increases in the color direction of from red to yellow. The black contours show the scales at which power spectra appear greater than 90% confidence for a white-noise process. The cross-hatched regions on either end indicate the "cone of influence," where edge effects become important. The global wavelet plot (b) summarizes the local information by removing the time-dimension. The dashed red line shows the significance level for the global wavelet spectrum.

3. Stochastic Weather Generator for the SFPUC system

This section provides a technical overview of the CliWxGen; the stochastic weather generator developed for the SFPUC RWS. Figure 14 illustrates the four major phases of the stochastic weather generator.

In Phase [1], the goal is to produce stochastic simulations of historical annual precipitation over the study region. If the climatology is homogenous within the study area, location-specific annual precipitation data can be area-averaged to obtain a single, representative time-series. However, if there are significant differences in climatology within the region like in this study, simple-averaging is not appropriate. Instead, a principal component analysis (PCA) can be applied to preserve the variability between different locations. The stochastic time-series generation is applied by a wavelet autoregressive model (WARM) on the represented annual precipitation series (Kwon et al. 2007). The WARM procedure first decomposes the annual series into significant low-frequency signals and the residual error term (noise). Each low-frequency component and the residual error is then simulated stochastically using best-fit linear autoregressive (AR) models. Finally, the simulated low frequency and noise component(s) are aggregated to obtain the simulated representative series of annual precipitation.

In Phase [2], simulated annual series from Phase [1] is disaggregated in time and space to obtain daily climate variables (precipitation, temperature, humidity, etc.) at all locations. This is done in three subsequent steps. First, the simulated annual series is inverted to its original scale and disaggregated spatially into annual precipitation series for all gage stations (Phase [2.1]). Next, the inverted series is disaggregated into monthly values using the method of fragments, a non-parametric resampling approach widely applied in climate simulation and disaggregation (Silva and Portela 2012) (Phase [2.2]). Finally, a k-nearest neighbors (KNN) resampling algorithm is used to further disaggregate the monthly precipitation series into daily values for all weather variables (i.e., precipitation, and minimum, average, and maximum temperature), while preserving the spatial and seasonal climate characteristics (In phase [2.3]). At the end of Phase 2, a complete set of climate realizations are obtained, which sample historical climate variability.

In Phase [3], the generated dataset of daily, multi-variable, multi-site climate realizations are reduced to a smaller set of realizations. This step is not mandatory in the stochastic weather generation process but is desired to reduce the computational challenges, i.e., due to the need to store and simulate large number of climate realizations in hydrosystem models. In this phase, we carefully select a small set of realizations that can span the initial variability range. This is done by first selecting criteria for ranking of the climate realizations (e.g., drought severity, extreme precipitation), and then subset from the initial set of realization using an appropriate statistical method such as sequent peak algorithm (Whateley et al., 2016).

In Phase [4], daily, multi-site, multi-variable climate realizations are perturbed to simulate a wide range of future climate changes. This is the final phase of the stochastic weather generator, where we perturb the underlying statistics of climate realizations to obtain a range of scenarios that represent both historical (natural) climate variability and a possible range of climate changes. This is done through different statistical procedures for the temperature and precipitation variables as explained next. For temperature variables (i.e., minimum, average, and maximum daily temperature), additive change factors are used to impose a linear increase over historical conditions, starting at zero and ending at the level of specified temperature increase (e.g., 4°C). For precipitation, multiplicative change factors are used to used to linearly perturb the historical mean values, starting from 1 and ending at the level of specified change (e.g., 10%).

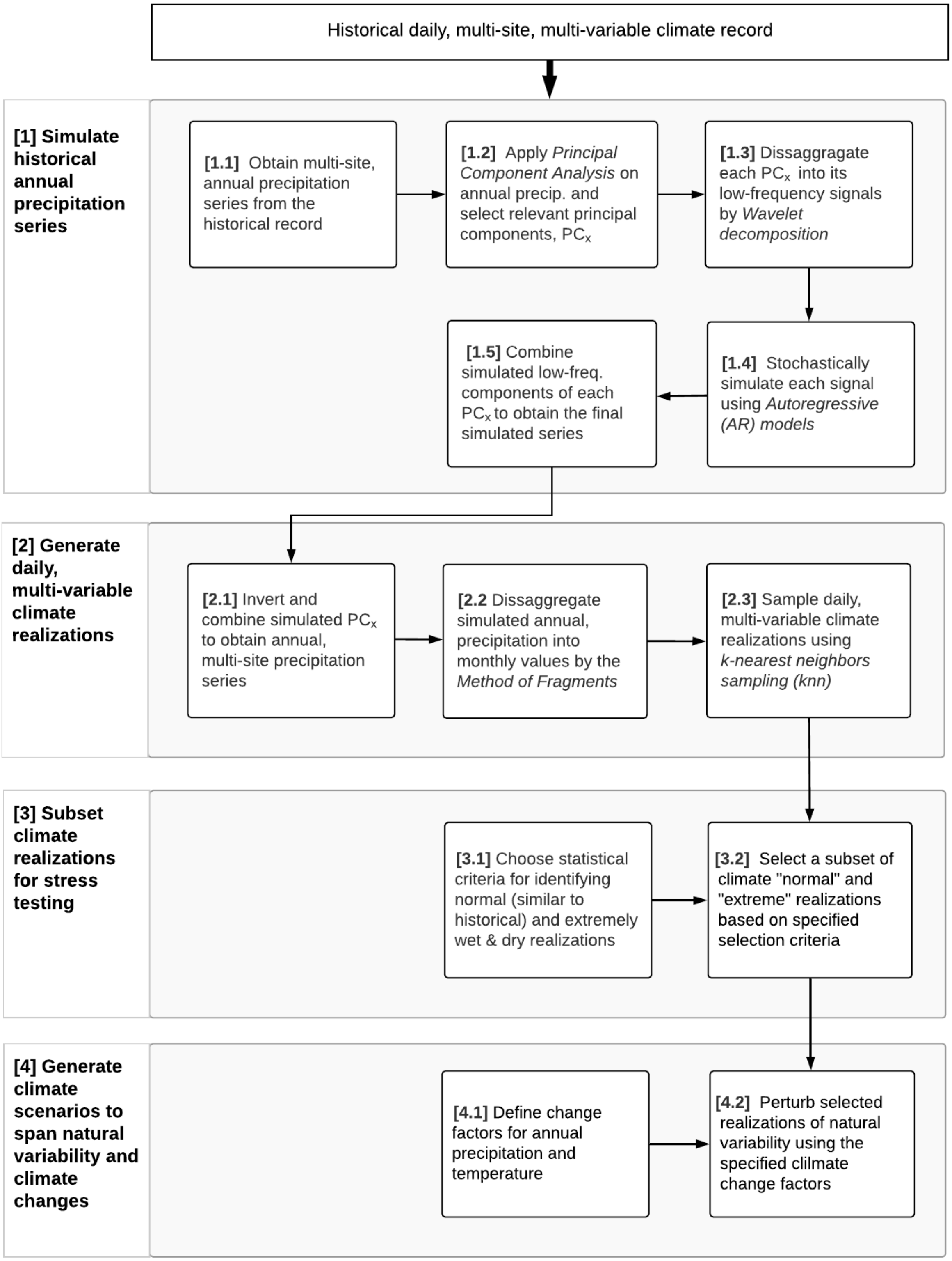

Figure 14. The flow chart of the stochastic weather generator developed for the SFPUC RWS

3.1. Historical Climate Data Used in the Weather Generator

When developing the weather generator, it is desirable to have a weather record that is long enough, e.g., 50 years or more, to provide a better representation of the climatological features such as trends and low-frequency variability. Also, the resampling techniques used in the stochastic weather generator (e.g., k-nearest neighbors) provides more diverse outcomes when the underlying input climate series is long enough. In most studies, long, continuous records of weather series may not be available, which poses a limitation for weather generator development. To circumvent this issue, weather generators often make use of gridded climate products, where corresponding time series of temperature of precipitation are available for large study regions. The wavelet analysis conducted on annual precipitation in Section 2.4 identified a low-frequency signal of about 15 years, which is considered to be as relatively long wavelength.

As previously shown in Section 2.1, the length of the observed daily temperature records varies across the stations, and only a limited number of stations provides long, continuous data. In order address this challenge, we investigate the suitability of using gridded climate data by comparing it with the local observations. As a gridded climate product, we evaluate the suitability of the CONUS dataset over the study region, covering a period of more than 100 years (from 1901 to 2008) at 6.25 km^2 spatial resolution (Livneh et al., 2013). The overlap of the CONUS grid cells with the precipitation and temperature gage stations are shown in Figure 16 and Figure 16 respectively.

We compare the daily precipitation from the CONUS dataset to the selected gage stations across the HTH and MCN stations in Upcountry, SFO, and HMB in Peninsula region, and LVK Airport and NEW in East Bay region (Figure 17). The gridded CONUS dataset is not able to replicate the observation precipitation adequately, especially for lower-magnitude precipitation events.

Similarly, Figure 18 and Figure 19 show a comparison of daily T_{min} and T_{max} values in the observed and gridded dataset for the same stations. Before the comparison, the gridded temperature series is adjusted by a lapse rate of 6.5 °F per km (3.56 °F per 1,000 feet) to account for the altitudinal differences between the gage stations and the average grid elevation (Maurer et al. 2002). For T_{min}, we observe a negative bias for Tuolumne station, and a positive bias for the Newark station (Figure 18). For T_{max}, we observed a slight negative bias for the SFO and HMB stations in the Peninsula region (Figure 19).

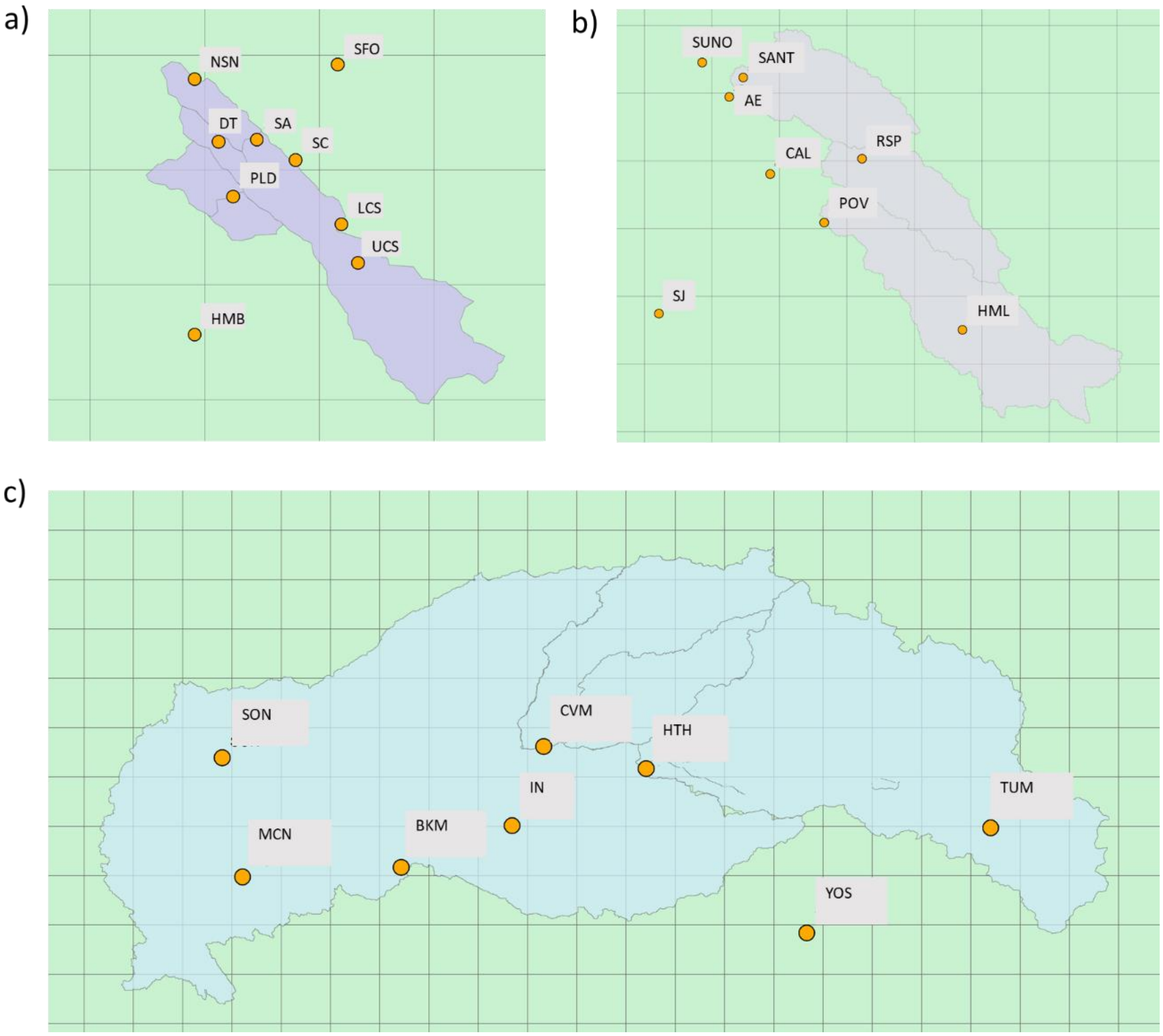

Figure 15. CONUS data grid cells (at 6.25 km^2 spatial resolution) and the precipitation gage stations in the SFPUC RWS: a) Peninsula region, b) East Bay region, and c) Upcountry region

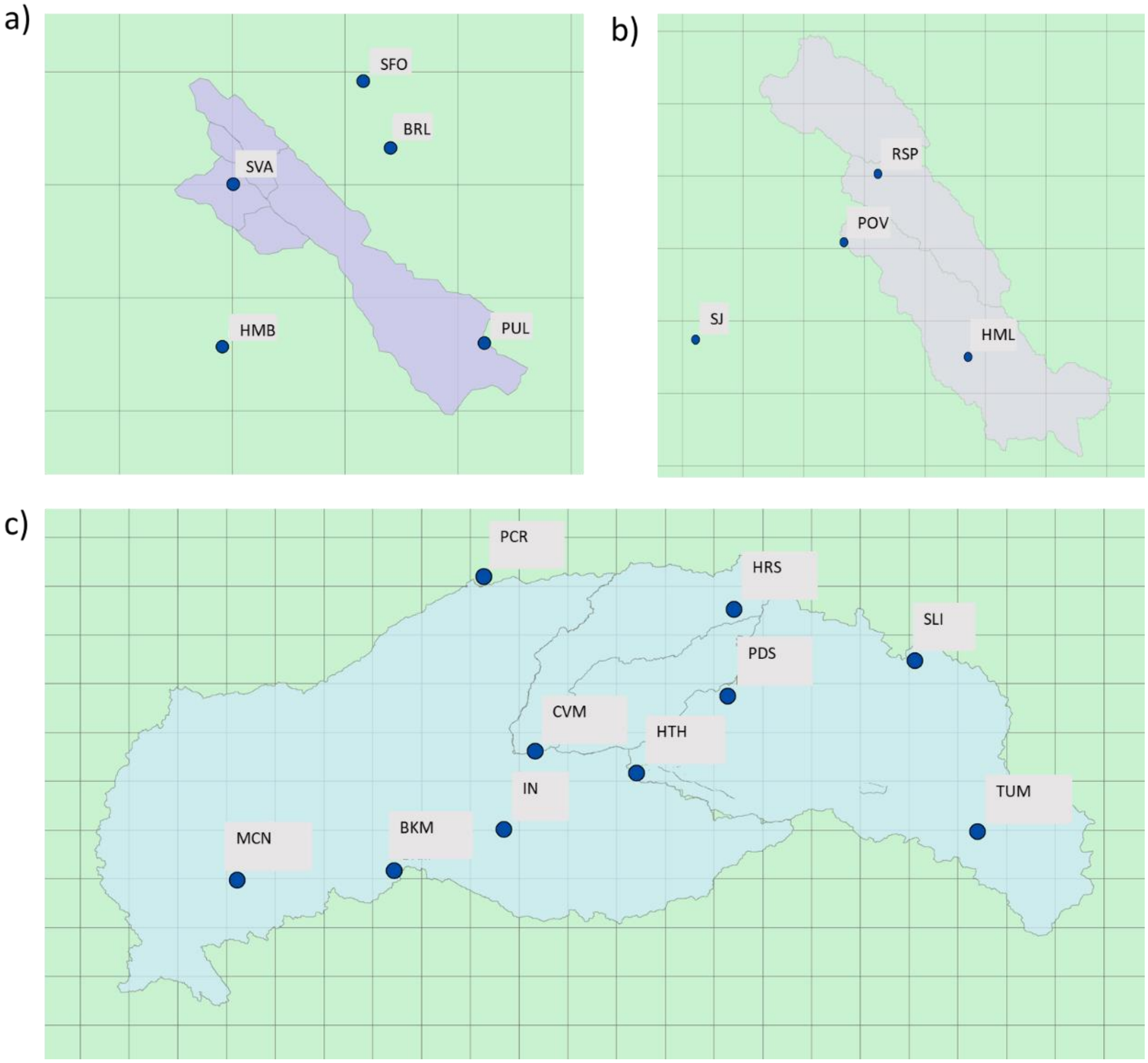

Figure 16. CONUS data grid cells (at 6.25 km² spatial resolution) and the temperature gage stations in the SFPUC RWS: a) Peninsula region, b) East Bay region, and c) Upcountry region

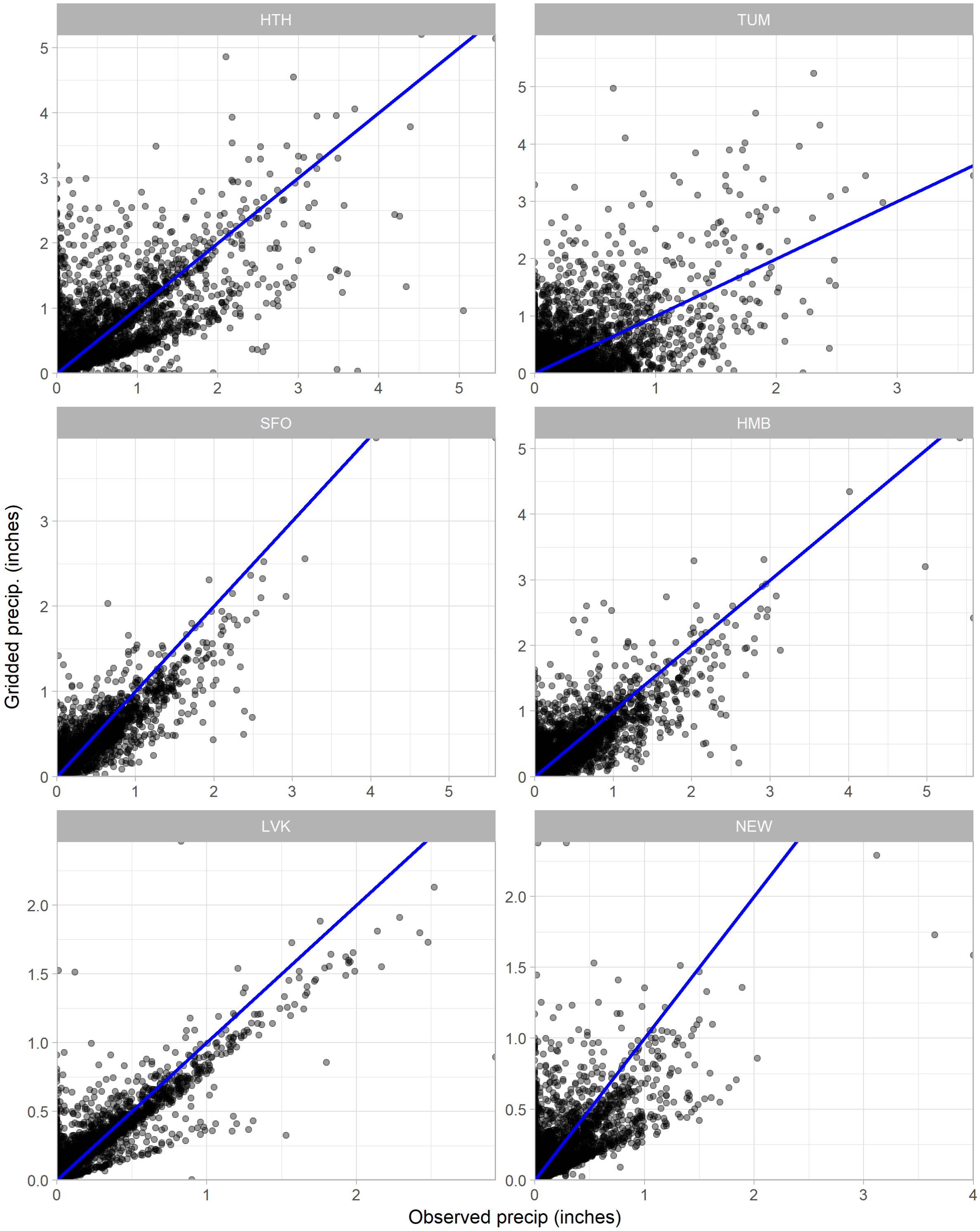

Figure 17. Comparison of daily precipitation from observed (gage) data and CONUS dataset over the 1956-2011 analysis period. Results are shown for the Hetch Hetchy (HTH), Tuolumne (TUM), San Francisco Airport (SFO), Half Moon Bay (HMB), Livermore (LVK), and Newark (NEW) stations respectively.

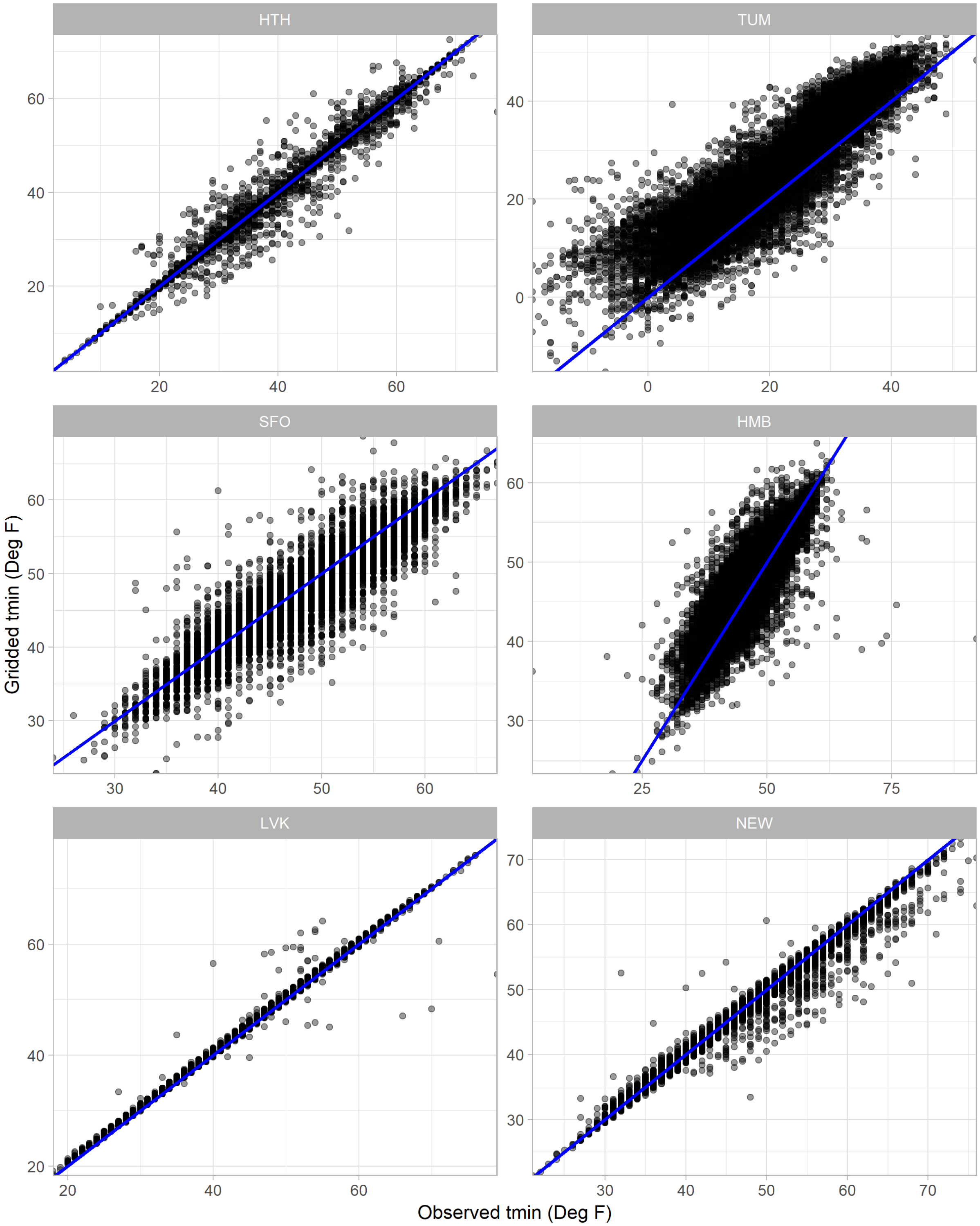

Figure 18. Comparison of daily minimum temperatures from observed (gage) data and CONUS dataset over the 1956-2011 analysis period. Results are shown for the Hetch Hetchy (HTH), Tuolumne (TUM), San Francisco Airport (SFO), Half Moon Bay (HMB), Livermore (LVK), and Newark (NEW) stations respectively.

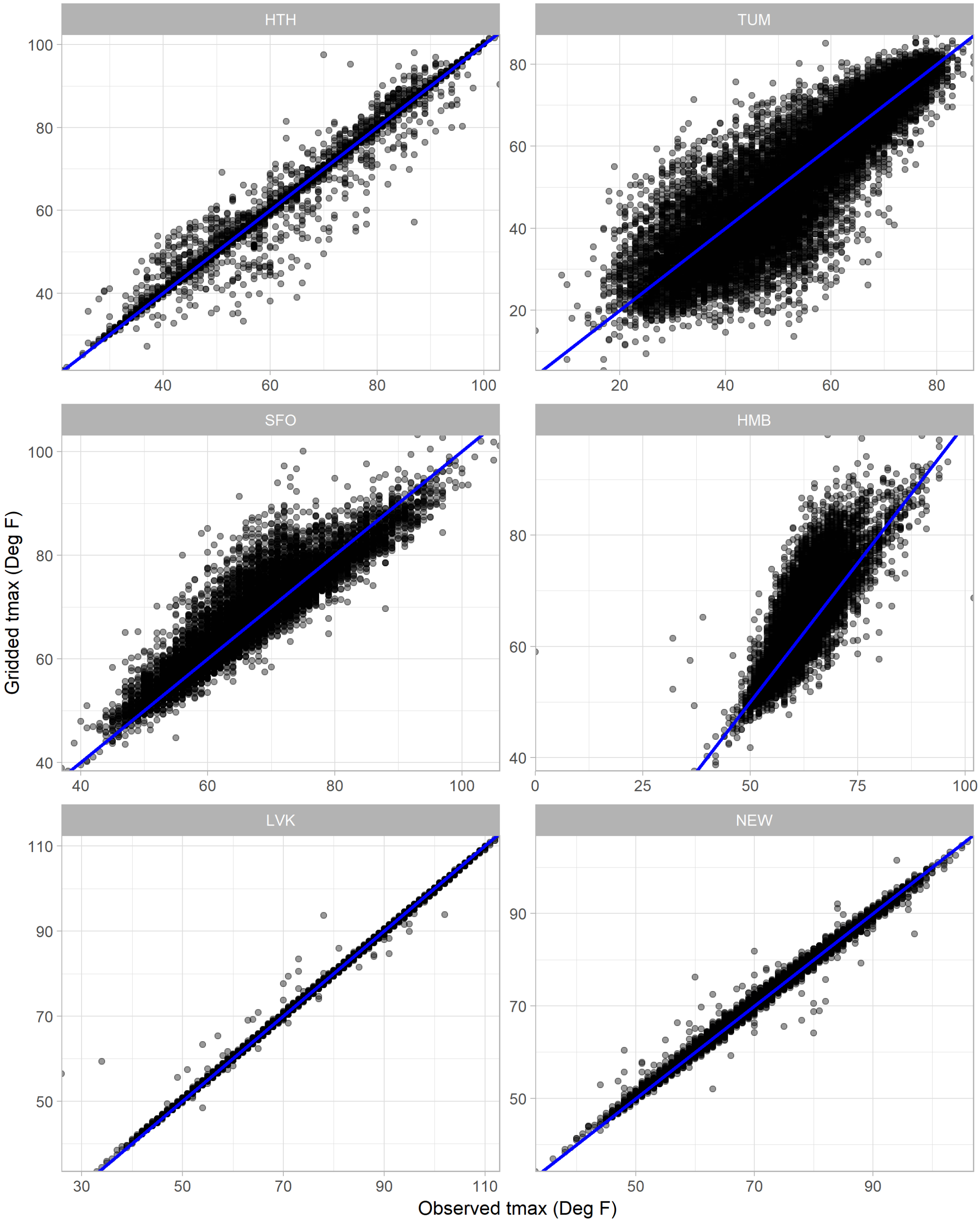

Figure 19. Comparison of daily maximum temperatures from observed (gage) data and CONUS dataset over the 1956-2011 analysis period. Results are shown for the Hetch Hetchy (HTH), Tuolumne (TUM), San Francisco Airport (SFO), Half Moon Bay (HMB), Livermore (LVK), and Newark (NEW) stations respectively.

Overall, the gridded precipitation is found to be not suitable for conditioning the weather generator. Instead, the thirteen precipitation gages that have the longest records and are representative of precipitation across the three regions are used as inputs (**Table 4**).

Combined with the CONUS daily gridded temperature dataset, the stochastic weather generator is conditioned on the fifty-five-year historical period from 1956 to 2011.

Table 4. The final precipitation dataset used in the weather generator

Station	**Short name**	**Region**	**Period of record (full range)**	**Period of record (used)**
Upper Crystal Springs	UCS	Peninsula	1908 – 2017	1956 - 2011
Lower Crystal Springs	LCS	Peninsula	1915 - 2017	1956 - 2011
San Andreas	SA	Peninsula	1908 - 2017	1956 - 2011
Pilarcitos	PLD	Peninsula	1909 - 2017	1956 - 2011
Sunol	SUNO	East Bay	1907 - 2017	1956 - 2011
Calaveras	CAL	East Bay	1915 - 2017	1956 - 2011
Mt. Hamilton	HML	East Bay	1948 - 2017	1956 - 2011
Hetch Hetchy	SFO	Upcountry	1930 - 2017	1956 - 2011
Early Intake	IN	Upcountry	1930 - 2017	1956 - 2011
Moccasin	MCN	Upcountry	1930 - 2017	1956 - 2011
Cherry Valley	CVM	Upcountry	1952 - 2018	1956 - 2011
Yosemite	YOS	Upcountry	1956 - 2017	1956 - 2011
Sonora	SON	Upcountry	1956 - 2017	1956 - 2011

3.2. Principal Component Analysis on Annual Precipitation

In order to generate new realizations of the historical climate, the first step is to obtain a representative time-series annual precipitation over the study region, i.e., SFPUC RWS. Typically, a representative time-series is provided by area-averaging the precipitation data at different gage locations across the study area. However, spatial-averaging may not be appropriate in cases where the precipitation shows high spatial variability, as for the case of the SFPUC system (Figure 6 and Appendix I). In such cases, a principal component analysis (PCA) can be applied to preserve the variability between the stations that would be lost if they were simply averaged together.

In simple terms, PCA is a dimension-reduction method that can be used to transform a large number of (possibly) correlated variables into a (smaller) number of variables called principal components. PCA finds a new set of dimensions such that all the dimensions are orthogonal (and hence linearly independent) and ranked according to the variance of data among them. The first principal component accounts for as much of the variability in the data as possible, and each succeeding component accounts for as much of the remaining variability as possible. Application of PCA includes a number of sequential steps including calculation of the covariance matrix of the data points, the eigen vectors, and corresponding eigen values, and sorting the eigen vectors according to their eigen values in the decreasing order.

For this study, we apply PCA on the historical annual precipitation series (1956-2011 period) from the thirteen gage stations to identify one or few principal components that can adequately explain the variance within the full set of data. The results of the PCA including the percentage of variance explained by each principal component as well as the loading factors for all precipitation gage stations for all components is shown in Table 5. The first principal component explains about 88% of the total variance, whereas the first two components together account for the 94% of the total variance in the historical annual precipitation record.

Table 5. Summary of results from the PCA on annual precipitation data across the thirteen gage stations. The top row shows the percentage of variance explained by each principal component. The remaining rows show the computed gage station loadings for each component.

Stations	**PC1**	**PC2**	**PC3**	**PC4**	**PC5**	**PC6**	**PC7**	**PC8**	**PC9**	**PC10**	**PC11**	**PC12**	**PC13**
	(88%)	*(4.9%)*	*(1.3%)*	*(1.2%)*	*(0.9%)*	*(0.6%)*	*(0.5%)*	*(0.4%)*	*(0.2%)*	*(0.2%)*	*(0.1%)*	*(0.1%)*	*(0.1%)*
Calaveras	0.18	-0.13	0.05	-0.18	0.06	-0.31	0.10	0.08	-0.56	0.24	-0.21	-0.14	-0.61
Cherry	0.44	0.34	-0.35	0.32	0.02	-0.20	0.36	-0.39	-0.03	0.16	-0.23	0.20	0.17
Hamilton	0.19	-0.05	0.58	0.57	-0.38	-0.34	-0.13	0.11	0.02	-0.01	0.07	-0.03	0.03
HetchHetchy	0.33	0.21	-0.18	0.06	0.34	-0.25	-0.29	0.24	0.18	-0.58	-0.12	-0.30	-0.12
Intake	0.30	0.14	-0.05	0.06	0.33	0.05	-0.21	0.20	-0.10	0.25	0.68	0.38	-0.10
LowCS	0.21	-0.35	-0.05	-0.32	0.02	-0.37	-0.38	-0.18	0.46	0.42	-0.11	-0.01	0.11
Moccasin	0.25	0.05	0.30	0.18	0.38	0.55	-0.11	0.09	0.00	0.36	-0.35	-0.29	0.12
Pilarcitos	0.31	-0.52	-0.44	0.22	-0.34	0.33	-0.28	-0.01	-0.26	-0.14	0.01	-0.03	0.03
SanAndreas	0.27	-0.33	0.05	0.00	0.05	0.10	0.60	-0.06	0.36	-0.05	0.37	-0.36	-0.20
Sonora	0.29	0.13	0.39	-0.34	-0.07	0.19	-0.19	-0.64	-0.16	-0.31	0.12	0.05	-0.06
Sunol	0.17	-0.16	0.10	-0.27	0.13	-0.23	0.18	0.19	-0.41	-0.07	0.12	-0.17	0.71
UppCS	0.21	-0.30	0.22	-0.12	0.12	0.09	0.22	0.26	0.14	-0.26	-0.34	0.67	-0.04
Yosemite	0.33	0.42	-0.04	-0.39	-0.57	0.17	0.05	0.41	0.13	0.12	-0.03	-0.07	-0.01

PCA results are further investigated by a biplot (Figure 20). The x and y-axes of the biplot show the first pair of principal components (i.e., PC1 and PC2) and to what extent they can explain the variance in annual precipitation data from each of the thirteen gage stations. PC1 explains most of the variance in precipitation gages, except for the Hamilton station, which is more strongly associated with PC2. Most stations within the Peninsula and East Bay regions show a similar response profile (indicated by the direction of the vectors in Figure 20), whereas the stations in the Upcountry region are found to be different than the stations in the former two regions.

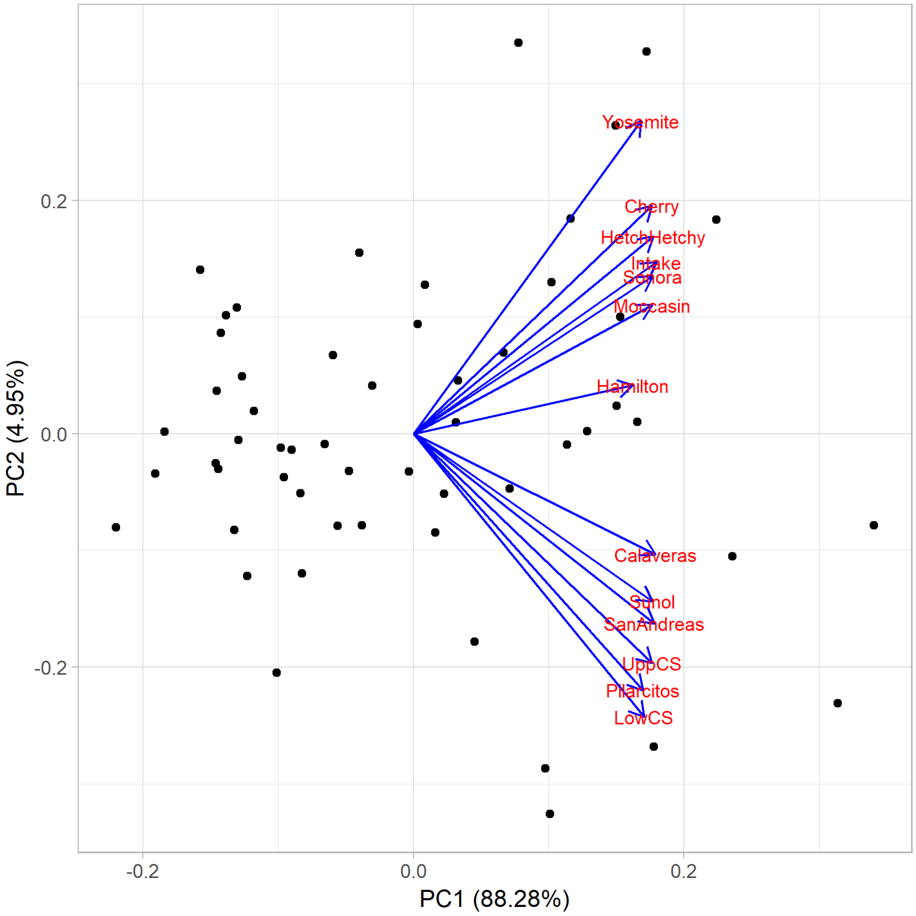

Figure 20. PCA biplot for historical annual precipitation from thirteen gage stations. The x and y-axes show the first and the second principal components of the PCA. The values in the parentheses show the total variance explained. The points represent the scores of the observations on the principal components. The cosine of the angle between a vector and an axis indicates the importance of the contribution of the corresponding variable to the axis dimension.

Wavelet analyses are also performed on the first two principal components to evaluate the spectral signature of each component. PC1 has a significant low-frequency variability signal at about 15 years, similar to the previously detected low-frequency signal of 12-15 years in the historical precipitation data (Figure 21).

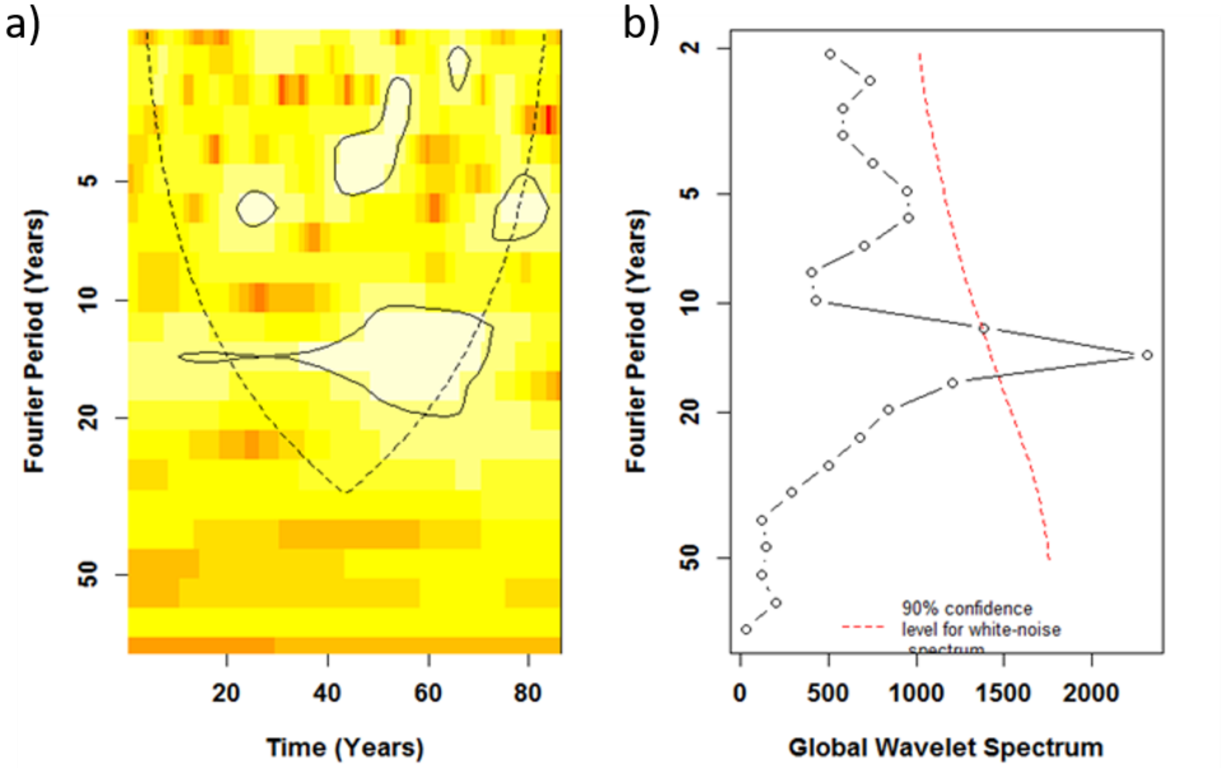

Figure 21. Wavelet analysis on the PC1 of historical annual precipitation: a) the local wavelet spectrum displaying the strength of each signal locally around the given time (shown in x-axis), b) the global wavelet plot, which is obtained by integrating the local wavelet spectrum over time. In a, the black contours show the scales at which power spectra appear greater than 95% confidence for a red-noise process. The cross-hatched regions on either end indicate the "cone of influence," where edge effects become important. In b, the dashed red line shows the significance, assuming the same significance level and background spectrum as in the local wavelet power spectra.

In contrast to the PC1, the second principal component does not show any statistically significant low-frequency signal (Figure 22).

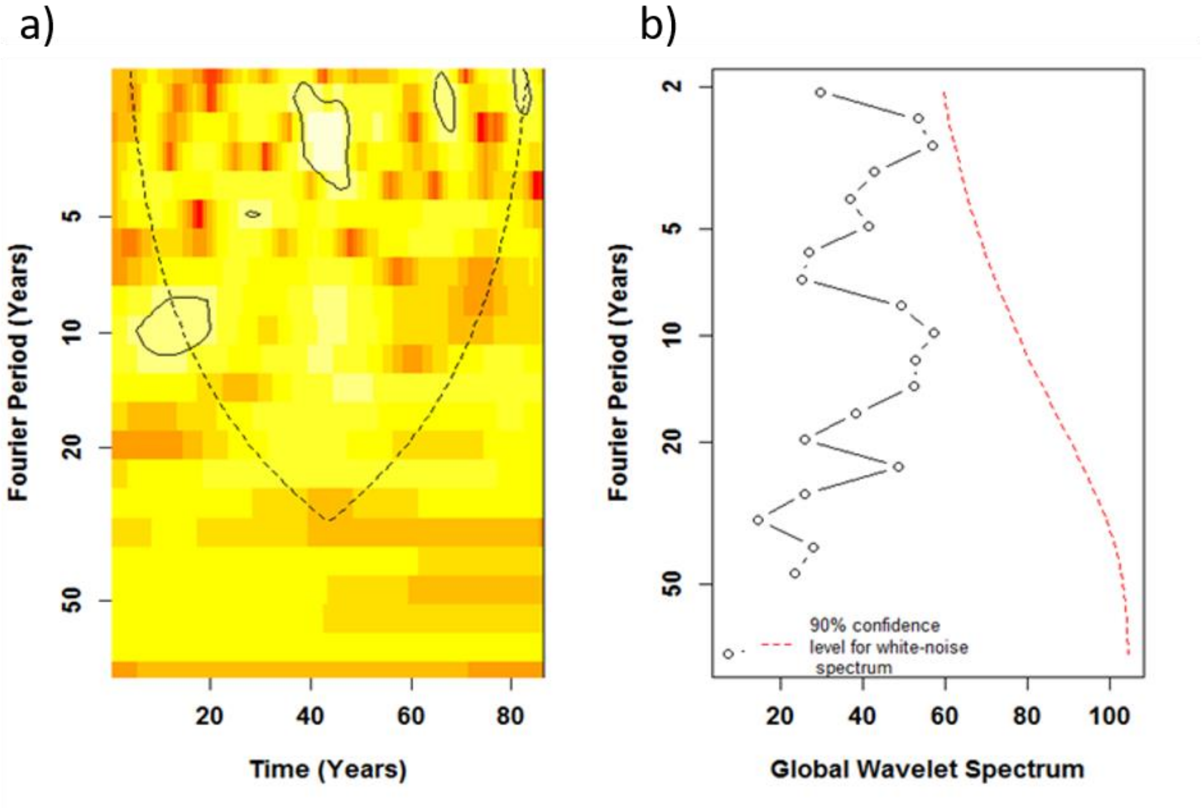

Figure 22. Wavelet analysis on the PC2 of historical annual precipitation: a) the local wavelet spectrum displaying the strength of each signal locally around the given time (shown in x-axis), b) the global wavelet plot, which is obtained by integrating the local wavelet spectrum over time. In a, the black contours show the scales at which power spectra appear greater than 95% confidence for a red-noise process. The cross-hatched regions on either end indicate the "cone of influence," where edge effects become important. In b, the dashed red line shows the significance, assuming the same significance level and background spectrum as in the local wavelet power spectra.

Finally, we evaluated the correlations between the first two principal components and the observed average sea level pressures (SLP) and sea surface temperatures (SST) to have a better understanding of the underlying climate drivers. Figure 23 shows that PC1 is correlated with both SLP and SST in areas typically associated with El Niño–Southern Oscillation (ENSO) and Pacific Decadal Oscillation (PDO). However, PC2 is not seen to be associated with any climate patterns (Figure 24).

Based on the results presented in this section, we only apply the WARM to the first principal component of annual precipitation.

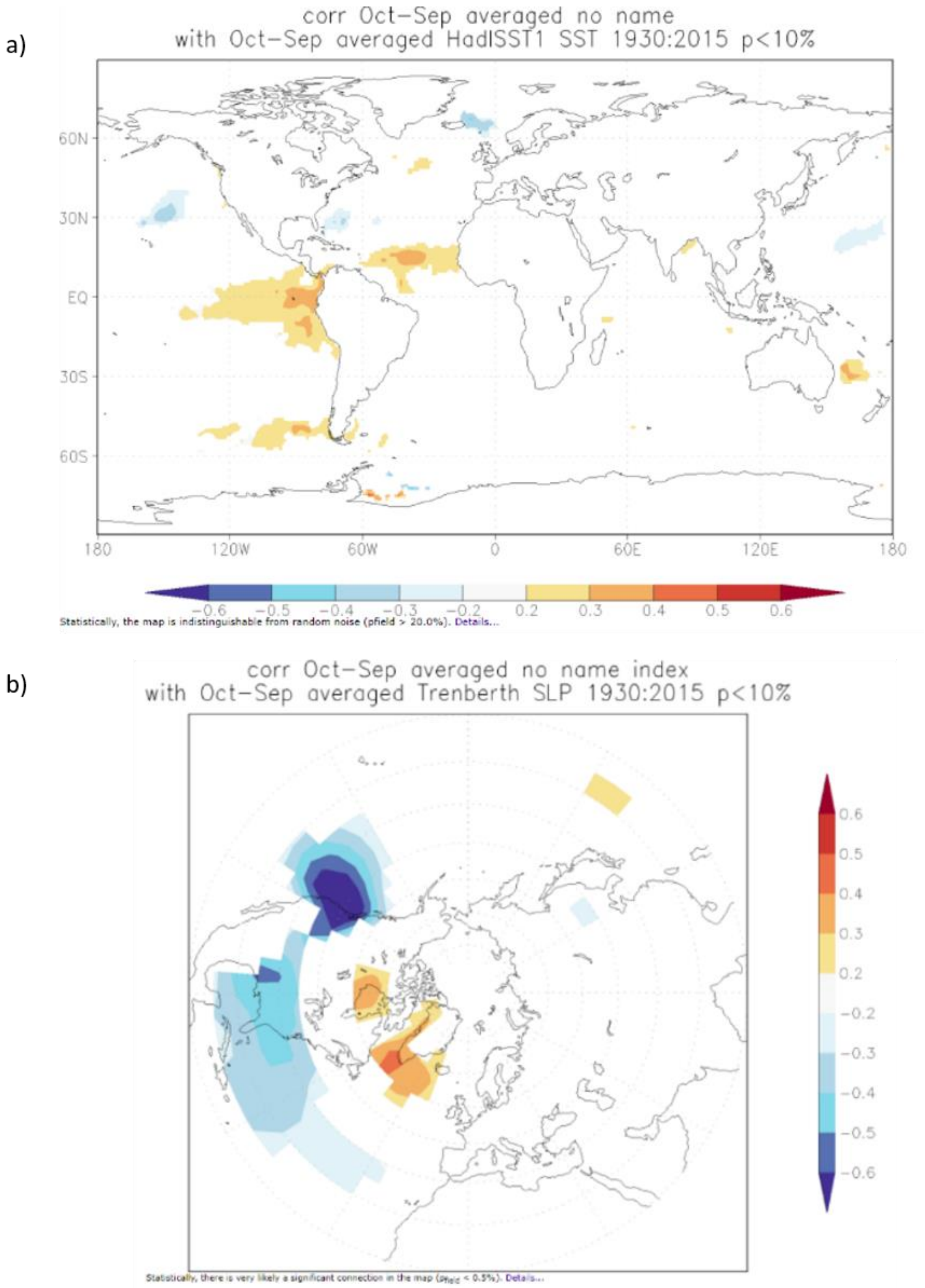

Figure 23. Correlation plots: a) PC1 vs. averaged annual sea surface temperature (SST) (b) PC1 vs. averaged annual sea level pressure (SLP)

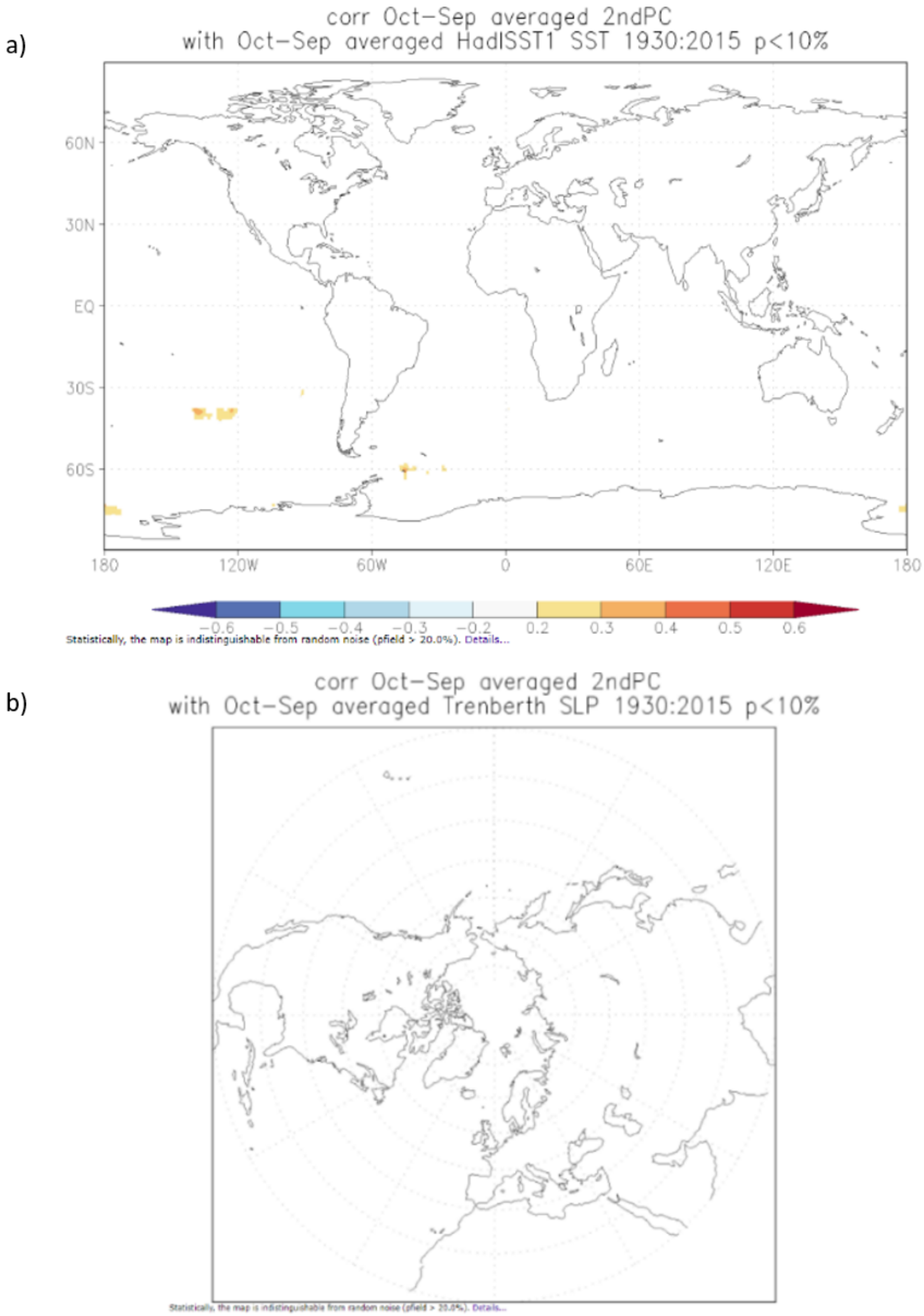

a) corr Oct−Sep averaged 2ndPC with Oct−Sep averaged HadISST1 SST 1930:2015 p<10%

Statistically, the map is indistinguishable from random noise (pfield > 20.0%). Details...

b) corr Oct−Sep averaged 2ndPC with Oct−Sep averaged Trenberth SLP 1930:2015 p<10%

Statistically, the map is indistinguishable from random noise (pfield > 20.0%). Details...

Figure 24. Correlation plots: a) PC2 vs. averaged annual sea surface temperature (SST) (b) PC2 vs. averaged annual sea level pressure (SLP)

3.3. Stochastic Simulations of the PC1 of Annual Precipitation

After choosing the PC1 as a representative series of annual precipitation, the next task is to generate new stochastic realizations of this series. For this purpose, we use a wavelet autoregressive model (WARM), a time-series simulation approach that combines simple autoregressive models with wavelet decomposition (Kwon et al. 2007; Steinschneider and Brown 2013). Briefly, WARM decomposes a univariate time series into several statistically significant components using a continuous wavelet transform function. After the significant low-frequency components of the time-series is identified, an autoregressive (AR) model is then employed to each of these components for stochastic simulation. Finally, the simulated time-series is obtained from the summation of each simulated component.

The WARM application for the SFPUC study begins with decomposing the PC1 of annual precipitation into its low-frequency components. The wavelet decomposition process considers a series of orthogonal or independent series that carry low-frequency information within the data (i.e., persistence at inter-annual and multi-decadal time scales). Figure 25 displays the PC1 series of annual precipitation (at the top) and the identified low-frequency component at about 12-15 years (in the middle) along with the residual term (at the bottom). Next, the low-frequency component and residual term are simulated using a series of linear AR models. The model order (p) and coefficients are determined using the "auto.arima (…)" function in the forecast package in R language (Hyndman and Khandakar 2008). After the AR models are defined, the time-series components are simulated using the "arima.sim (…)" function from the same R package. Note that the time-series models employed here (linear AR models) are additive in nature with no interactions across the noise or the signals. Based on this feature, we aggregate the simulated low-frequency component and the residual noise term to obtain a single simulated series of PC1.

The warm process, i.e., the wavelet decomposition of PC1 of annual precip, the stochastic simulation of decomposed components, and finally aggregation of the simulated components, is repeated to obtain a set of (n = 1,000) stochastic realizations, each having 50-years of length.

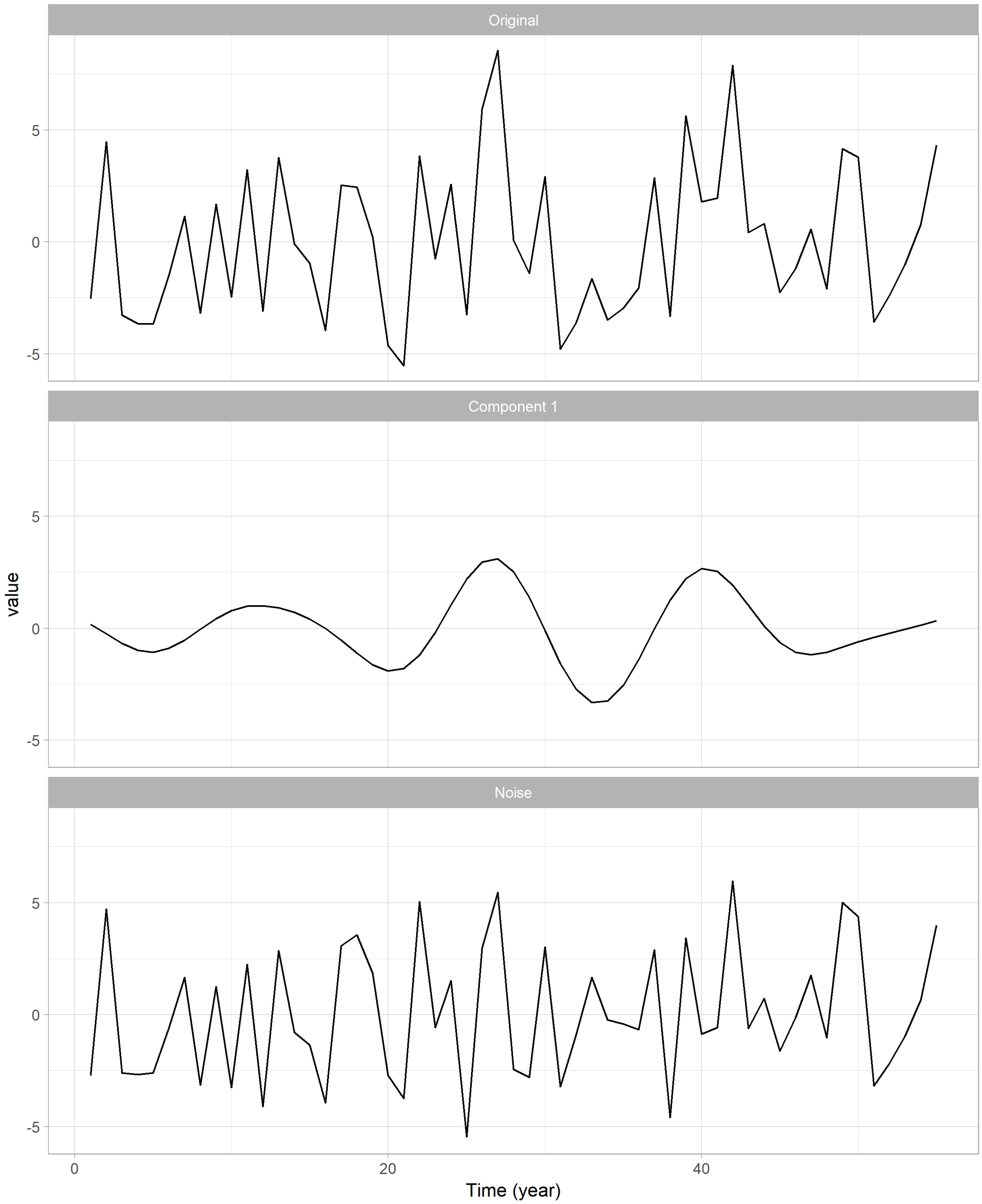

Figure 25. Wavelet decomposition of the PC1 of annual precipitation (Original = PC1 of annual precipitation, Component 1 = detected low-frequency signal at about 12-15 years, Noise = the residual series from the PC1)

3.4. Disaggregation of Simulated PC1 Series in Time and Space

The stochastic climate data generated in Section 3.2 provides new realizations of the PC1 of annual precipitation. However, for stress testing the water resources system, this data needs to be disaggregated into daily values of climate variables (i.e., precipitation, and minimum and maximum temperature) at different locations.

The disaggregation of simulated PC1 of annual precipitation begins with inverting the vector of 50-year simulated series to a matrix of multi-site data consisting of 50 years of annual precipitation values for each of the thirteen precipitation gage stations. This is done by multiplying the simulated PC1 series by the station loading factors obtained from the PCA (Table 5), and then rescaling the station-specific precipitation values based on the computed mean and standard deviations from each gage.

Next, we disaggregate the multi-site annual precipitation data into monthly values using the "method of fragments" (Srikanthan and McMahon 2001; Silva and Portela 2012). The method of fragments is applied by obtaining the monthly precipitation ratios from the historical record and then standardizing the observed monthly rainfall time-series so that the sum of the monthly rainfalls in any given year equals unity. This results in 55 sets of fragments of monthly rainfalls from a record of 55-year data. For each year in the simulated multi-site annual precipitation data, we then identify the most similar year regarding mean annual precipitation and distribute the simulated annual precipitation value to monthly values using the twelve-monthly fragments from this most similar year. This procedure is repeated for all years of the simulated annual precipitation realizations.

In the third and the final step, we further disaggregate the simulated monthly precipitation to daily values for all weather variables, i.e., precipitation and minimum, average and maximum temperature. This procedure is done using a non-parametric k-nearest neighbors (knn) resampling algorithm (Lall and Sharma, 1996). Knn is applied by finding k number of historical nearest neighbors from the historical monthly precipitation record, and then resampling among those k neighbors. In this process, a discrete resampling kernel is introduced to place higher weights to the neighbors that are more similar to the simulated value (shown below). Once a historical month is sampled among the k neighbors, all daily values of climate variables (precipitation and minimum, average, and maximum temperatures) are taken from that sampled month. The knn resampling process preserves the covariance structure between the weather variables and across space since the values are directly sampled from the historical record.

Below are the algorithms used for the method of fragments and knn resampling:

Method of fragments approach (adapted from Silva & Portela, 2012)

1. Begin with an inverted series of each annual precipitation realization $n \in N$
2. For each gage $i \in I$, determine which year k in the observed record had the most similar annual precipitation to the simulated annual precipitation $P_{i,k}^{n}$
3. Calculate the proportion of annual precipitation in each month for year k to obtain twelve monthly factors $f(m)_{i,k}^{n}$, where m is the calendar month from 1 to 12
4. Use $f(m)_{i,k}^{n}$values from step 2 to distribute the simulated annual precipitation $P_{i,k}^{n}$ into monthly values $f(m)_{i,k}^{n} * P_{i,k}^{n}$
5. Repeat steps 1 to 4 for each year $k \in K$ and gage $i \in I$
6. Repeat step 5 for each all annual precipitation realizations $n \in N$

KNN resampling algorithm (adapted from Lall and Sharma, 1996)

1. Begin with a simulated monthly precipitation series obtained from the method of fragments. For each month m, a vector of simulated precipitation values P_s of length thirteen (the number of gage stations) is available.
2. Calculate the Euclidean distances d, between P_s and each of the Q vectors of observed monthly precipitation for the same calendar month.
3. Order the computed Euclidean distances d from the smallest to the largest and select k smallest distances, d_j where j is the index of the ordered distances $\{1,2,..k\}$. The value of k is set based on the square root of the sample size (in this case set as 7)
4. Assign weights to each d_j using the discrete kernel function:

   $$w_j = \frac{\frac{1}{j}}{\sum_{j=1}^{k} \frac{1}{j}}$$

   where the weights assigned to k nearest neighbors w_j sum to 1.
5. Sample one value from the k-nearest neighbors, using the weights w_j as the vector probabilities assigned to each nearest neighbor, and record the historical month associated with that value.
6. Obtain the daily values of all climate variables, i.e., precipitation and minimum, average, and maximum temperature from the sampled historical month.
7. Repeat steps from 1 to 6 for all months
8. Repeat step 7 for each annual precipitation realizations

3.5. Weather generator performance

In this section, we evaluate the performance of the weather generator based on its skill in replicating the statistics of the historical climate period (1956-2011).

Figure 26 presents the power spectra from 1,000 stochastic annual precipitation realizations. The mean power signal from the stochastic series (black line) matches well to the power spectra of the historical annual precipitation (blue line) with a bump at the period length of 11-14 years. Results also show that the observed spectra are within the range of the simulated spectra (marked by the gray band) for the period lengths of up to 30 years.

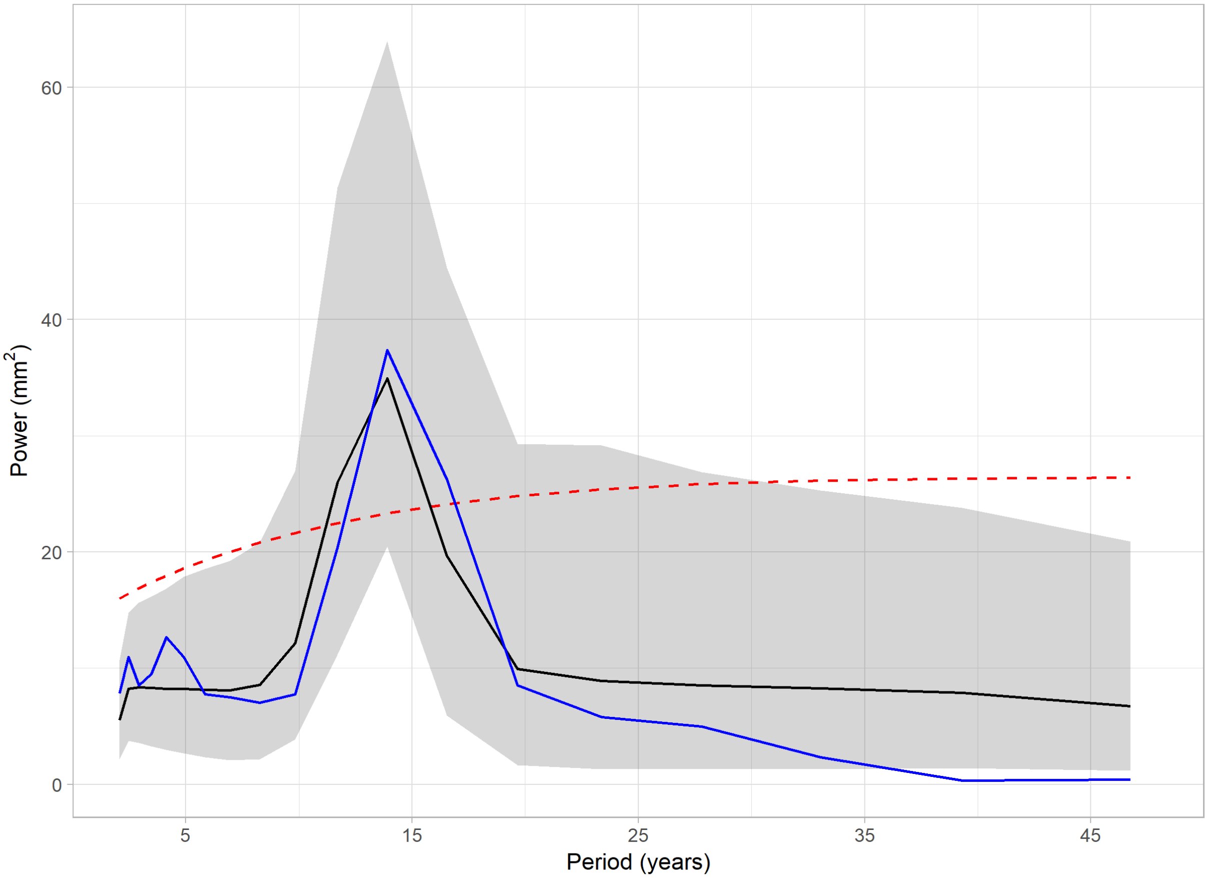

Figure 26. Global power spectra for annual precipitation. The observed spectra (blue) are compared against the mean power spectra (black) of the 1,000 simulations, along with range bounded by the 2.5th and 97.5th percentiles of the power spectra for the ensemble (gray). Also shown is the 95% significance level (red dotted). The power spectra of the observations and simulations become statistically significant if they rise above the red dotted line.

Figure 27 compares annual mean precipitation from 1,000 stochastic realizations to the observed values (1956-2011 period) for each gage station across the Upcountry, Peninsula, and East Bay regions. Overall, there is good agreement between the simulated and observed annual precipitation, and the historical means are within the simulated range, except for the SUNO station in East Bay.

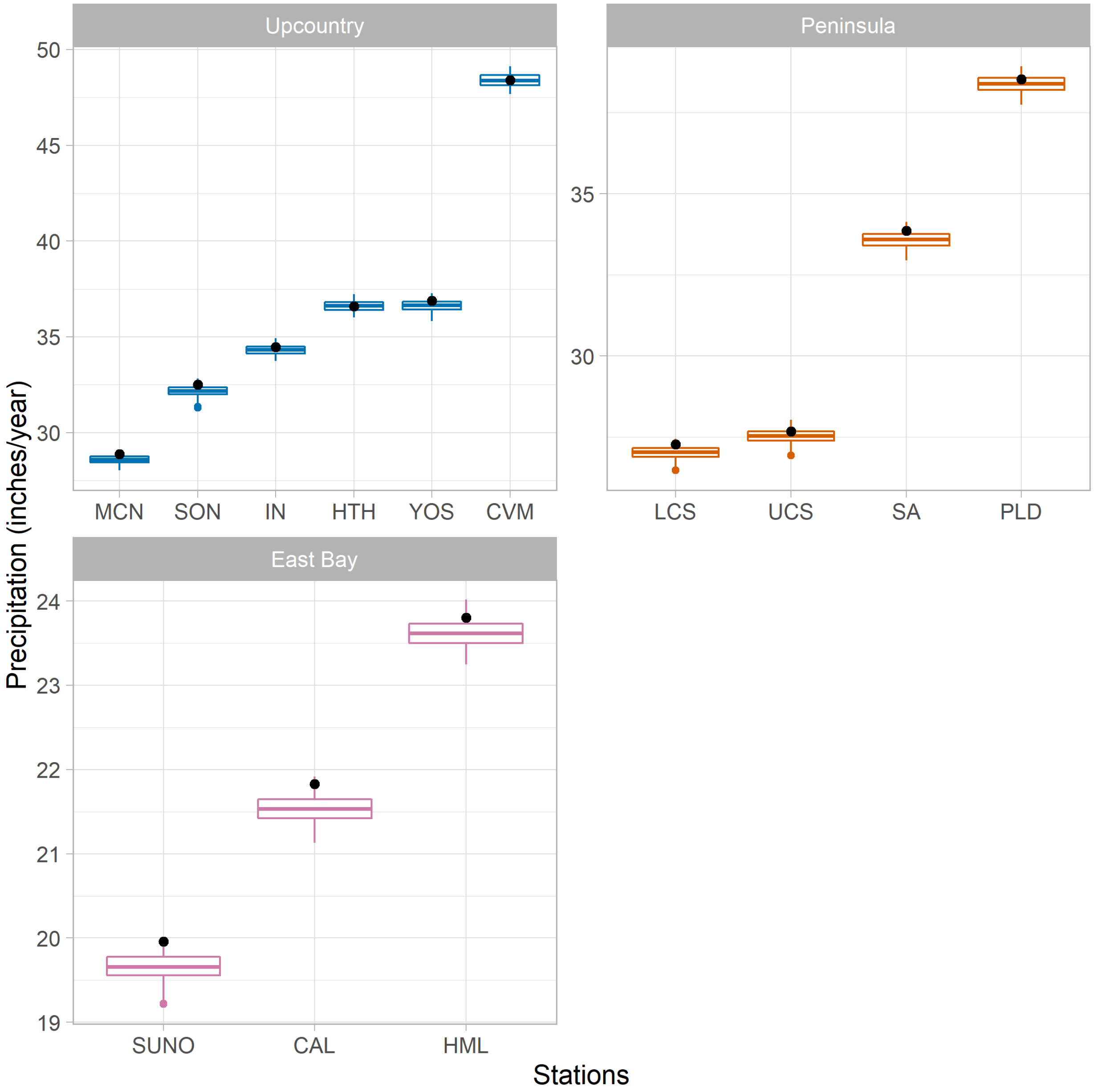

Figure 27. Boxplots of simulated annual average precipitation across the gage stations in the three regions (Upcountry = blue, Peninsula = orange, East Bay = pink). The black dots represent the observed annual precipitation for each gage station.

Figure 28 compares average daily precipitation from the stochastic realizations to the average daily historical values for each calendar month. Results from the stochastic realizations vary over the wet season. Historical daily precipitation is well represented from January to March, underestimated in November, and overestimated in December.

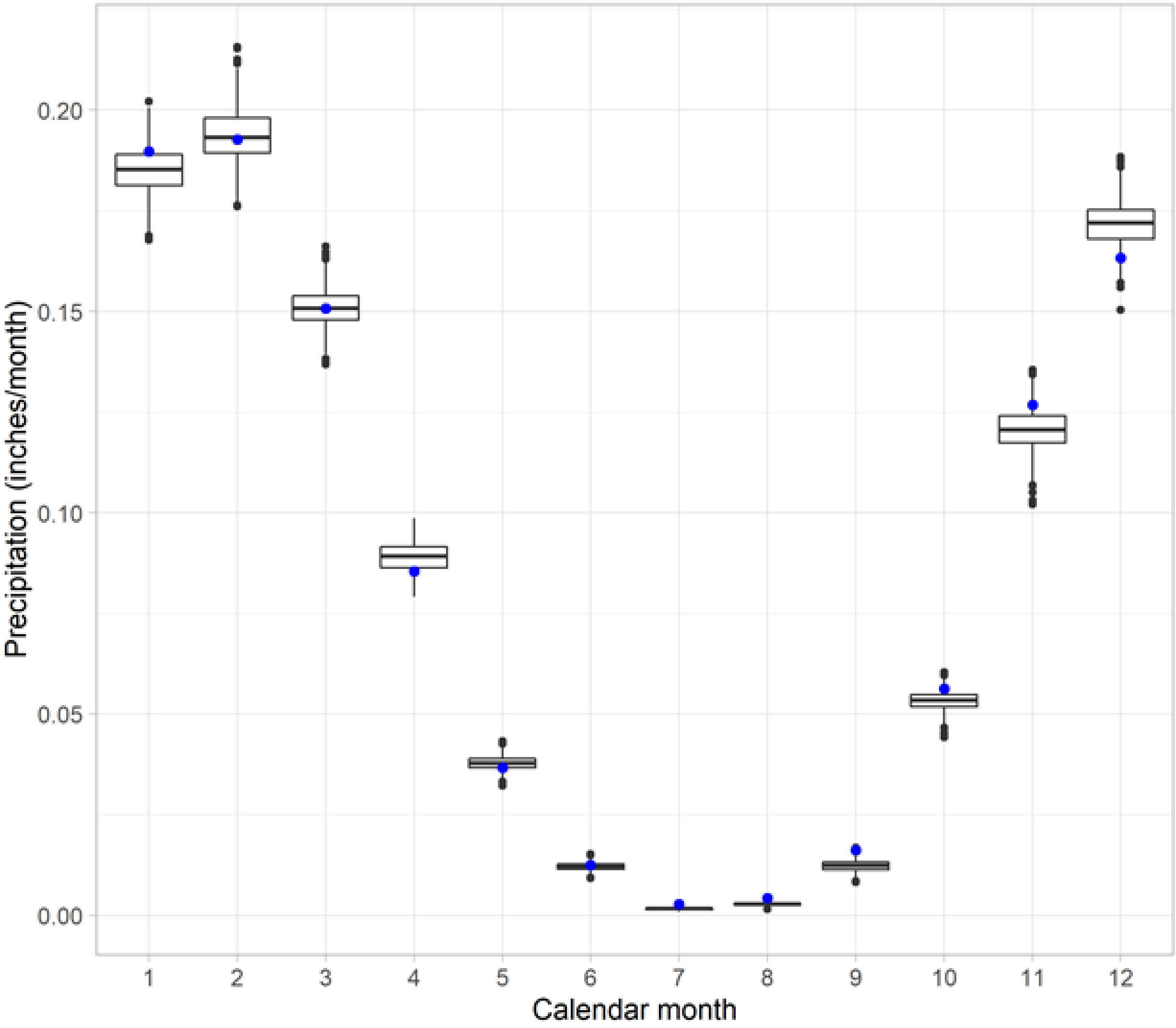
Precipitation (inches/month)
0.20
0.15
0.10
0.05
0.00
1
2
3
4
5
6
7
8
9
10
11
12
Calendar month

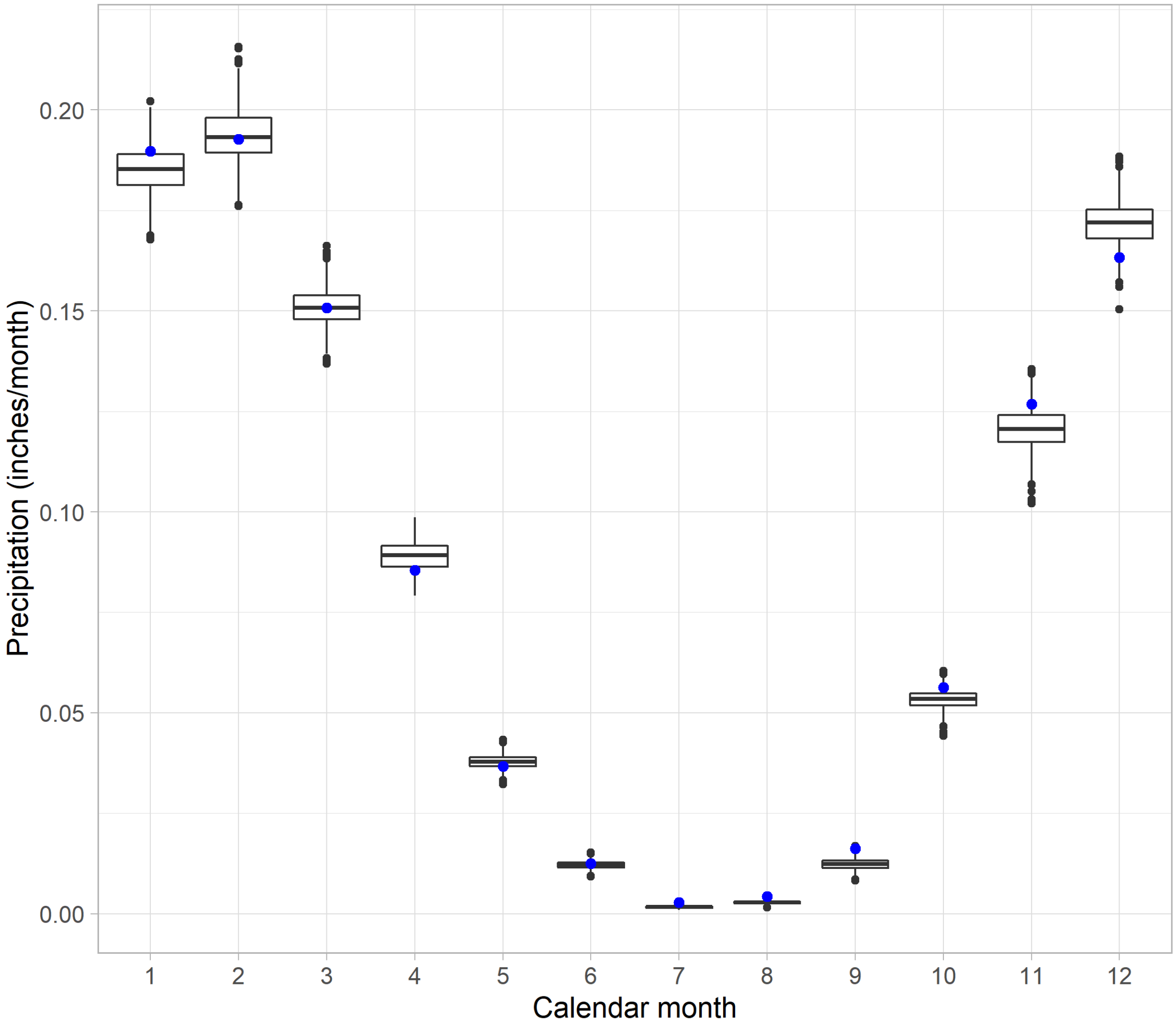

Figure 28. Box-plots of mean monthly precipitation from the stochastic realizations. Historical monthly mean precipitation is shown by the blue dot. Results show spatially-averaged values across the thirteen gage stations.

Figure 29 compares average daily T_{min} values from the stochastic realizations to the observed T_{min} for each calendar month. Results show that the observed values are within the range of the simulated T_{min} values, however, the match between the two dataset varies based on the month. A similar comparison is also shown for the daily T_{max} values with comparable results (Figure 30).

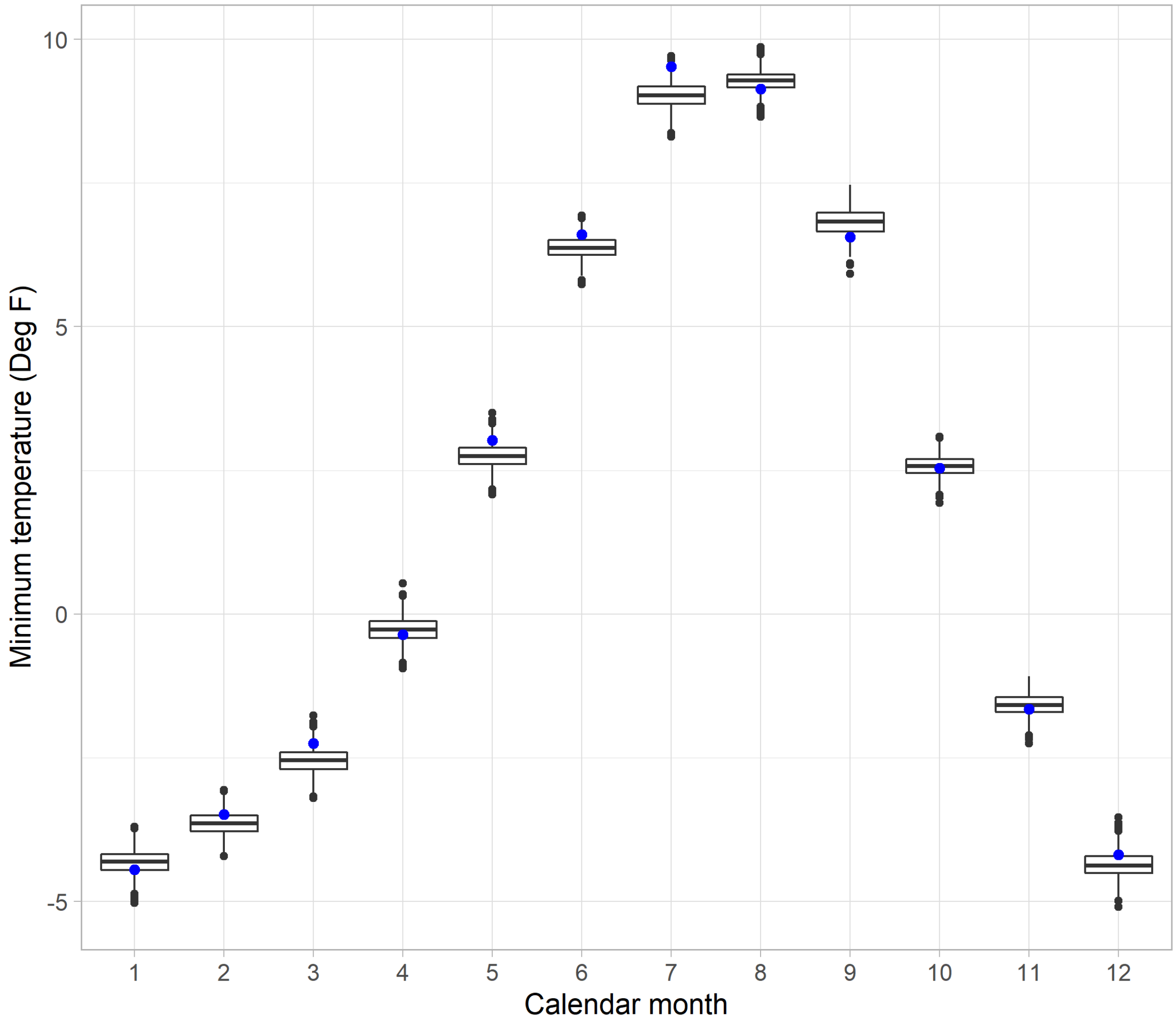

Figure 29. Box-plots of mean monthly precipitation from the stochastic realizations. Historical monthly mean precipitation is shown by the blue dot. Results show spatially-averaged values across the thirteen gage stations.

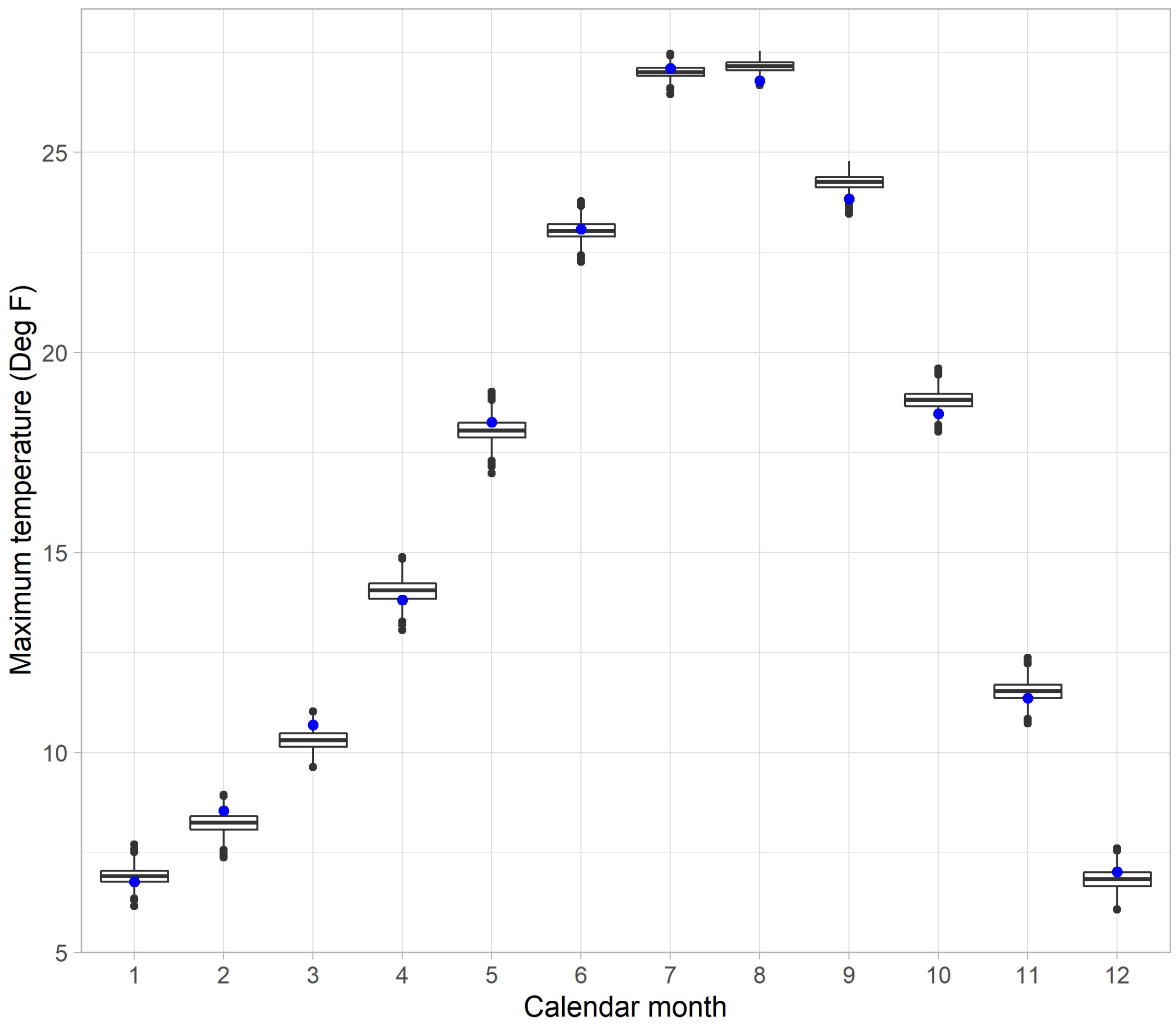

Figure 30. Box-plots of mean monthly precipitation from the stochastic realizations. Historical monthly mean precipitation is shown by the blue dot. Results show spatially-averaged values across the thirteen gage stations.

Next, we examine the first and higher-order statistics for all simulated daily weather variables across all stations (i.e., precipitation, minimum temperature, and maximum temperature) from the same 1,000 stochastic realizations.

Figure 31 depicts the mean, standard deviation, skew, and kurtosis of nonzero daily precipitation amounts. For this evaluation, we find the median values over the 1,000 stochastic realizations and compared them to the statistics of the underlying historical analysis period. The results suggest very good performance regarding the mean of precipitation. The standard deviation of precipitation is slightly underestimated. The skewness and kurtosis of simulated precipitation matches well with the historical values, except for a few outlier values.

Figure 32 shows the mean, standard deviation, skew, and kurtosis of daily minimum temperatures computed from the median results of 1000 stochastic realizations. Daily means and standard deviations show good performance with no noticeable bias. For both skew and kurtosis parameters, performance varies across different grid cells and months. However, we did not identify any systematic bias (i.e., under or overestimation).

Figure 33 displays the mean, standard deviation, skew, and kurtosis of daily maximum temperatures computed from the median results of 1000 stochastic realizations. Daily means of maximum temperature matches very well with the historical values. However, the match between the historical and simulated standard deviation varies across different grid cells and months and overall shows a slight negative bias. The match between the simulated and observed maximum temperature is acceptable for the skewness, and poor for the kurtosis.

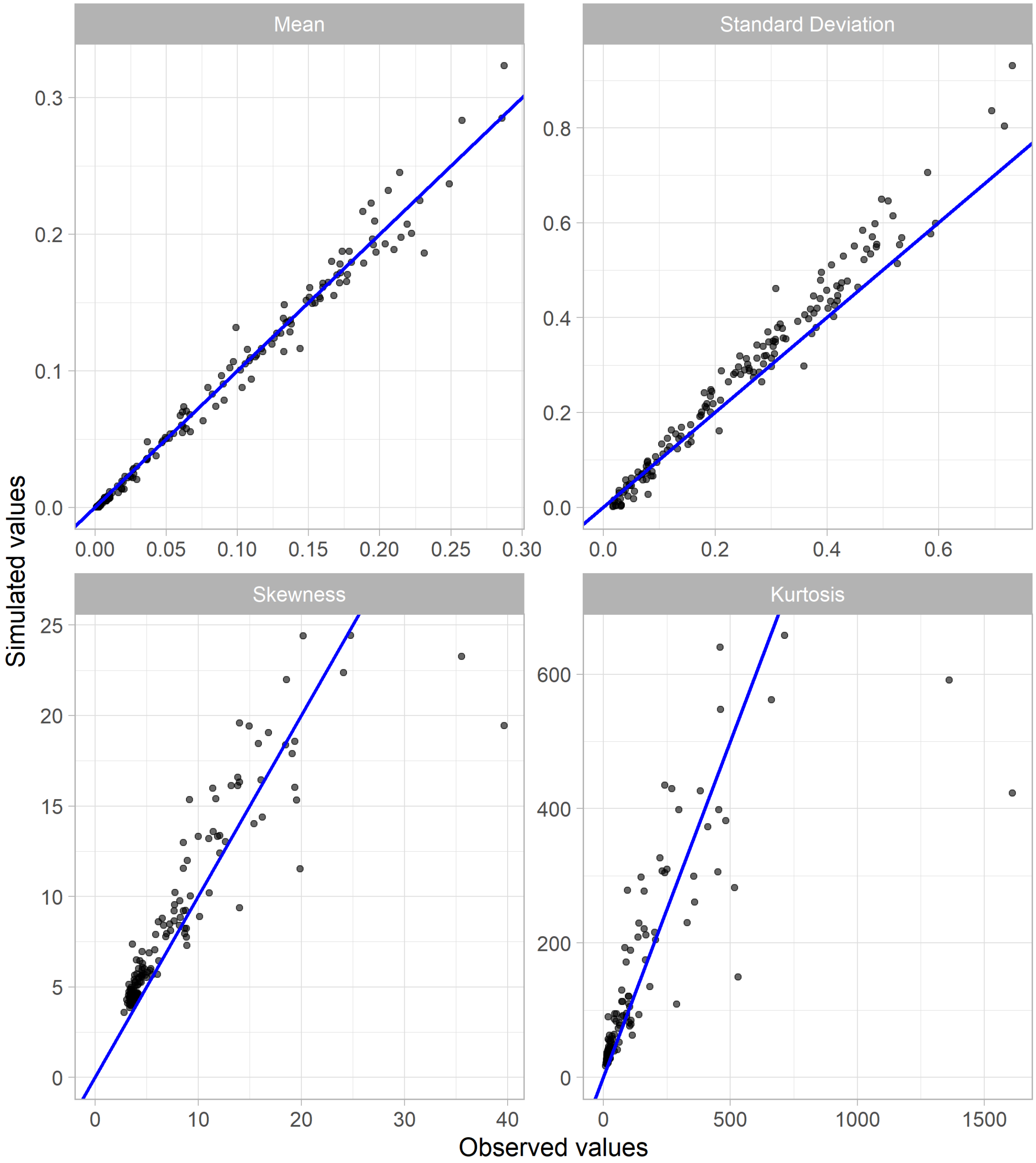

Figure 31. Daily performance statistics for precipitation for all possible combinations of gage stations (13 in total) and months, including the mean, standard deviation, skewness, and kurtosis. Median values across 1000 stochastic realizations are shown against the observed values. Observed values show daily values from the historical period 1956-2011. In each plot, the diagonal lines (slope=1 and intercept=0) is shown in blue color.

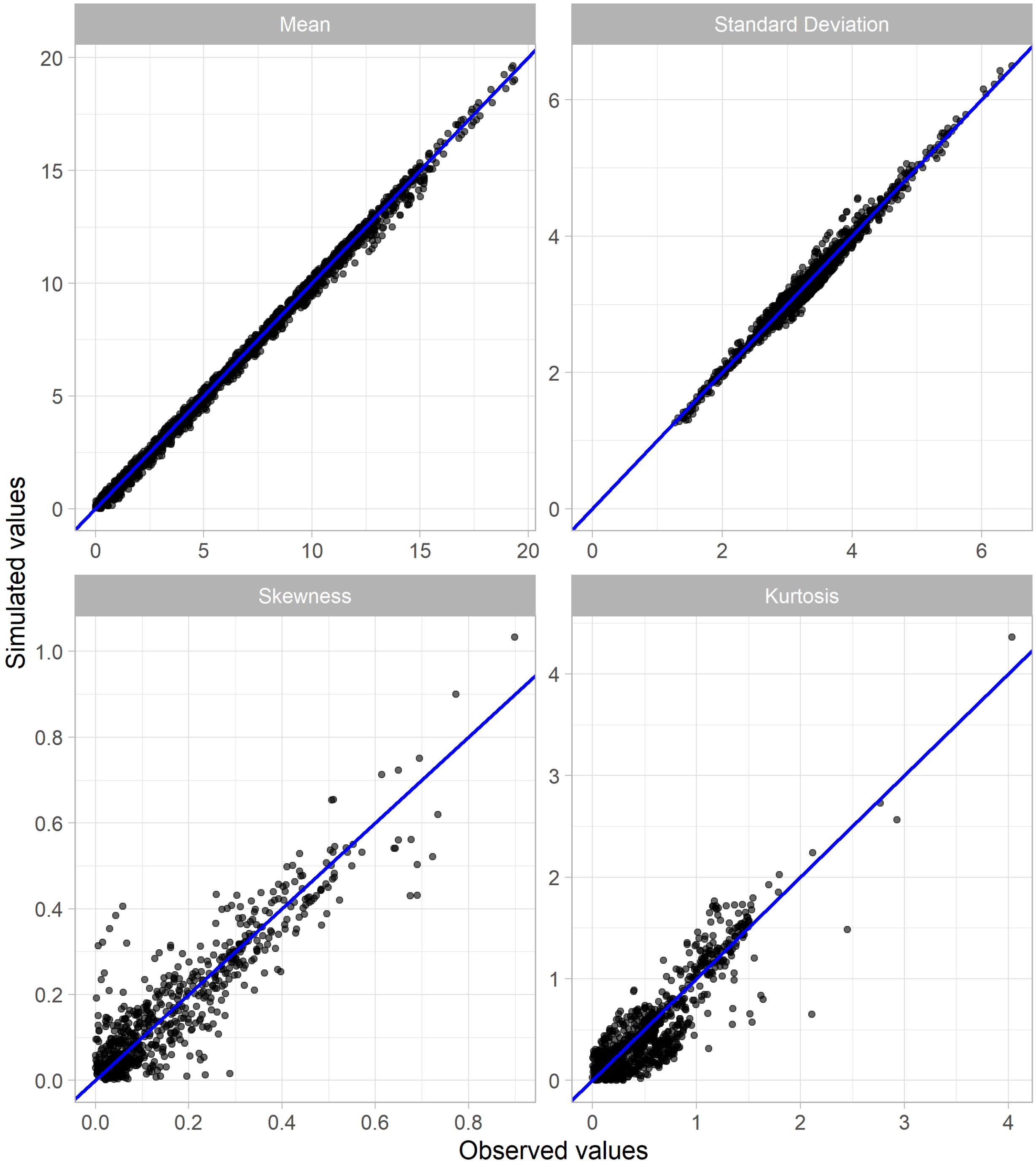

Figure 32. Daily performance statistics for minimum temperature for all combinations of grid cells (260 in total) and months, including the mean, standard deviation, skewness, and kurtosis. Median values across 1000 stochastic realizations are shown against the observed values. Observed values show daily values from the historical period 1956-2011. In each plot, the diagonal lines (slope=1 and intercept=0) is shown in blue color.

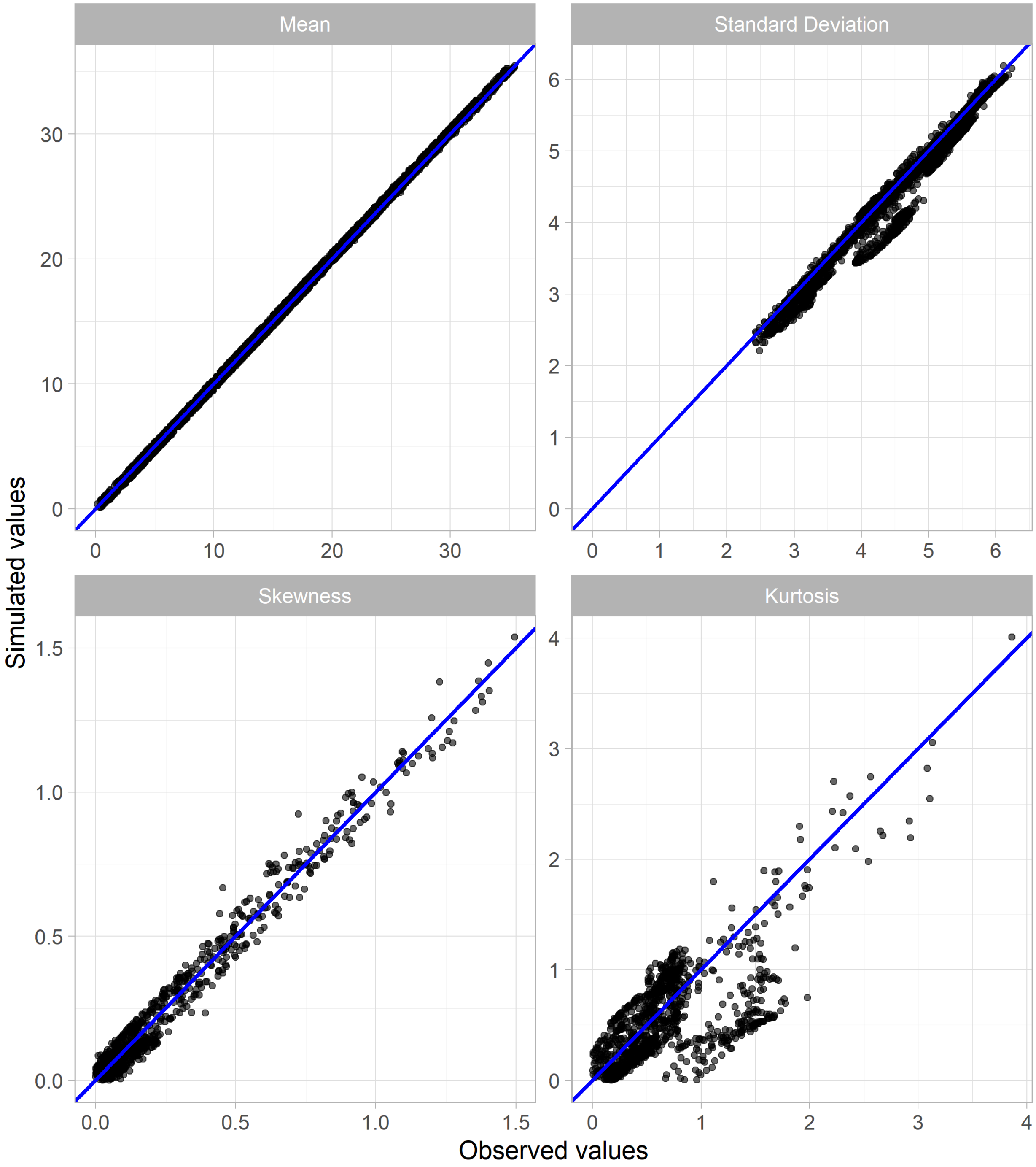

Figure 33. Daily performance statistics for minimum temperature for all combinations of grid cells (260 in total) and months, including the mean, standard deviation, skewness, and kurtosis. Median values across 1000 stochastic realizations are shown against the observed values. Observed values show daily values from the historical period 1956-2011. In each plot, the diagonal lines (slope=1 and intercept=0) is shown in blue color.

4. Analysis and Selection of Climate Realizations

The weather generation process, which consists of a wavelet autoregressive model coupled with spatial and temporal disaggregation methods provide multi-site, multi-variable daily climate realizations for the SFPUC region. The set of stochastic climate realizations obtained from the weather generator (1,000 in total) can be combined with climate change factors (see section 5) for stress testing the system under uncertainty from natural variability and climate change. In this work, this is done through a cascade of models including the SAC-SMA and PRMS hydrological models, which take climate as input and the water resources system operations model, which takes the outputs of the hydrology models as inputs. Application of the stress test procedure over a large sample of climate realizations (in this case 1,000) is time-consuming and computationally demanding. To address this issue, we select a smaller set of climate realizations from the initial database of climate realizations that can span the entire variability range.

In this section, we first show an analysis of climate realizations regarding drought severity and extreme precipitation to better understand the dataset. Next, we provide a methodology to select a smaller subset of "representative" and "interesting" realizations from the weather generator outputs.

4.1. Analysis of Climate Realizations based on Drought Severity

Given that droughts present an important challenge to the water utility's ability to meet water demand, drought severity measures can be used to evaluate and rank the set of climate realizations from the weather generator. We measure drought severity using the sequent peak algorithm, a critical-period analysis technique commonly applied in water deficit analysis in reservoirs (Thomas and Burden 1963; Loucks et al. 2005). We applied sequent peak analysis to determine the maximum cumulative departure from mean precipitation in each daily precipitation realization and sort the traces based on the calculated range of cumulative deficits values. The maximum cumulative precipitation deficit for each climate realization is estimated using the equations:

$$K_t = \max\{0,\ K_{t-1} + D_t - P_t\}$$

$$K^* = max\{\ Kt\ \}\ over\ all\ t = 1,2,\dots,t$$

where K_t is the cumulative precipitation deficit at day t, D_t is the mean annual precipitation at t, P_t is the precipitation at t, and K^* is the maximum cumulative precipitation deficit over the entire simulation period. Thus, K^* can be considered as a measure of drought severity, with higher values indicating prolonged periods of reduced rainfall.

To assess drought severity, we calculated K^* for each of the 1,000 climate realizations. In doing this, we focused on the Hetch Hetchy station due to its importance for the regional water resources system. Next, we rank the climate realizations in ascending order based on the computed K^*.

Figure 34 shows a histogram of K^* from 1000 realizations as well as the historical K^* value from the 1956-2011 period. K^* values from the stochastic realizations span from about 0.1 to 4.9 inches, exceeding the historical K^* value is 2.2 inches. This shows that the stochastic realizations provide a good coverage of possible range of drought severities (for the Hetch Hetchy gage station).

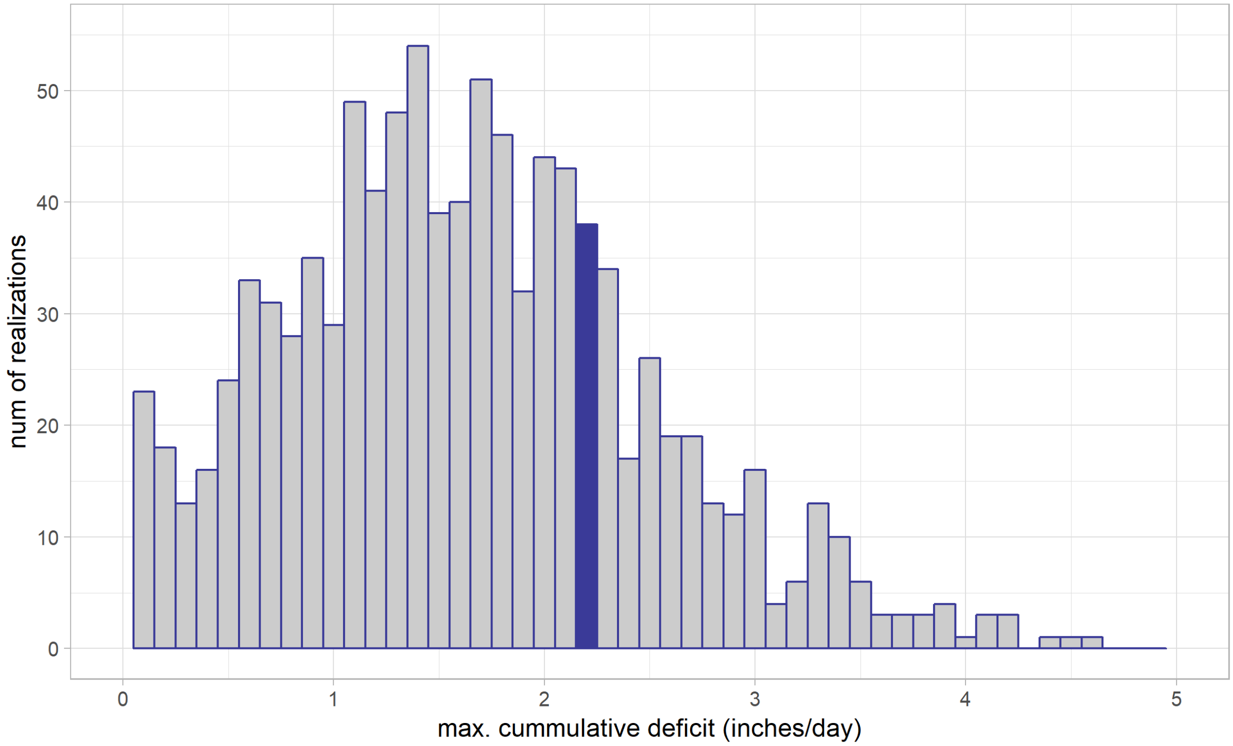

Figure 34. Histogram of K^* values from 1,000 stochastic realizations for the Hetch Hetchy gage station. The blue bar indicates the historical K^* value at 2.2 inches.

Figure 35 shows box-plots of K^* values from the same climate realizations for all of precipitation gage stations. The results are compared against the historical K^* for each station (shown in blue). Except for the HML station in East Bay, the stochastic realizations are able to provide more severe droughts than the historical period. Figure 35 also shows that in about eight out of thirteen gage stations, the historical drought severity is represented within the first and the third quartile range of the stochastically climate data.

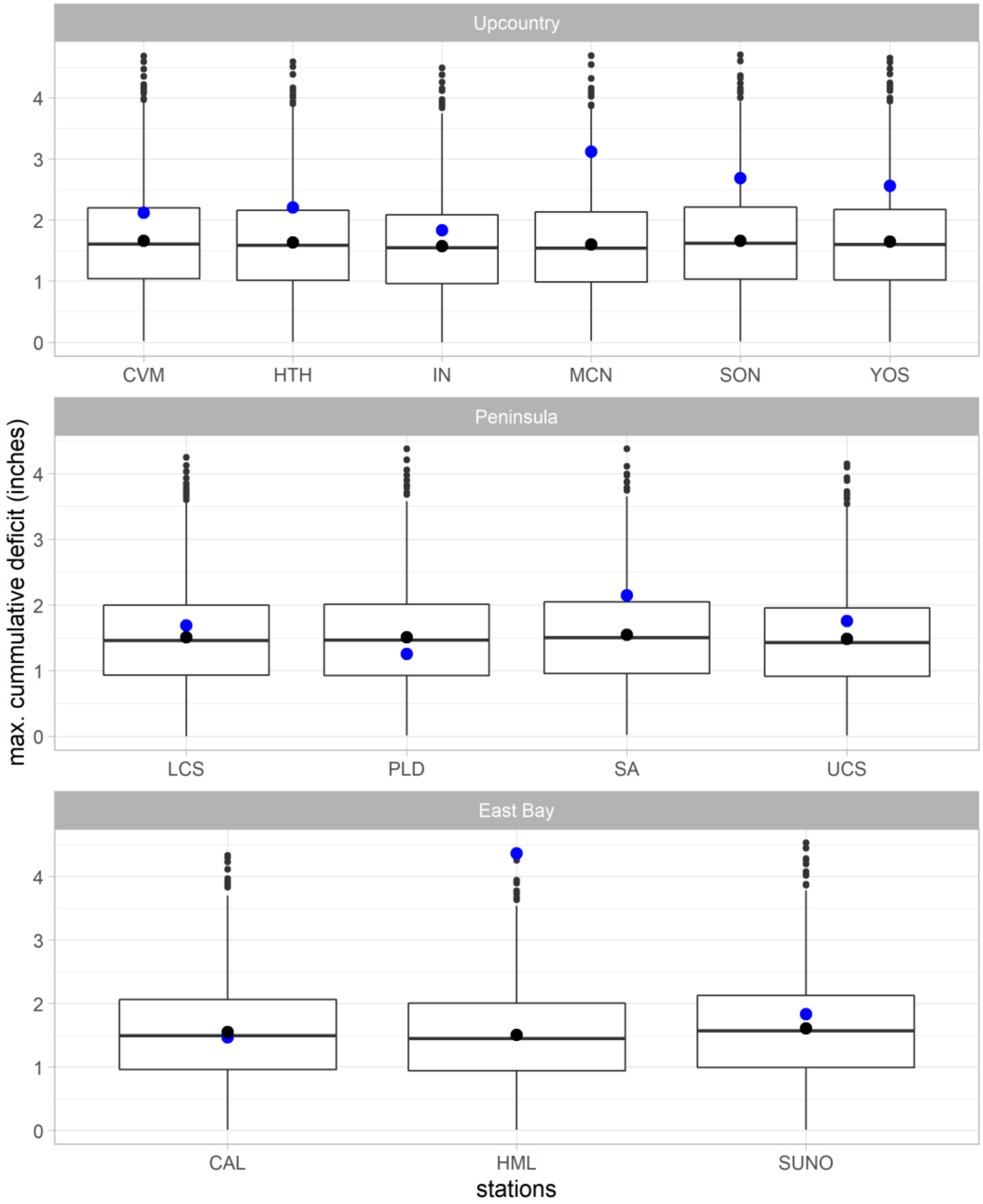

Figure 35. Calculated daily maximum cumulative deficit values (K^*) for the thirteen precipitation gages across the Upcountry, Peninsula, and East bay regions. The box-plots show K^* values from the seven representative traces selected. The blue dots show the K^* values calculated from the historical precipitation record (1956-2011) for each gage station.

4.2. Analysis of Climate Realizations based on Extreme Precipitation

In addition to droughts, extreme precipitation events are also a major source of concern for public utility services, which is also the case for SFPUC. We evaluate the same set of 1,000 climate realizations from the weather generator based on their ability to reproduce the observed precipitation extremes at the Hetch Hetchy gage station.

For the extreme precipitation analysis, we first define a set of critical thresholds at the 98th, 99th, and 99.9th percentiles of the historical monthly precipitation (1956-2011) (Table 6).

Table 6. Extreme precipitation threshold level defined based on monthly precipitation at the Hetch Hetchy gage (1956-2011)

	Percentile level	Historical precipitation at the given level
1	98 %	14.1 inches/month
2	99 %	16.1 inches/month
3	99.9 %	17.6 inches/month

Figure 36 shows the frequency of extreme precipitation events shown in Table 6, for the historical monthly precipitation at the Hetch Hetchy gage (1956-2011). Over the historical analysis period, the threshold of 14.1 inches/month is exceeded 14 times (Figure 36-a), whereas the threshold of 16.1 inches/month is exceeded seven times (Figure 36-b). There is only one precipitation event in the historical record that exceeded 17.6 inches/month (Figure 36-c).

Next, we show the occurrences of extreme precipitation across the set of 1,000 stochastic climate realizations. Figure 37 shows the histograms of extreme precipitation in the stochastic realizations for the same monthly extreme precipitation thresholds levels, i.e., 14.1, 16.1, and 17.6 inches/month, respectively. For the threshold of 14.1 inches/month, the number of extremes events in each realization ranges from 2 to 21, compared to the historical value of 14 (Figure 37-a). For the threshold of 16.1 inches/month, number of extremes are up to 14, about twice as many as in the historical period (Figure 37-b). Finally, for the threshold of 17.6 inches/month, number of extremes are up to 8 compared to one event in the historical record (Figure 37-c).

a) 14.1 inches/month (Percentile: 98%)

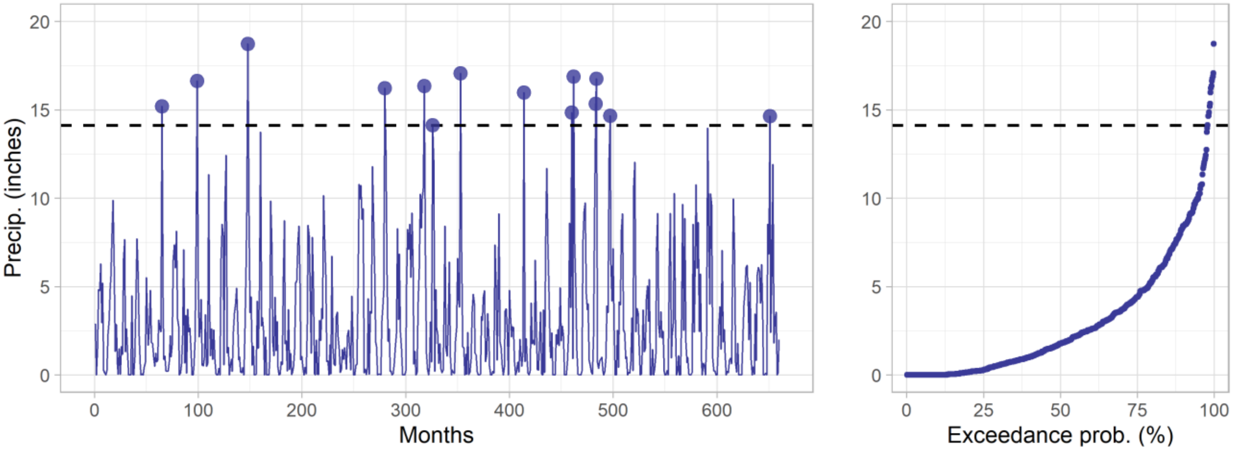

b) 16.1 inches/month (Percentile: 99%)

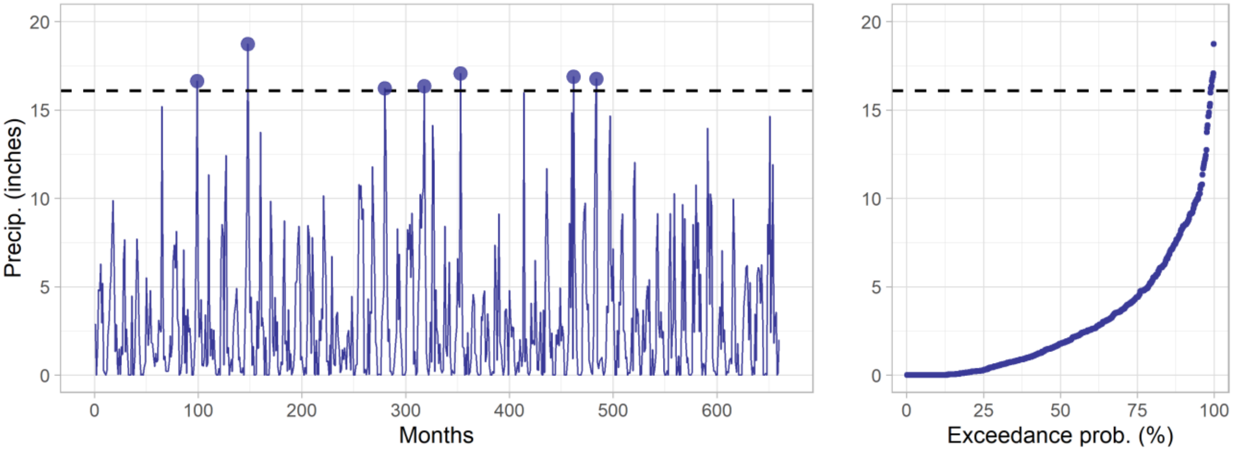

c) 17.6 inches/month (Percentile: 99.9%)

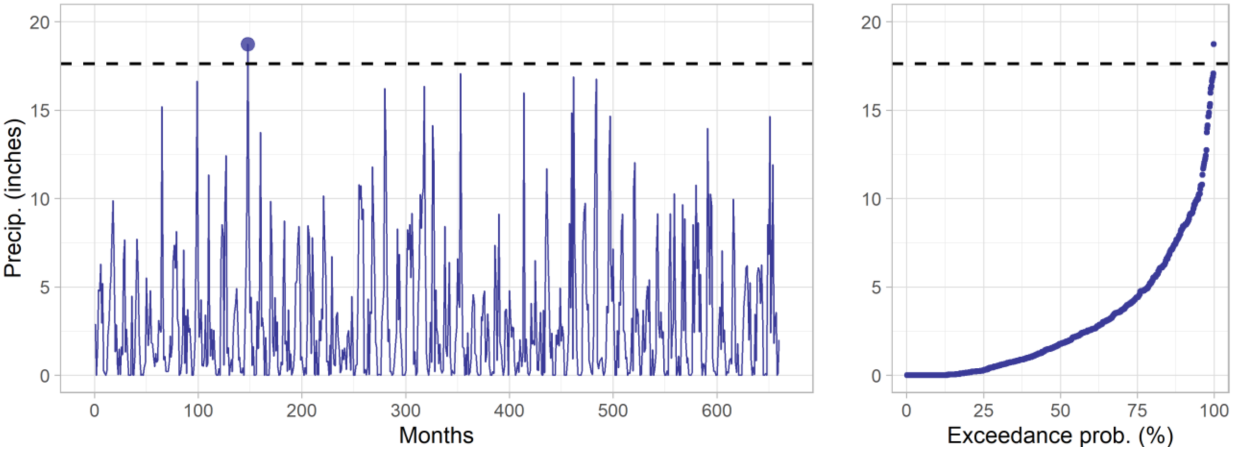

Figure 36. Time-series and exceedance probabilities for the Historical monthly precipitation at Hetch Hetchy gage (1956-2011). The horizontal dashed lines indicate the threshold values to set extreme events. Extreme values in a, b, and c are shown with blue dots.

a) 14.1 inches/month (Percentile: 98%)

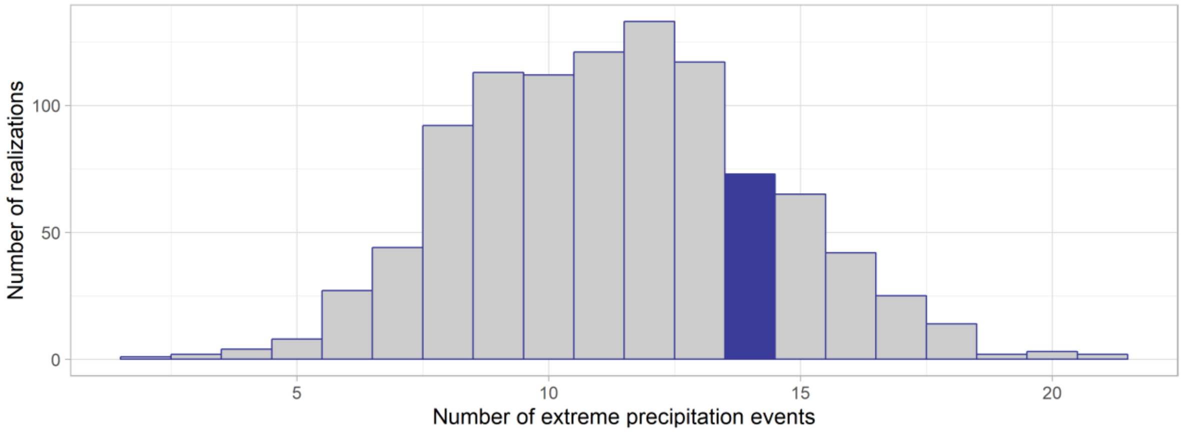

b) 16.1 inches/month (Percentile: 99%)

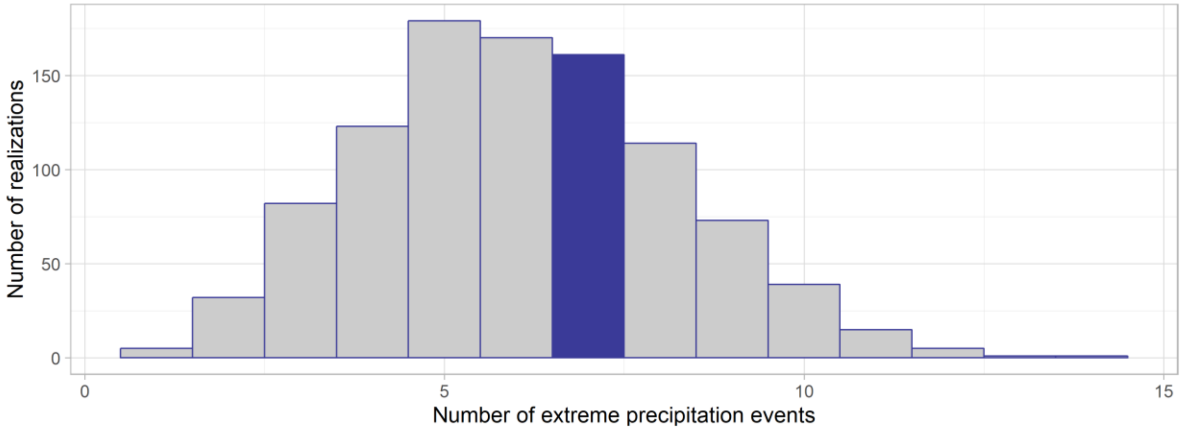

c) 17.6 inches/month (Percentile: 99.9%)

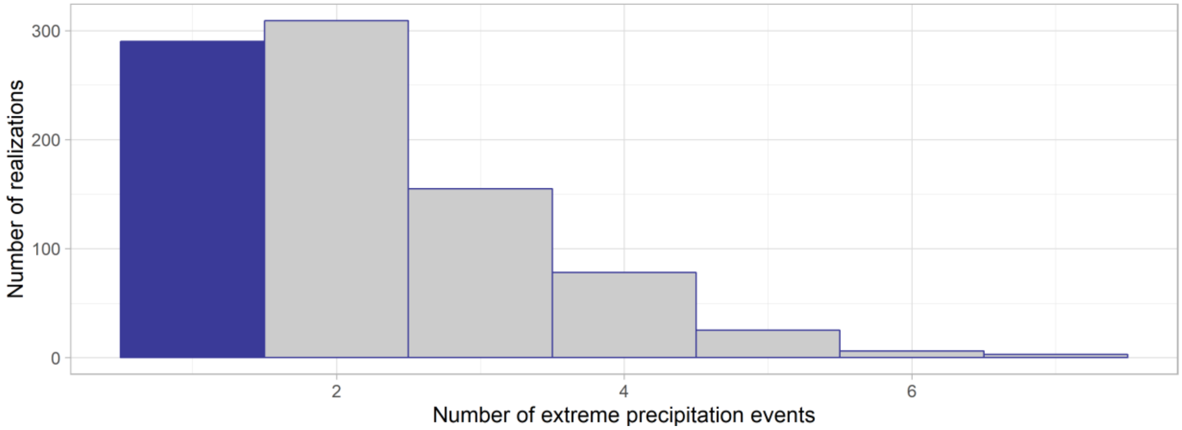

Figure 37. Histogram of extreme precipitation events across the set of stochastic realizations obtained from the weather generator. In a, b, and c, the bins show the count of monthly extreme precipitation events exceeding the given threshold value (x-axis) and the corresponding number of realizations associated with each bin. The blue bar represents the count of extremes in the historical record.

4.3. Subsetting Climate Realizations for the Stress Test

For the stress test analysis, we select a total of nine stochastic climate realizations among a set of 1,000 provided by the weather generator. During the selection process, we aim to cover a broad and a balanced range of possible climate climates that may occur in the future. This includes three representative or "normal" realizations that are similar to the historical record and a total of six realizations that represent realistic but extremely wet and dry futures (Figure 38).

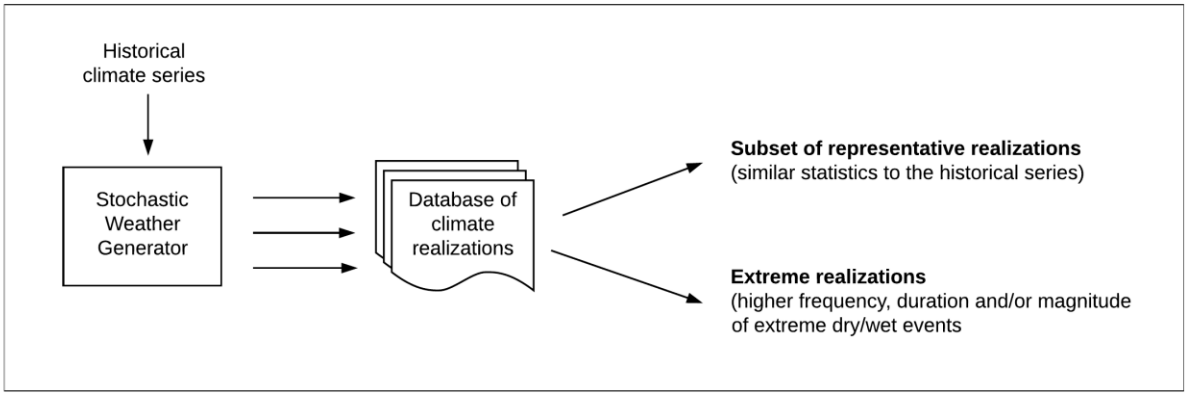

Figure 38. The process of subsetting stochastic climate realizations for the vulnerability analysis

4.3.1. Selection of representative climate realizations

For identifying realizations similar to the historical precipitation sequence, we first evaluate the first and higher-order statistics of the 1,000 stochastic realizations, including monthly means, monthly standard deviations, and maximum monthly precipitation as well as the daily maximum cumulative deficit of precipitation estimated using the sequent peak algorithm introduced previously. After this comparison, we identify three realizations that best represent the historical precipitation data at the Hetch Hetchy gage.

Figure 39 shows the boxplots of computed statistics from 1,000 daily stochastic traces in comparison to the historical values (red dots). The three selected realizations subsetted among 1,000 are shown by the blue dots. Monthly means of the selected realizations range from 3.02 to 3.05 inches, which shows a very good match to the historical value (3.025 inches). Standard deviation of the same three realizations range from 3.55 to 3.65 inches per month, which also matches very close to the historical value (3.6 inches). Selected stochastic traces are also similar to the historical trace in terms of monthly maximums, which range from 18 to 19 inches (historical = 18.5 inches), and maximum daily cumulative deficit, which is estimated to be same as the historical value (2.2 inches)

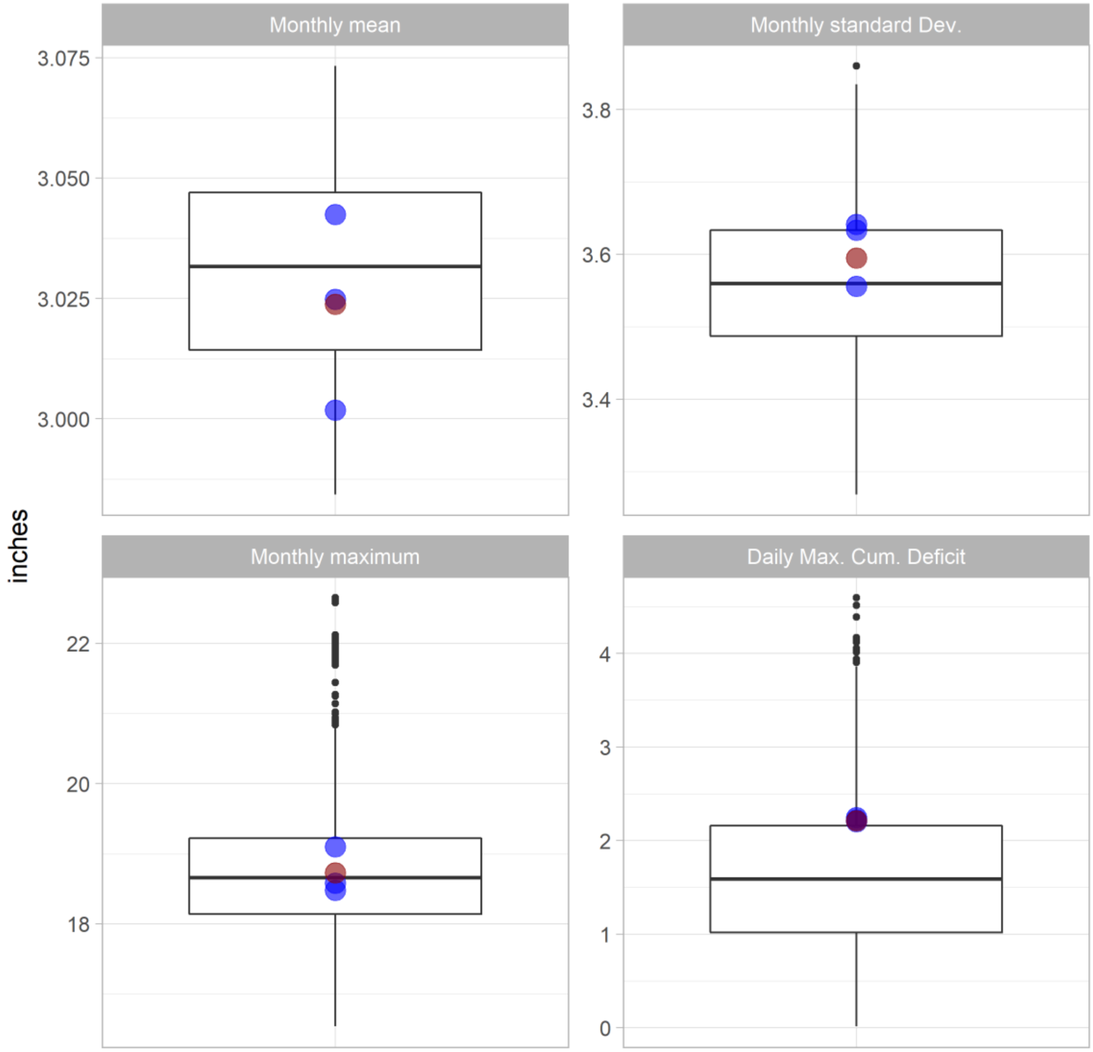

Figure 39. Box-plots of monthly mean, standard deviation, maximum precipitation, and daily maximum cumulative deficit of precipitation from 1,000 stochastic realizations (for Hetch Hetchy gage). Red dots indicate the historical statistics. Blue dots show the statistics of three selected stochastic realizations that show similar to the historical precipitation series.

Figure 40 displays the annual precipitation time-series at Hetch Hetchy gage for the three selected stochastic realizations in comparison to historical series. Figure 41 shows that these three traces also preserve the spatial correlations between the Hetch Hetchy, San Andreas, and Calaveras stations.

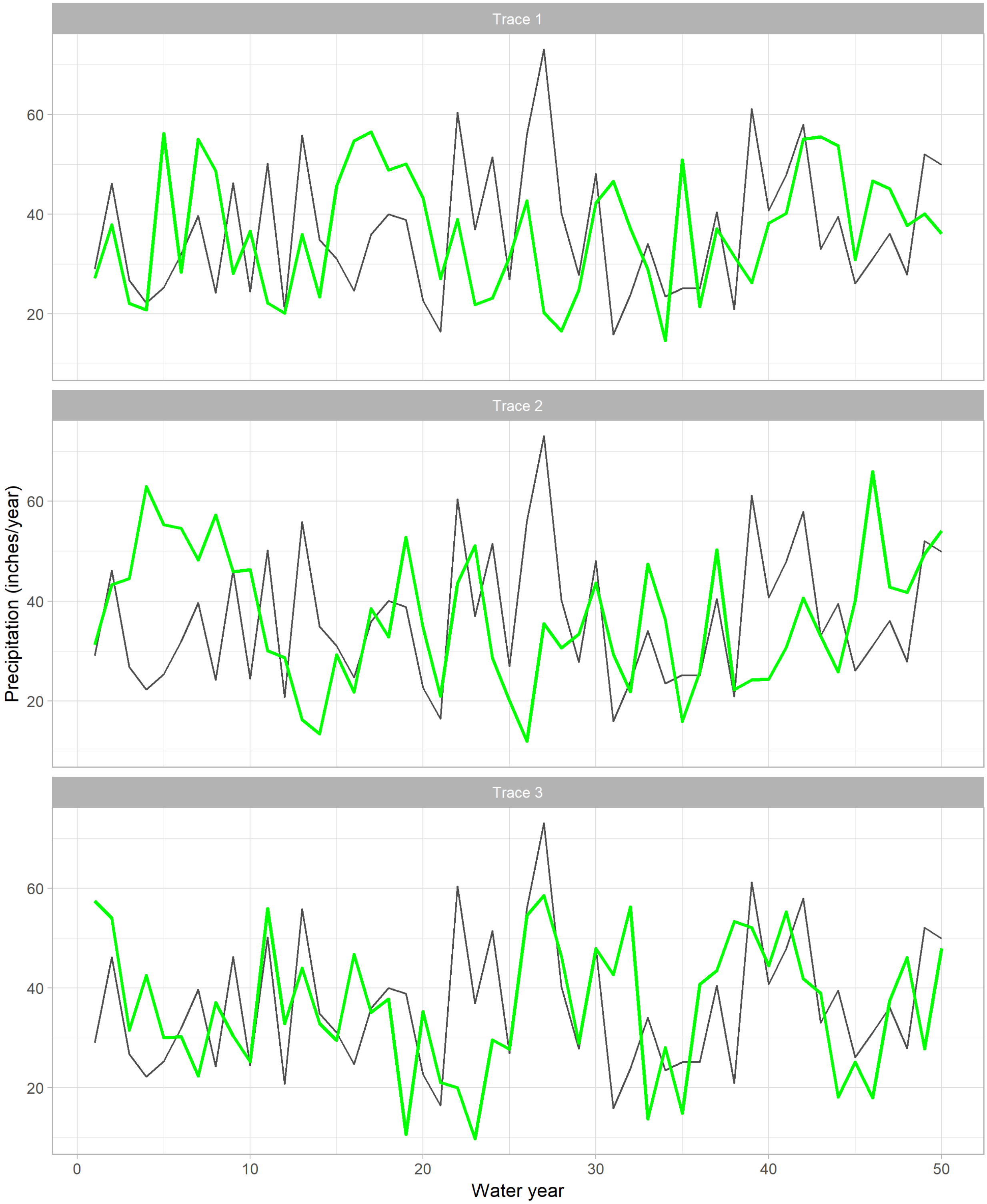

Figure 40 – Annual precipitation series from three selected climate realizations (in green) compared to the historical series from 1956 to 2005 (in gray). All values are for the Hetch Hetchy gage station.

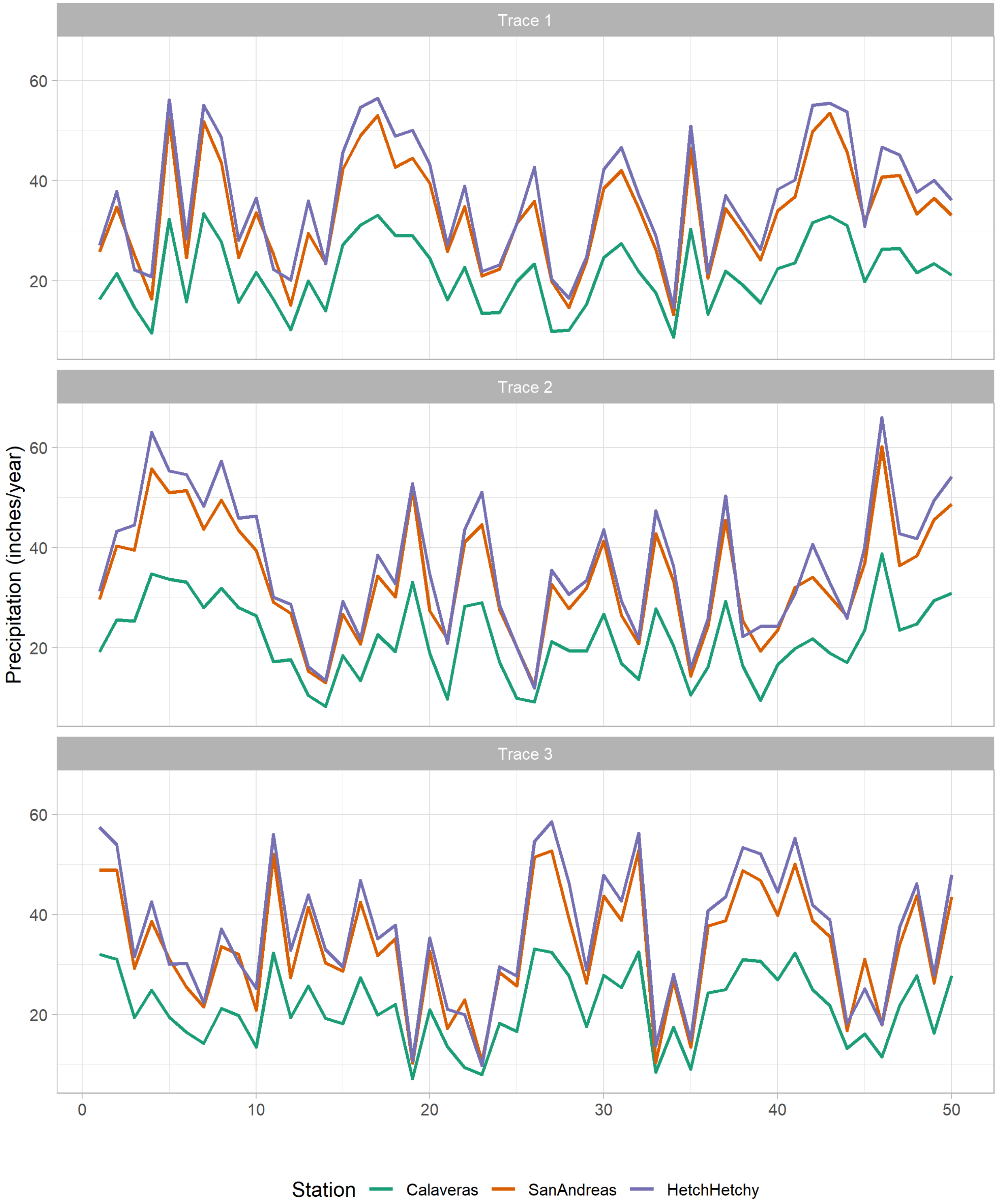

Figure 41. Three subsetted representative stochastic realizations from the weather generator results. For each realization, time-series at the Hetch Hetchy, Calaveras, and San Andreas stations shown by the indicated color.

4.3.2. Selection of extremely wet and dry climate realizations

In addition to the three representative natural variability realizations, we also sample a total of six extreme realizations that can challenging for the water resources system, i.e., in terms of droughts or floods. To define the extremee climate realizations, we first define extremely dry and wet events based on an analysis of historical annual precipitation series from the Hetch Hetchy gage (from the year 1956 to 2011). We define the dry and wet extremes based on the 95th and 95th percentiles of the empirical distribution of historical precipitation. These threshold values correspond to less than 18.3 inches/year and greater than 60 inches/year for the dry and wet extremes respectively.

Based on the specified wet and dry extreme thresholds, we then rank the set of 1,000 stochastic climate realizations based on three features:

i) Frequency of extremes, i.e., count of values below (or above) the threshold,
ii) Maximum duration of extremes, i.e., longest sequence of consecutive extreme values,
iii) Severity of extremes, i.e., maximum magnitude of extreme values

Based on these three features, we identify a total of realization that represent three extremely dry and three extremely wet realizations of the historical climate.

Figure 42 displays the three extremely wet realizations referred as Trace 4, 5, and six respectively. The first wet realization (Trace 4), has six extremely wet years, which is two times of the count of extremes in the historical record. The second wet realization (Trace 5) has a three-year wet event (at the years 36, 37 and 38), which can be challenging scenario for water system operations, i.e., flood control. Finally, the third realization (Trace 6) has a single wet year with a total precipitation of about 87 inches/year, which corresponds to a return-interval of about 200 years.

Figure 43 presents three extremely dry realizations referred as Traces 7, 8, and nine respectively. Trace 7 has six extremely dry years (< 18.3 inches/year), which is three times of the historical series. Trace 8 has a 3-year prolonged drought at years 39, 40, 41. If one considers the low precipitation years before this sequence (years 37 and 38), the specified drought can be considered as a 5-year drought. Finally, Trace 9 has a single year extreme drought, in which the total precipitation is less than 5 inches/year. This rare drought corresponds to a return-interval of about 10,000 years.

Overall, these six extremely wet and dry traces provide a rich representation of stochastic (natural) variability of the climate in addition to the three representative traces previously shown.

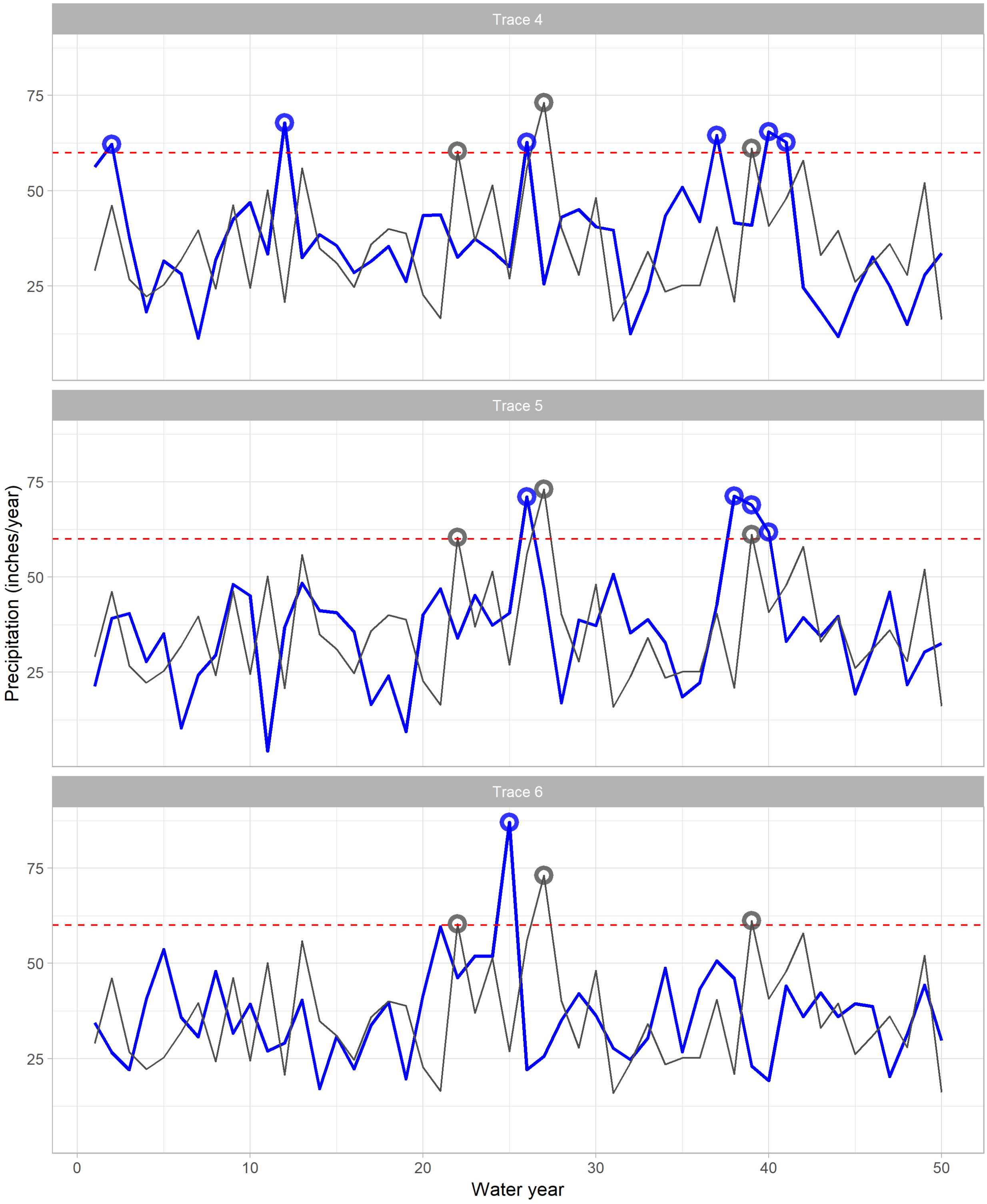

Figure 42. Three extremely wet climate realization identified from the weather generator outputs. The stochastic traces are shown in blue. Historical climate (1956-2005 interval) is shown in gray color. The red dashed line marks the threshold of 60 inches/year

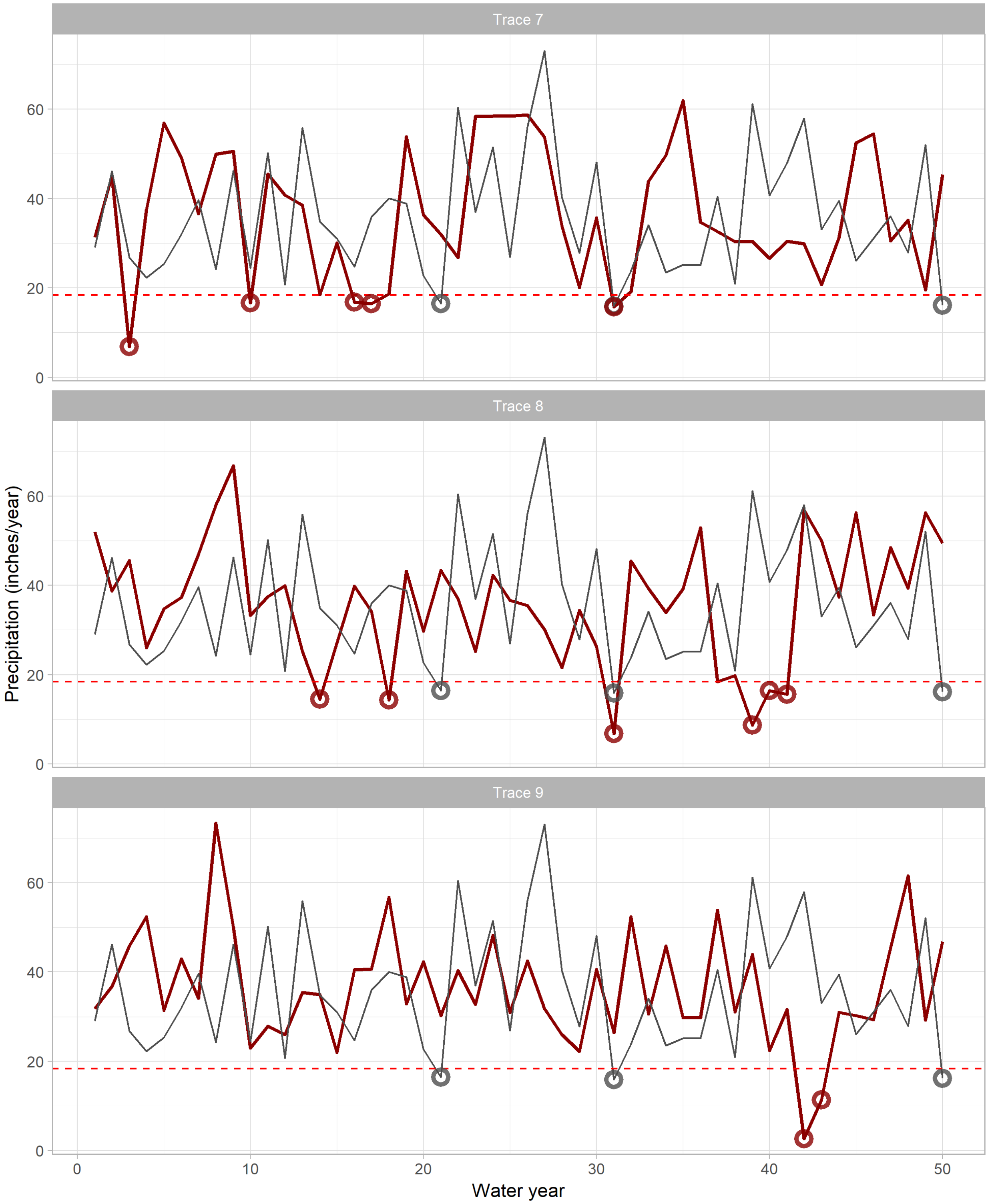

Figure 43 Three extremely dry climate realization identified from the weather generator outputs. The stochastic traces are shown in blue color. Historical climate (1956-2005 interval) is shown in gray color. The red dashed line marks the threshold of 18.3 inches/year

Finally, selected statistics of the nine natural variability realizations sampled from the weather generator outputs are summarized in Table 7.

Table 7. Selected statistics of the precipitation series from the nine stochastic climate realizations selected from the weather generator outputs. Historical series show the same statistics from the observed precipitation record (1956-2011 period). Stochastic minimum and maximum represent the range of statistics computed from 1,000 stochastic realizations. All values are based on the results at the Hetch Hetchy station.

	Type of stochastic realization	Monthly mean precip. (inches)	Monthly Standard deviation of precip. (inches)	Monthly maximum precip. (inches)	Daily max. cumulative deficit of precip. (inches)
Trace 1	**Representative (normal)**	3.04	3.63	19.10	2.20
Trace 2		3.02	3.56	18.58	2.22
Trace 3		3.00	3.64	18.48	2.24
Trace 4	**Extremely wet**	3.05	3.67	18.10	0.61
Trace 5		3.01	3.52	18.30	3.01
Trace 6		3.04	3.46	17.68	2.13
Trace 7	**Extremely Dry**	3.05	3.45	17.88	1.43
Trace 8		3.00	3.45	18.47	2.89
Trace 9		3.02	3.44	18.23	1.09
Historical series		3.02	3.60	18.70	2.20
Stochastic minimum		3.00	3.30	16.50	0.01
Stochastic maximum		3.10	3.90	22.60	4.59

5. Climate Change Projections and Scenarios

In this section, we evaluate most recent climate projections across the SFPUC RWS region based on the data from the Global Coupled Model Intercomparison Project phase 5 (CMIP5, Taylor et al. 2012). We then consider this information to evaluate the possible range of mean changes in long-term precipitation and temperature for perturbing the natural variability realizations presented in the previous section. The work presented here is a joint effort of the University of Massachusetts Amherst team and the National Center for Atmospheric Research (NCAR). The analysis is structured into three high-level parts: i) a brief description of temperature outlooks and ii) more in-depth analysis of the projections of precipitation, and iii) a summary of projected changes.

5.1. Temperature Projections

Figure 44 summarizes the GCM multi-model spatial projection of temperature change across the western half of the US (including the SFPUC region) at mid-century. Most changes are seen in areas with snow feedback (winter in high-latitudes and continental interiors) and high elevations (all seasons), while the smallest changes are expected over the oceans. The magnitude of this warming by mid-century (~2050) varies slightly between models: ~2 to 2.50 ºC in the Upland and 1.5 to 2 ºC close to the ocean in the lowland. The seasonal variations of this robust change are fairly small.

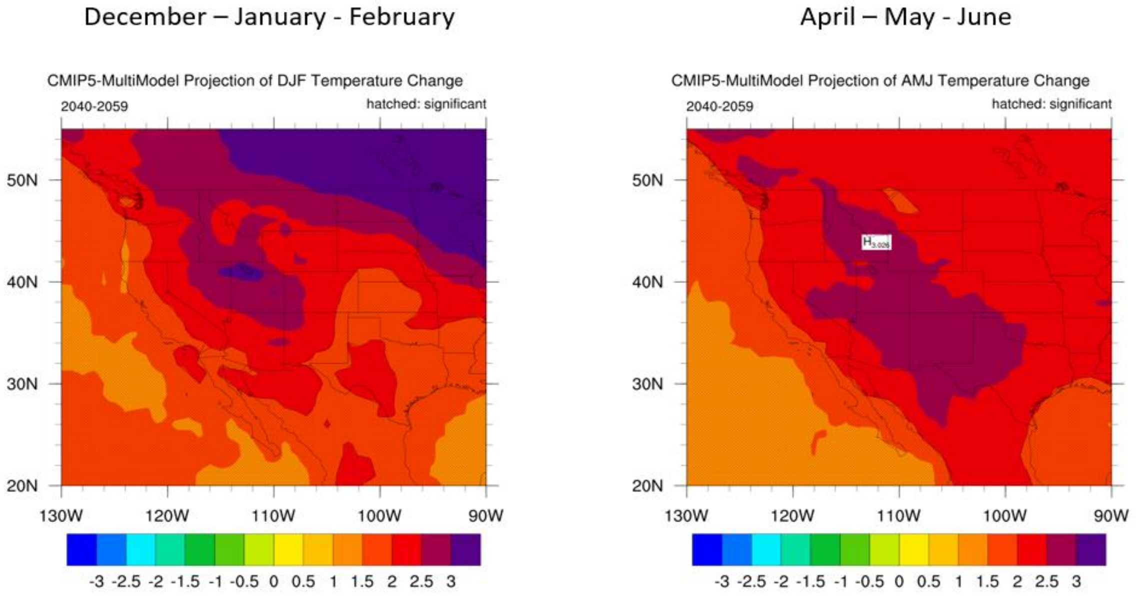

Figure 44. **The projected changes in cold season precipitation as the CMIP-5 multi-model average.**

Figure 45 shows the changes to the monthly mean absolute temperature climatologies for the three 30-year periods (1981-2010, 2011-2040, and 2041-2070) for a location in the Southern Sierra near Hetch Hetchy as represented in the bias-corrected BCSD dataset. The plot suggests a robust warming signal across all months of the year and an increase of warming as time progresses. January's mean temperature for the 1981-2010, 2011-2040, and 2041-2070 was -3.3ºC, -2.2ºC, and -0.9ºC respectively; while the July mean temperature for the same periods were, 15.5ºC, 16.9ºC, and 18.6ºC respectively. Note, the larger the projected mean changes, the broader the model spread, likely related to the differences in elevation in the models. Key is that the changes are systematic across models, despite internal climate variability (in contrast to precipitation, see below).

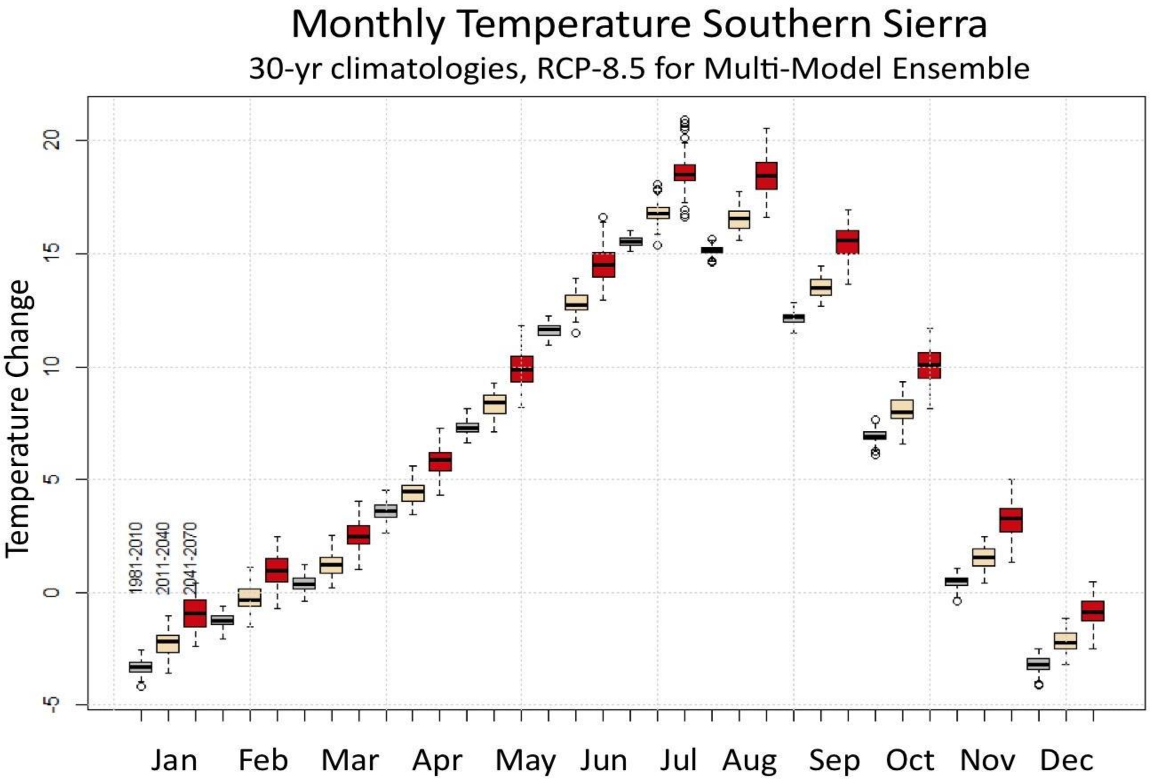

Figure 45. The projected changes in mean monthly temperature across a CMIP5 multi-model ensemble for the periods of 1981-2010 (gray), 2011-2040 (yellow) and 2041-2070 (red) as bias-corrected in the BCSD archive for more accurate absolute values.

On inter-annual time scales, the variability of temperature appears to be increasing slightly as time progresses, although the change is not significant. Looking at KNN-results conditioned on CMIP5 models, Figure 46 indicates that the range across the models increases as the different models exhibit slight differences in the mean warming trajectory (due to different climate sensitivity as well as differences in regional dynamical changes). When examining the inter-quartile range, the distribution of annual mean temperatures in the CMIP5 models is slightly larger for future periods than for the evolving present day window, and the overall warming trend over the period 2041-70 is faster than over the "current' 1981-2010 interval.

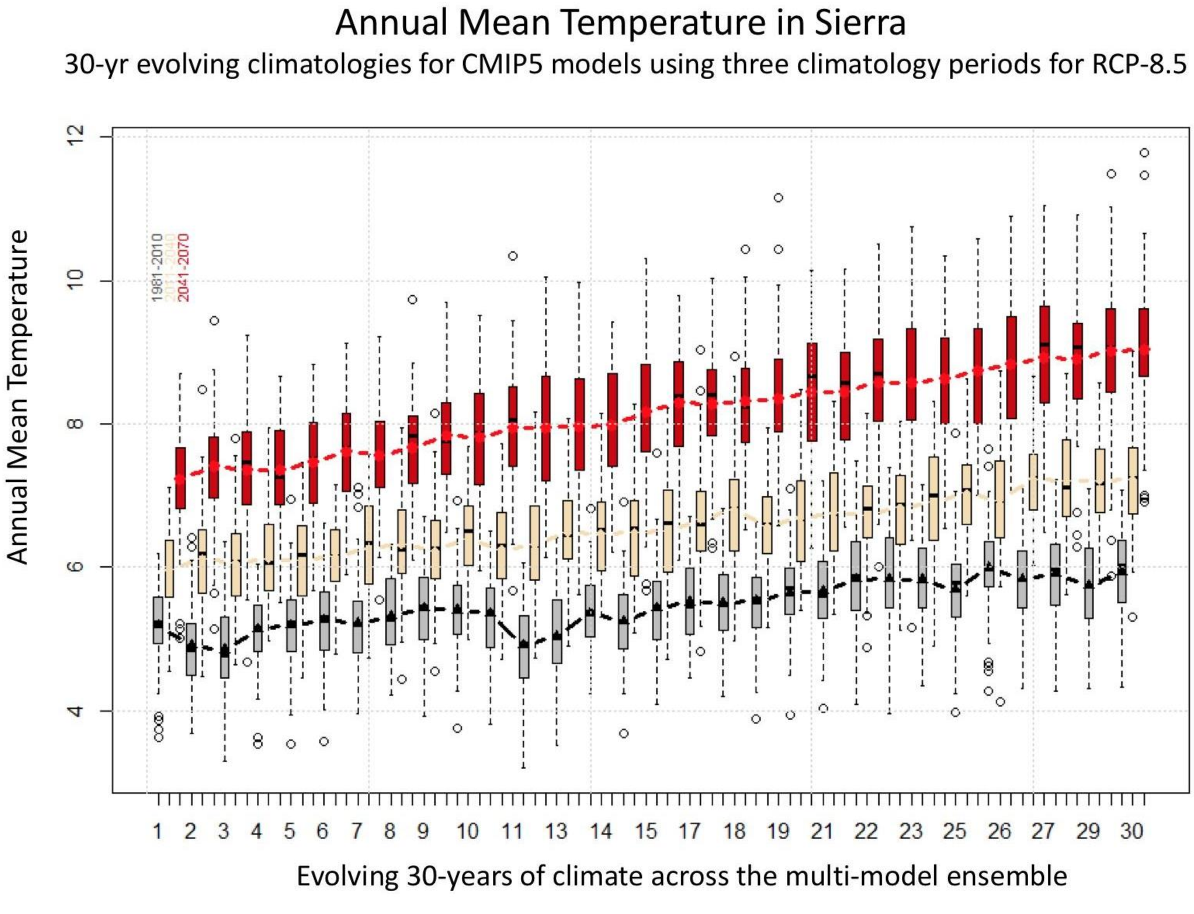

Figure 46. The projected changes in mean annual temperature across a CMIP5 multi-model ensemble for the periods of 1981-2010 (gray), 2011-2040 (yellow) and 2041-2070 (red). Each year in the 30-year sequence is represented by the distribution across 70 GCM simulations that got bias-corrected through the BCSD method.

As discussed above, the changes seen in temperature are robust and showing a systematic warming across time in all consulted datasets. In the BCSD historic ensemble, the mean is 5.45ºC, while the 2011-2040 ensemble mean is 6.6ºC, and the 2041 to 2070 ensemble mean is 8.2ºC. Figure 3 offers insight into the evolving nature of these changes (note, the segments connect seamlessly if assembled in sequence).

In summary, temperatures are clearly projected to increase across the SFPUC domain. The changes by the 2050s are expected to be around 2 to 2.5 ºC, with the upland locations possibly slightly higher. Towards the end of the century, the changes could reach as much as 4 to 5ºC under the assumption of an RCP-8.5. The seasonal distribution of these changes is to a first order uniform, though locally in the high Sierra where snow feedback can operate, larger values can be expected during the shoulder seasons and in winter.

5.2. Precipitation Projections

We analyzed the precipitation projections with an eye towards aspects that are both important for water resource management, and that might exhibit more systematic signals, although the observation of non-significant change including variability within a range experienced during the recent past, is also a useful result for the current climate change assessment.

Figure 47 shows the monthly average climatologies derived in the bias-corrected BCSD archive for the three 30-year periods over the Southern Sierra region that includes Hetch Hetchy. Figure 48 shows the projected anomalies relative to the present-day baseline for the direct GCM output. While individual months don’t necessarily appear highly robust in showing a change, when taken together across the seasonal cycle, a more systematic image appears: A clear seasonal evolution of the mean and median anomalies with relatively wet winters and much drier summers is seen. The two future periods show the GCM-derived projected changes in monthly precipitation suggesting increasing winter-time precipitation as reflected in the multi-model median as well as the inter-quartile range. The other period of increase is during summer, though the absolute values are diminishingly small. However, these two periods are separated by shoulder seasons that show a clear tendency for drying, namely between April, May, and June, as well as September, October and November.

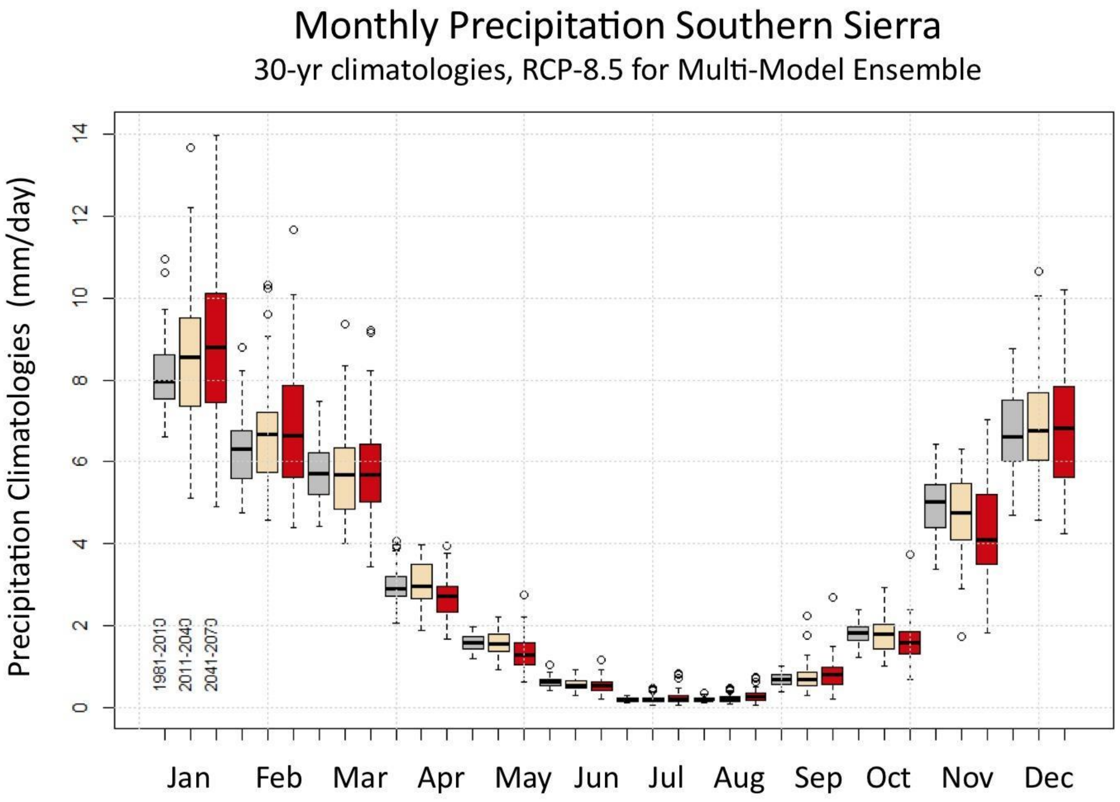

Figure 47. The projected changes monthly mean precipitation across the year in the CMIP5 multi-model distribution as represented in the BCSD archive for the high elevation location of the Southern Sierra.

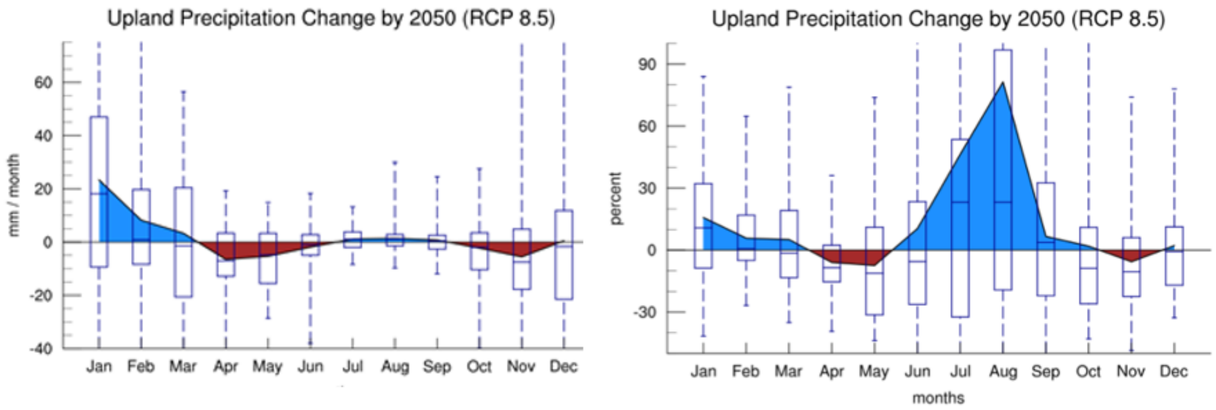

Figure 48. GCM projected changes in mm/month (left panel) and percent changes (right panel) compared to the present-day baseline. Clearly seen are the increases during the core winter and summer season and decreases in the shoulder season. The large percent change in summer is an artifact of the very small absolute values of precipitation

Figure 49 shows the inter-annual precipitation variability from the CMIP5 projections. The figure shows the interannual spread by the running average across the different GCMs that are fully overlapping. The demonstrated inter-annual variability in the SFPUC region can mask a possible signal from climate change as in other regions (Deser et al. 2012).

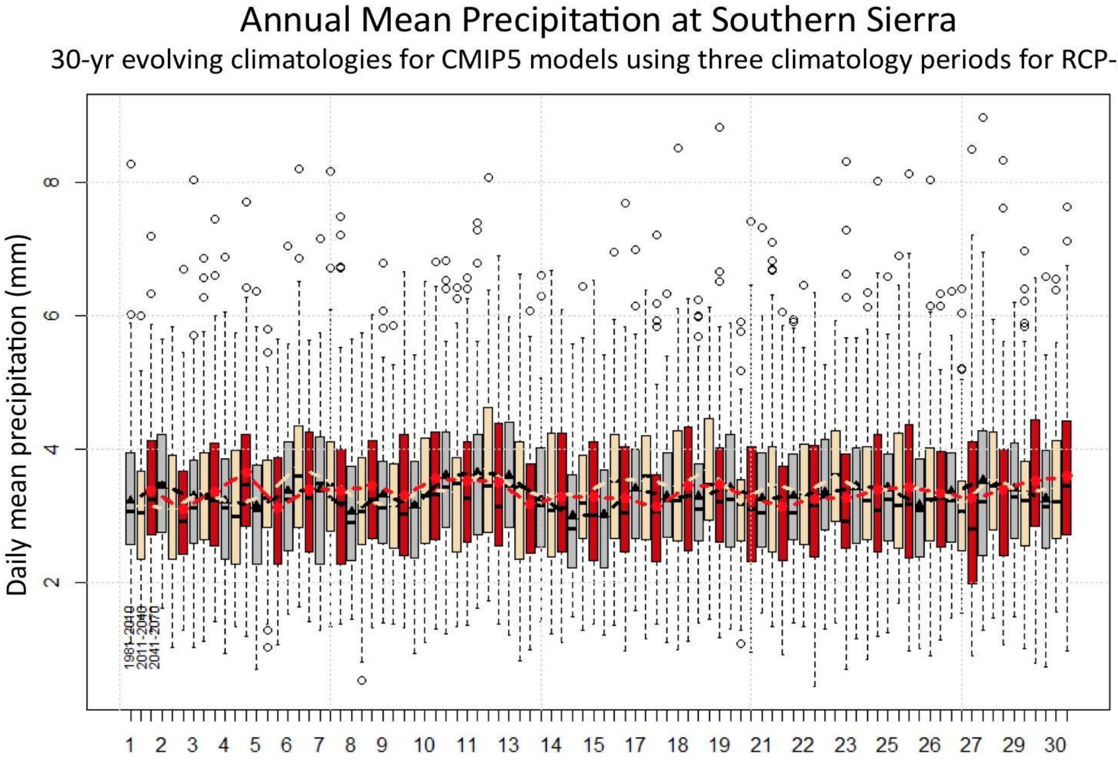

Figure 49. Projection of annual mean precipitation for three 30-year climatological periods (1981-2010 light gray, 2011-2040 tan, and 2041-2070 brown) for the upland location of the SFPUC domain. Each box represents 70 samples from the BCSD data archive. The running mean values across the 30-year intervals are shown as lines.

Although the mean precipitation change over the broader Hetch Hetchy Watershed shows a slight increase, the coherence of this signal across models is much lower than in regions further to the north (and much further to the south). Therefore, it is important to ask the question if the changes are in any form significant. Figure 50 illustrates significance using the approach applied in the IPCC report (Stocker et al., 2013, building on Tebaldi et al., 2011), where color is applied only in areas where at least two thirds of the models agree on the sign of change (the upland section of the SFPUC domain falls just outside of that area), and when additionally requiring a statistically significant deviation from the present day distribution using a 90% confidence, then only small areas inland and off the coast of Oregon fulfill these criteria along the West coast of North America (hatched areas in Figure 50).

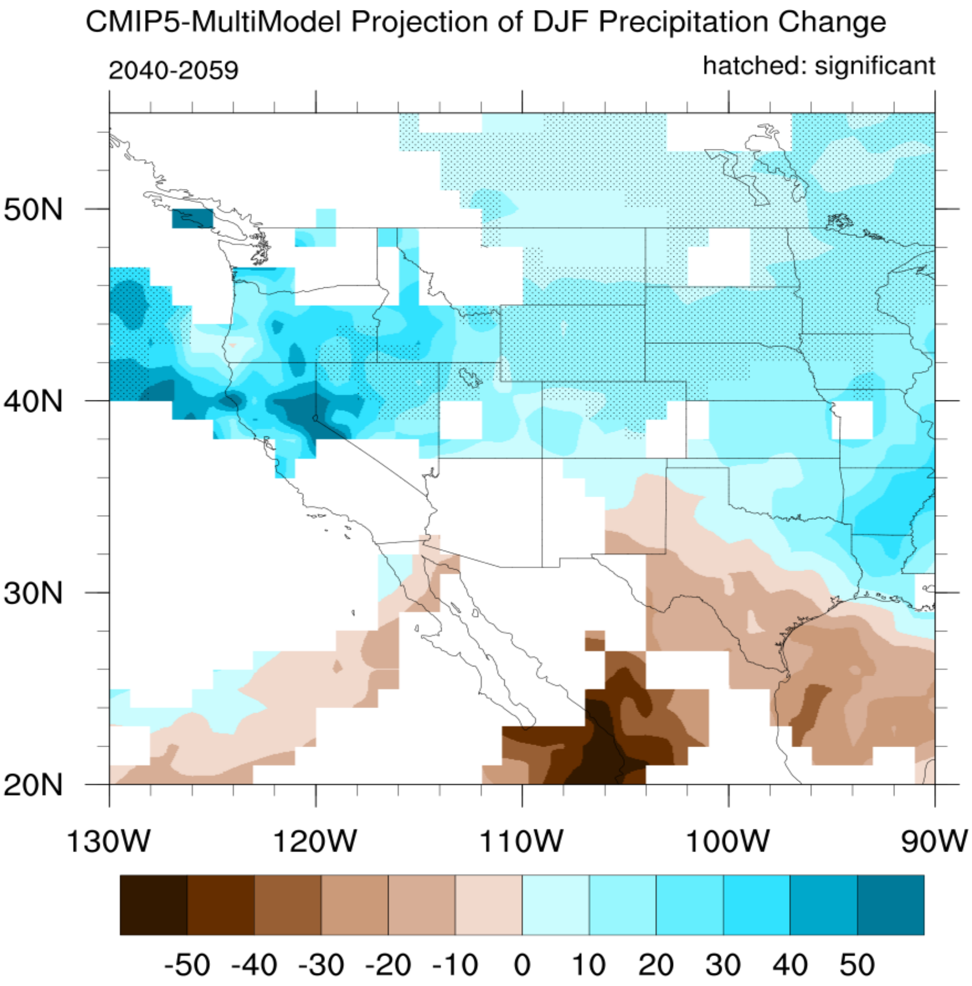

Figure 50. Projection of change in winter (DJF) precipitation for 2050 over the North American West. Colored areas indicate at least two-thirds of models agree on the sign, and hatched areas additionally fulfill significance criteria at the 90% confidence level.

Figure 50 broadly outlines the dynamical feature of expected changes in the hydrologic cycle. Higher latitudes will very likely see an increase in precipitation due to an increase in transport of moisture in warmer air. The subtropical areas are more likely to see a decrease in precipitation due to enhanced downward motion in the descending branch of the Hadley cell. Based on the different climate model's depiction of this constellation, the intersect between these two large-scale domains falls somewhere over Southern and Central California. The SFPUC domain is near the positive precipitation domain (the Bay is actually within it), and thus can be considered to be somewhat more likely to see positive than negative precipitation in the near future. This outlook appears consistent with the changes discussed above regarding the seasonal cycle. Positive trends during winter (Dec - February) align with the more robust trends to the north of the SFPUC domain. But because of the high variability, the significance of these changes in the means remains low.

When considering only the maximum precipitation events, however, then a trend towards higher values is apparent. Figure 51 illustrates the BCSD-derived maximum monthly precipitation for each year annual precipitation for the Southern Sierra with an increase over the coming decades in both the expected value (median and mean maxima) as well as an increase in spread reflecting the heavy tail of the distribution of these maxima.

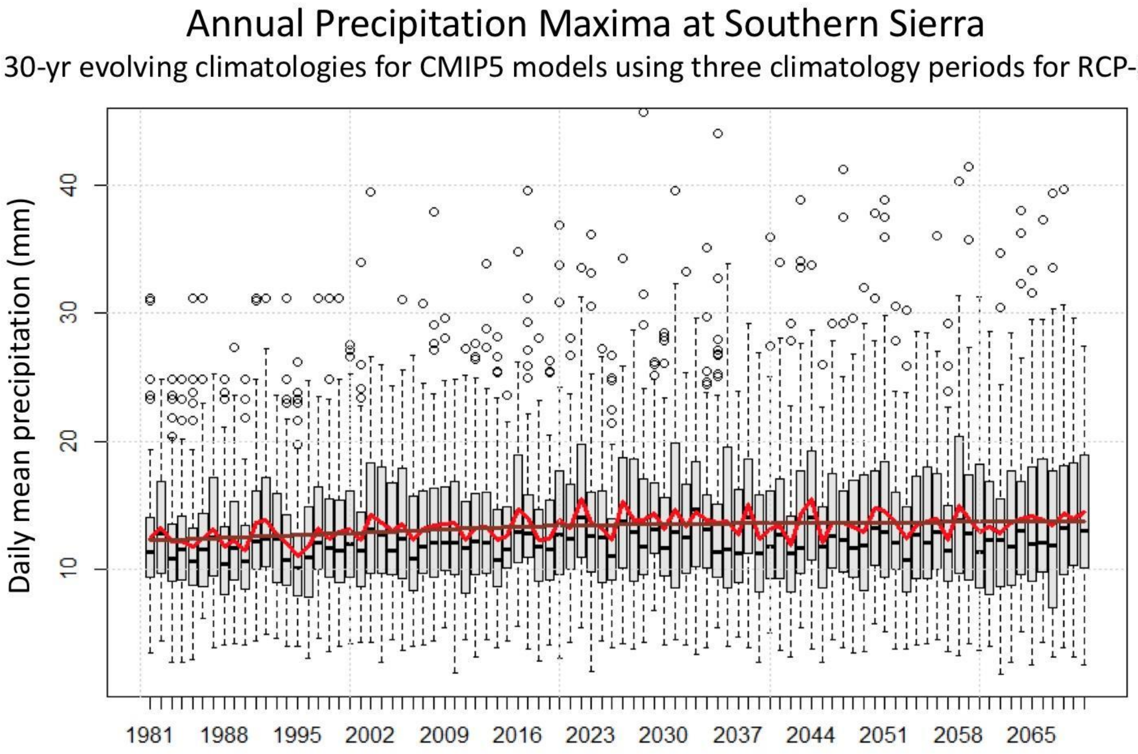

Figure 51. Projection of change in annual maximum precipitation (in mm/day) for the Southern Sierra showing an increase from 12 to 14 mm.

5.3. Summary of Projected Changes

In this section, we aimed to identify systematic changes that can be linked to underlying physical processes to strengthen the confidence in the projections. While temperature changes appear highly robust across all time scales, changes in precipitation are less certain and require separation into different components. Long-term mean precipitation appears not statistically significant; we nevertheless consider it more likely that the average might increase than a decrease. However, the interannual variability is also likely to increase, supporting the notion that in a warmer world the enhanced hydrologic cycle shows wetter conditions when wet and drier conditions when dry. Most importantly, high-intensity precipitation events are likely to increase in frequency and intensity.

Table 8. Overview of identified changes. 2010-2040 and 2025 mean, and 2041-2070 and 2050 mean.

Climate Variable	GCMs	BCSD	WRF-CONUS
Temperature - annual	2025: Upland: Lowland: 2050: Upland: +2 - +2.5 Lowland: +1.5 - 2	2025: Upland: +1 2050: Upland: 2-3	*2085:* *Upland: +4 - +5* *Lowland: +3.5 - + 4*
Temperature - seasonal mean		Seasonal cycle	
Precipitation - annual	non-significant	non-significant	
Precipitation - seasonal mean	DJF: positive, +10% Jan MAM: negative, -10% Apr JJA: positive, miniscule SON: negative, -10% Nov	Similar: DJF: positive, +10% Jan MAM: negative, -10% Apr JJA: positive, miniscule SON: negative, -10% Nov	DJF: +10% upland
Dry days / Wet days	MAM: increase in dry days, and potential decrease in 4-day (longer) events.		
Maximum Monthly precip		Increase ~10% from 12 to 14 mm/day	
Extremes	Increase across tails		
Whiplash	~10% increase in transition intensity		

Figure 52 shows the scatter plot of annual mean climate changes from the CMIP5 ensemble for the 2020-2070 period relative to the historical period of 1960-2010. The climate projections show a relative increase in temperature up to about 4°C for East Bay and Upcountry regions and about 3°C for Peninsula. However, in all regions, projected temperature changes are clustered around 1-2 °C. Similar to other regions in the globe, model projections for precipitation change is highly uncertain across the three regions, with no clear direction. Projected range of changes in precipitation are -20 to 30% in East Bay and Peninsula and -15% to 25% in Upcountry.

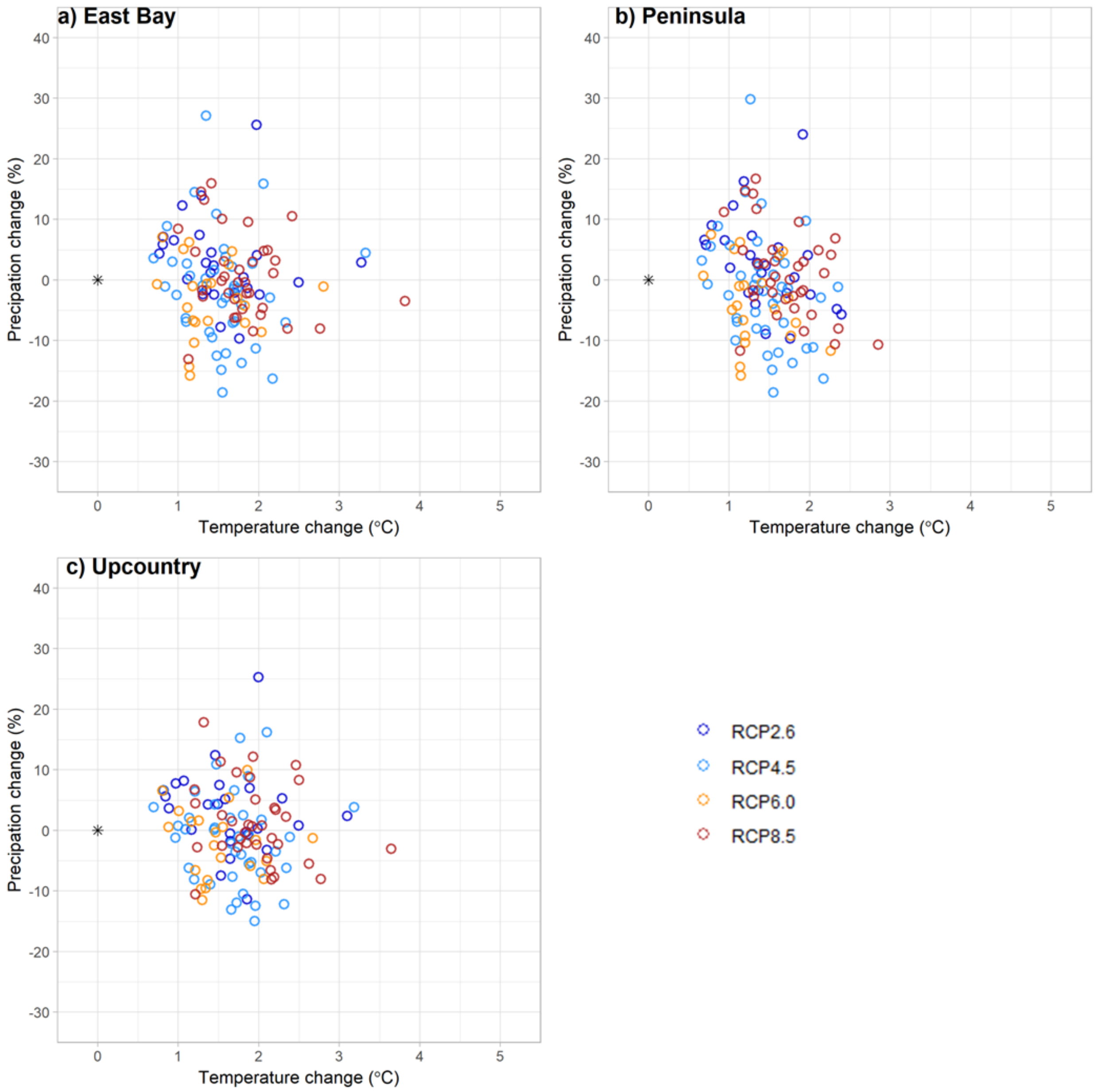

Figure 52 –Projected changes in mean annual precipitation and temperature from the CMIP5 climate models under Representative Concentration Pathways (RCPs) 2.6, 4.5, 6.0, and 8.5: a) East Bay, b) Peninsula, c) Upcountry. Each dot shows a calculated relative change in mean annual climate between the future period of 2020-2070 and the historical period of 1960-2010.

5.4. Development of Climate Scenarios

The final set of climate scenarios are obtained by perturbing the selected set of nine stochastic climate realizations by a range of temperature and precipitation change factors. The purpose of this process is to obtain a wide range of scenarios that span the uncertainties from natural climate variability as well from long-term anthropogenic climate change.

Based on the analysis shown in Section 5.3, we vary the annual mean temperature from 0 to 5° C with 1° C increments. For precipitation, we explored a range of changes from -40% to 40% with 5% increments. Overall, this results in a vector of 102 climate changes from each unique combination of 6 temperature changes and 17 precipitation changes. These change factors are then applied over each of the nine stochastic realizations of 50-year length transiently, resulting in a total of 918 climate scenarios (Table 9).

Table 9. Summary of climate change scenarios

Type of uncertainty	**Sampling range**	**Sample size**
Natural climate Variability	stochastic realizations of the historical climate	9 realizations
Changes in mean annual precipitation (%)	-40 % to 40 % with 5% increments	17 change factors
Changes in mean annual temperature (°C)	0 to 5° C with 1° C increments	6 change factors
	TOTAL	*918 climate scenarios*

The final set of annual precipitation series that result from the combinations of nine stochastic realizations and five levels of precipitation changes (i.e., linear changes of -40%, -20%, 0, 20% and 20% from the baseline values) is displayed from Figure 53 to Figure 55. These time-series illustrate a wide range of challenging scenarios for the SFPUC water resources system with in terms of both wet and dry conditions as they consider natural climate variability and possible climate changes together.

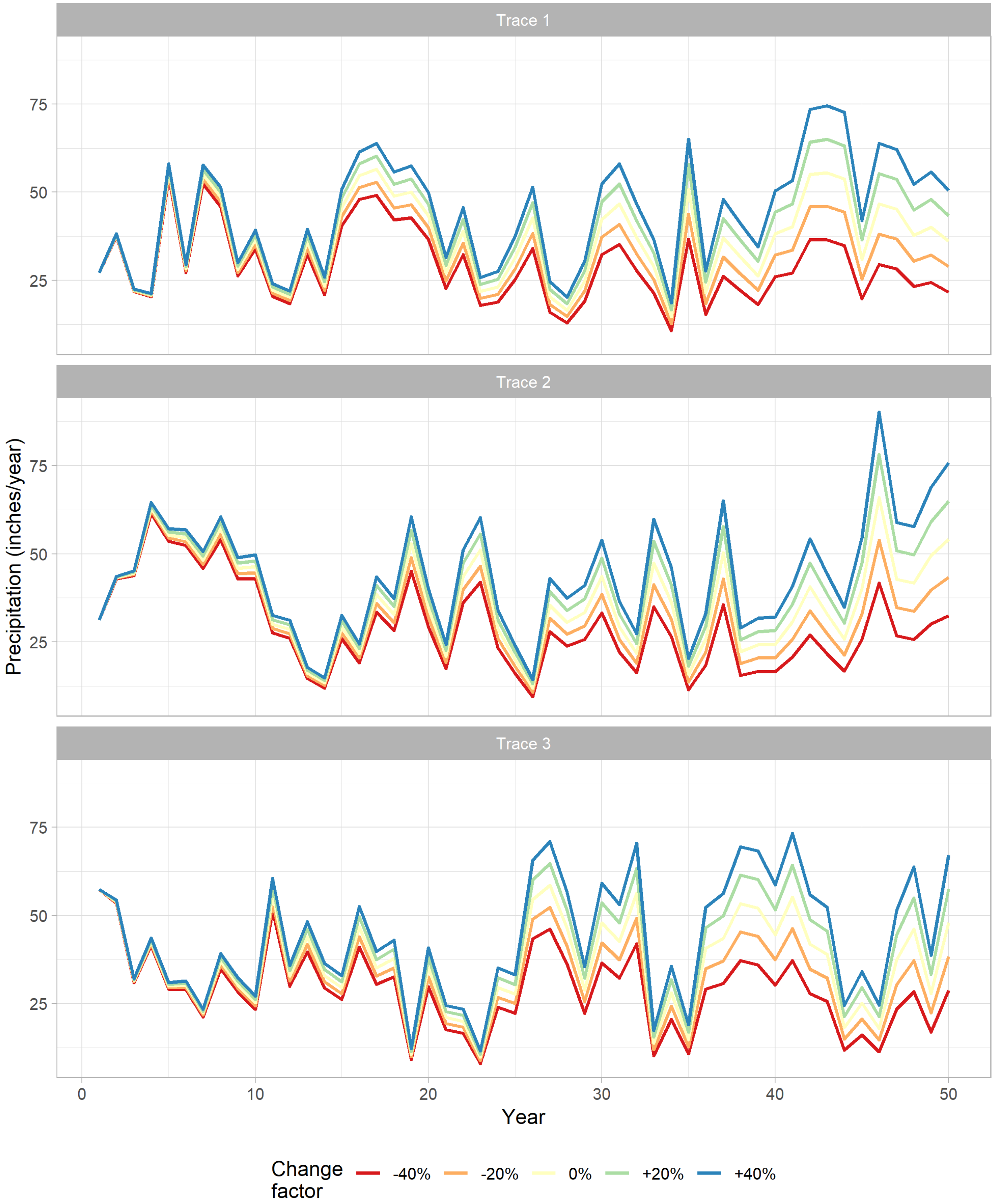

Figure 53. Selected set of representative stochastic realizations from the weather generator outputs (Traces 1, 2, and 3 respectively). Each stochastic trace is linearly perturbed by five precipitation change factors (i.e., -40%, -20%, 0, and 40%) to impose long-term climate changes.

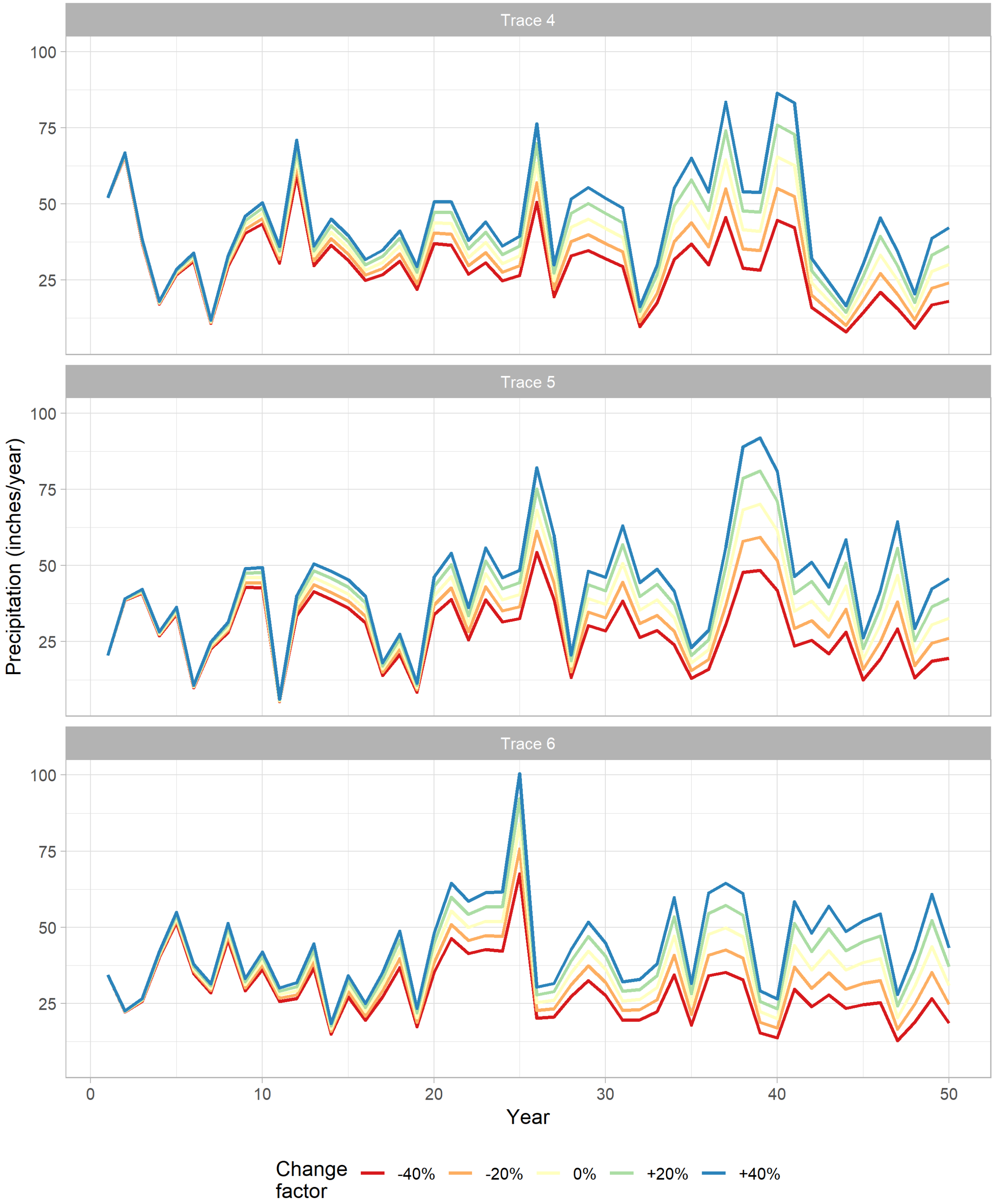

Figure 54. Selected set of wet stochastic realizations from the weather generator outputs (Traces 4, 5, and 6 respectively). Each stochastic trace is linearly perturbed by five precipitation change factors (i.e., -40%, -20%, 0, and 40%) to impose long-term climate changes.

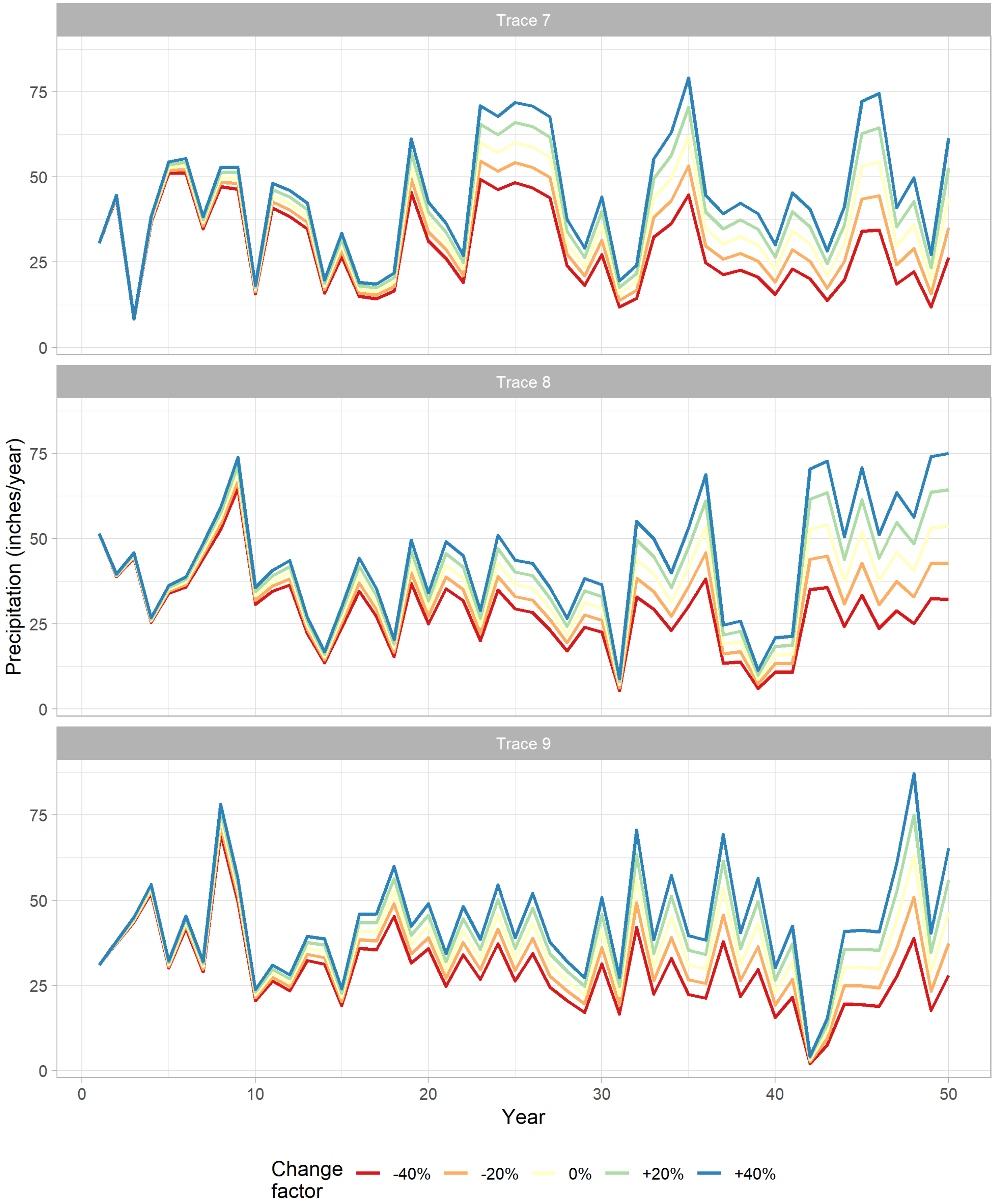

Figure 55. Selected set of dry stochastic realizations from the weather generator outputs (Traces 7, 8, and 9 respectively). Each stochastic trace is linearly perturbed by five precipitation change factors (i.e., -40%, -20%, 0, and 40%) to impose long-term climate changes.

5.5. GCM Downscaling

GCM projections are too coarse and biased to be used directly for a hydrologic impact assessment and need to be downscaled to a finer resolution before they can be used to drive hydrologic models [*Fowler et al.*, 2007]. There are two components to downscaling: spatial downscaling and bias correction. Bias correction refers to an approach where known systematic errors ('biases') in GCM projections over a region are removed. There are two primary methods for spatial downscaling: dynamical and statistical. Dynamical downscaling approaches make use of regional climate models (tailored to the region of interest) and use GCM output as boundary conditions. While it can provide a much more realistic representation of the physical processes in a region, dynamical downscaling can be computationally prohibitive, especially for larger domains and for processing several GCM ensembles with over centuries-long climate time series.

Statistical downscaling makes use of historically observed empirical relationships between finer-scale climate variables and coarser GCM output. Implicit in this approach is the assumption that the relationship between coarser scale climate and finer scale climate variables remains stationary. Constructed analogs (CA) has emerged as a popular statistical downscaling method, especially for North America [*Brekke et al.*, 2013]. CA methods search for a set of observed days (typically 30) that most closely match a given GCM output day when the observations are coarsened to the GCM grid. Bias-corrected constructed analog (BCCA) and Localized Constructed Analog (LOCA) [*Pierce et al.*, 2015] are two commonly used sets of downscaled GCM data products that make use of the CA method [*Bracken*, 2016].

There are three key differences between the LOCA and BCCA approaches. BCCA selects a set of 30 analog days where climate most closely matches a given GCM grid cell daily climate across the entire downscaling domain. LOCA selects the set of 30 analog days based on how well the observed days match the GCM climate over ~1000 km region around the point being spatially downscaled. The second key difference is that while the BCCA approach calculates optimal weights for the selected 30 days to generate downscaled climate, LOCA selects only one of the 30 days that is most similar to the point being downscaled at a ~100 km scale. This has important implications as the LOCA approach thus avoids the problem of spurious precipitation drizzle generation and damping of precipitation extremes that result from using a weighted average of 30 days (as is done for BCCA). The third key difference between the LOCA and BCCA data products is in the bias correction method. BCCA uses quantile mapping for bias correction that can lead to a loss of the GCM predicted climate change signal depending on the climate variability of the given region. LOCA avoids this problem by making use of a three-step process that preserved the climate signal.

Given the internal climate variability observed in California's climate, and the spatial climate variability across our study area, the choice of GCM downscaling approach used to evaluate hydrologic impacts of climate change may influence findings. In this study, we compare BCCA and LOCA downscaled climate data and its projected effect on SFPUC watersheds. We also compare the downscaled GCM projections with climate simulation produced using a stochastic weather generator. We obtain downscaled GCM ensembles for both the BCCA and LOCA approaches [*Maurer et al.*, 2007]; retaining only the 10 models that have been identified by the Climate Change Technical Advisory Group (CCTAG) [*CA DWR*, 2015b] to simulate California climatology well. The models selected for this analysis are all from RCP 8.5 emission scenario. For BCCA, we were only able to obtain 7 of the 10 models for the RCP 8.5 emission scenario.

Figure 56 shows a comparison of changes in the magnitude, frequency and variability for simulated precipitation at the Hetch Hetchy gage using different downscaling approaches. 100 weather generator runs, each 50 years long, run under baseline conditions (no climate change) are shown. The ensemble of GCM projections of 2020-2070 included in the study for this region indicate an increase in both the mean and standard deviation of annual precipitation over the historic average (black circle). A slight decrease in coefficient of variation is also observed. The lag-1 autocorrelation (not shown) values exhibited by the projections are similar to the low value of observed autocorrelation (0.03) for precipitation at this gage station. No systematic difference can be observed in the precipitation projections from the BCCA and LOCA downscaling. The weather generator runs exhibit climate characteristics comparable to the observed record and present a range of plausible climates that can be run to evaluate the effect of internal climate variability on regional hydrology. The weather generator is used in this study to explore a much wider range of future climate than those offered by the GCMs.

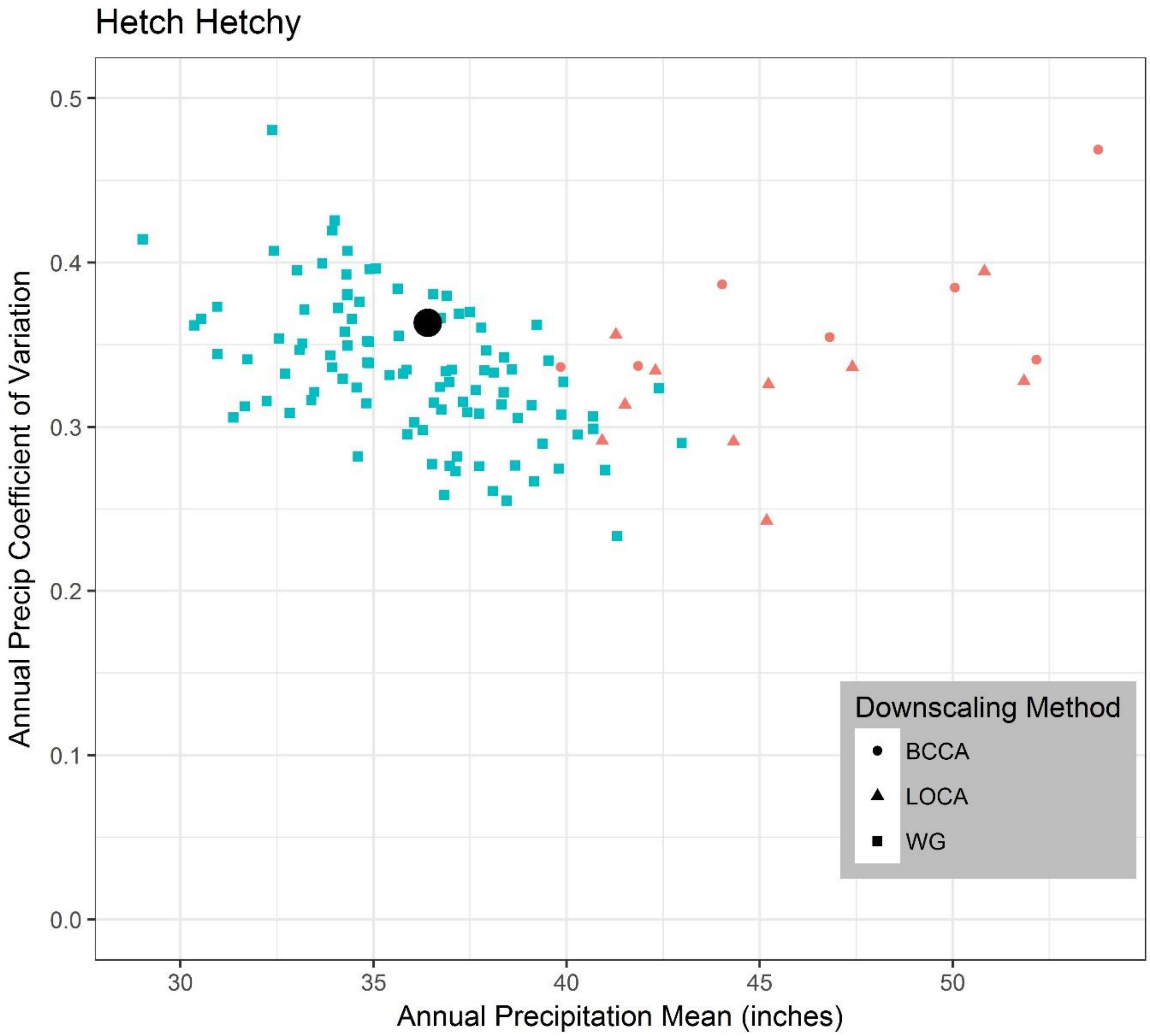

Figure 56. The mean and coefficient of variation of annual precipitation at the Hetch Hetchy precipitation gage. Statistics for observed (black), simulated (blue), and GCM projected (red) precipitation are shown. Shapes denote the different downscaling method used.

6. Climate realizations: CliWxGen vs. NCAR-WG

The section provides a summary of the task of comparing synthetic sequences of daily climate generated by NCAR-WG and CliWxGen. Although both NCAR and CliWxGen generators produced new sequences of daily precipitation and daily maximum and minimum temperature across the Upcountry region, the comparison described in this section focuses on the precipitation variable only. The comparison is carried out using simulated precipitation at nine stations spread over the Upcountry region. Precipitation time series at these nine locations are required inputs to PRMS, the hydrology model used for the LTVA to simulate streamflow across the region (see the Technical Report 2: Hydrology Modeling Module; HGR TR2, 2021). The nine considered precipitation stations are Hetch Hetchy Reservoir, Buck Meadows, Tuolumn Meadows, Cherry Valley Dam, Moccasin, Pinecrest, Yosemite, Gianlelli and Early Intake). Prior to comparing the NCAR and CliWxGen weather generator outputs, it is worth highlighting few differences between these two tools.

As described in more details in the previous sections, CliWxGen is a stochastic weather generator that combines a wavelet autoregressive model with the method of fragment and the k-nearest neighbors (Knn) approach. As such, CliWxGen is only driven by the low frequency components that are identified from the historical observed rainfall. In this study, only one significant low frequency component was identified (≈15-year frequency, Section 2.4). CliWxGen simulated daily precipitation time series for only five out of the nine stations that are used in PRMS model. Precipitation time series at the four missing locations are obtained via interpolation fro m the five available stations; see the Technical Report 2 (HRD TR2, 2021) for more details regarding the interpolation). Nine 50-year long stochastic realizations of daily precipitation are used for the comparison. As a whole, these nine stochastic realizations built by CliWxGen are deemed consistent with the historical period used, which is the period 1956-2011.

The NCAR weather generator is a non-parametric stochastic weather generator that combines a Markov Chain Model (MCM) with the Knn approach. MCM is used to create daily stochastic sequences of dry, wet and very wet days over arbitrary long sequences (in this case, 30-year long periods). Knn is used to randomly select a date from the historic record that satisfies the sequence state (dry-to-dry, dry-to-wet, dry-to-very wey, etc) that has been simulated with MCM. To account for seasonal effects, candidate days are sampled within a moving window that is centered on the current Julian day. For each selected dates, precipitation, maximum and minimum temperature are sampled at once to keep consistency among the weather variables. For future periods, i) a similar temperature trend as observed in the GCM projections is added to the synthetically generated temperature time series; ii) the magnitude of extremes is corrected to account for the change in extreme precipitation between historic and future periods, as seen in the GCM projections. Four different GCMs are used to condition the NCAR weather generator (CCSM, CESM, GFDL, MPI). Up to 30 stochastic realizations were generated for each GCM-forcing. The dataset used to build NCAR weather generator is the dataset that SPUC uses as input data to their PRMS models for Upcountry. This dataset spans from 1969 to 2015. More details regarding the NCAR weather generator are given in the Technical Report: Climate Change Storylines (NCAR, 2018).

Figure 57 shows the results of the comparison of the simulated annual precipitation obtained from the NCAR weather generator (boxplot) and CliWxGen (colored symbols). Although the comparison is meant to be carried out under current climate conditions, simulated future periods are shown for NCAR-WG. As compared to the historical mean of the Upcountry annual precipitation (i.e., roughly 950 mm; 37.4 in), all nine CliWxGen realizations well reproduced the historical average. The historic realization (brown square symbol) is from five available gauges for which available rainfall data covers the period used by CliWxGen (i.e., 1956-2011) plus precipitation at the missing four gauges were obtained via interpolation (HGR TR2, 2021). The black square shows the annual average from historic observed ground stations that are used in PRMS. Each NCAR-WG produces a range of mean statistics that varies from 1981-2010 through 2041-2070. It is observed CCSM, CESM, and GFDL-informed realizations' mean decreases from 1981-2010 to 2011-2040 before increasing for 2041-2070. Historical (1981-2010) CCSM, CESM, GFDL, and MPI-informed realizations centered closely on the historical mean (based on the median) and captures the range of the nine stochastic climate realizations. However, CESM tends to produce lower annual total precipitation than the historical (one realization of CESM goes as low as about 800 mm).

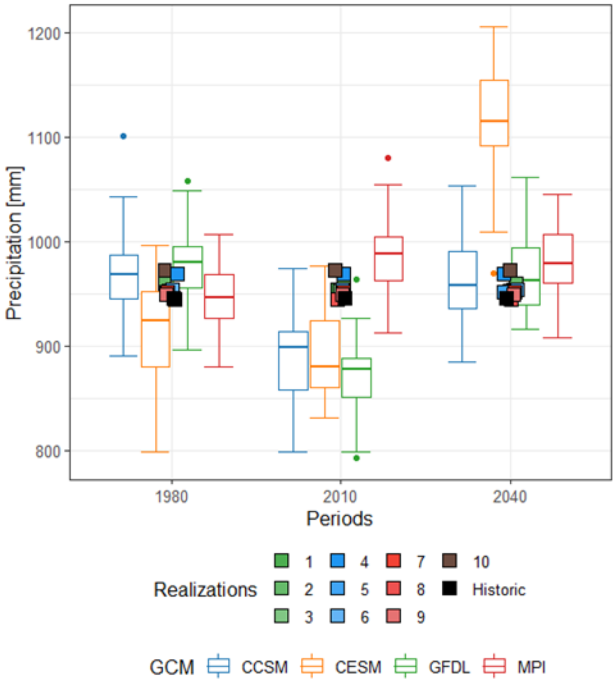

Figure 57. Comparison of the simulated annual average precipitation across the Upcountry region (average of 9 stations). Results from the NCAR-WG are shown using boxplots. Each color shows a different GCM used to conditions the NCAR-WG. Each boxplot summarizes the distribution across the 30 stochastic realizations. Results are shown for the baseline period (1981-2010, labeled '1980') and two futures periods (2011-2040 and 2041-2070, respectively labeled '2010' and '2040'). Results obtained from each stochastic realization (9 total) simulated via CliWxGen are shown with colored square symbols. CliWxGen realizations are meant to represent the 1956-2011 period (to ease the reading, results are repeated for each period). Note that a random noise was added to the x-axis of the square to ease reading of the figure. The historical realization is shown in brown color and the black squares show the annual average calculated using PRMS inputs (1970-2016). In the context of this comparison, the latter is considered being the 'truth', although the time periods used by each model vary.

Figure 58 illustrates the comparison results between NCAR-WG and CliWxGen in regards with variability of the precipitation variable. Variability at both annual and monthly scales is analyzed. Results show that simulations from NCAR-WG tend to overestimate the variability of the annual precipitation. It is noted for instance that the variability of the historical annual precipitation (black squares in Figure 58, left) is below the lower inter-quartile of the annual precipitation distribution across the ensemble of 30 realizations for each forcing GCM. The nine stochastic realizations from CliWxGen are closer to the historical value. Some slightly overestimate while some slightly underestimate the inter-annual variability of the historical precipitation. As an ensemble, the nine stochastic realizations represent correctly the inter-annual variability of the annual historical precipitation across the Upcountry region.

The results of the comparison for the monthly temporal scale is significantly different than the one discussed for the annual scale. It is noted that simulations from NCAR-WG significantly overestimate the variability of the monthly precipitation across the region. On the other hand, the stochastic realizations from CliWxGen underestimate the precipitation variability at monthly scale. Note that the historical realization (brown) is close to the historic precipitation. A similar results is obtained on a daily temporal scale, although not shown in this report. More details regarding the comparison are given in the Technical Report 2 (HRG TR2, 2021).

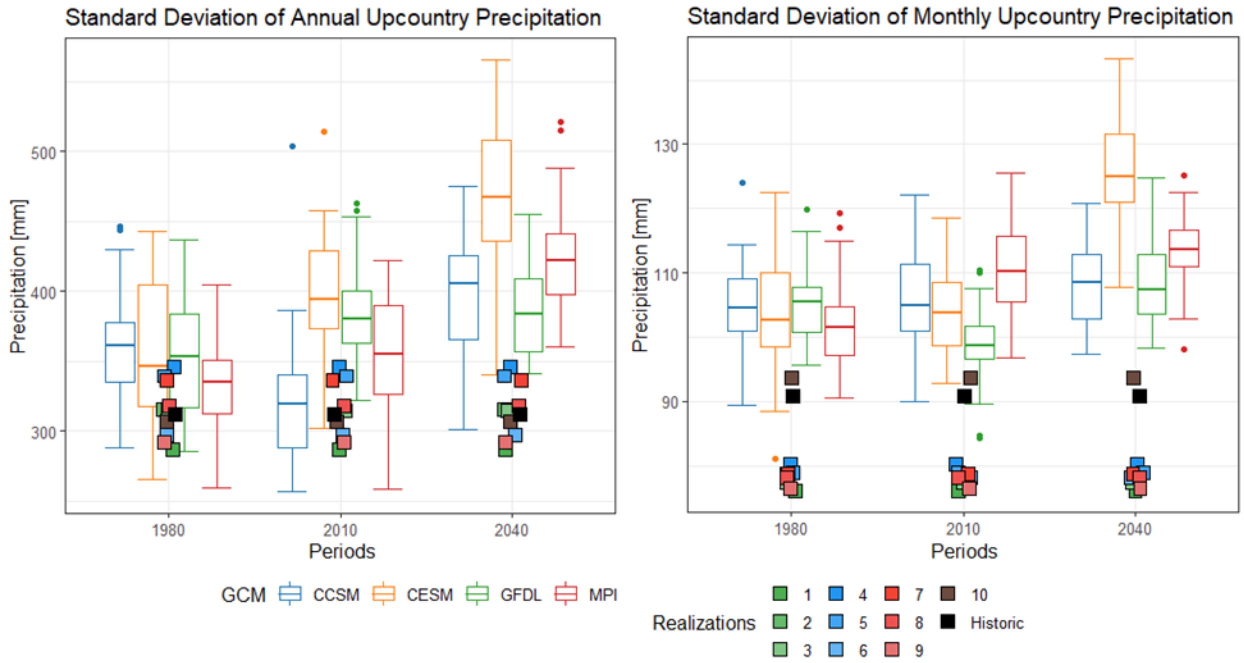

Figure 58. Comparison of the standard deviation of the simulated precipitation across the Upcountry region (average of 9 stations). Left: annual temporal scale. Right: monthly temporal scale. See

Figure **57** for more caption details.

7. References

Barnett TP, Pierce DW, Hidalgo HG, et al (2008) Human-Induced Changes United States. Science (80-) 319:1080–1084.

Brown C, Ghile Y, Laverty M, Li K (2012) Decision scaling: Linking bottom-up vulnerability analysis with climate projections in the water sector. Water Resour Res 48:1–12. doi: 10.1029/2011WR011212

CA DWR (2015) California Climate Science and Data - For Water Resources Managemnt. Sacramento, CA

Deser C, Phillips A, Bourdette V, Teng H (2012) Uncertainty in climate change projections: The role of internal variability. Clim Dyn 38:527–546. doi: 10.1007/s00382-010-0977-x

Dettinger M, Cayan D (2014) Drought and the California Delta—A Matter of Extremes. San Fr Estuary Watershed Sci. doi: 10.15447/sfews.2014v12iss2art4

Dettinger MD, Cayan DR, Diaz H, Meko DM (1998) North–South Precipitation Patterns in Western North America on Interannual-to-Decadal Timescales. J Clim 11:3095–3111. doi: https://doi.org/10.1175/1520-0442(1998)011<3095:NSPPIW>2.0.CO;2

Hyndman RJ, Khandakar Y (2008) Automatic time series forecasting: The forecast package for R. J Stat Softw 27:C3–C3. doi: 10.18637/jss.v027.i03

Killam D, Bui A, LaDochy S, et al (2014) California Getting Wetter to the North, Drier to the South: Natural Variability or Climate Change? Climate 2:168–180. doi: 10.3390/cli2030168

Kwon H-HH, Lall U, Khalil AFF (2007) Stochastic simulation model for nonstationary time series using an autoregressive wavelet decomposition: Applications to rainfall and temperature. Water Resour Res 43:1–15. doi: 10.1029/2006WR005258

Lall U, Sharma A (1996a) A nearest neighbor bootstrap for resampling hydrologic time series. Water Resour Res 32:679–693.

Lall U, Sharma A (1996b) A nearest neighbor bootstrap for resampling hydrologictime series. Water Resour Res 32:679–693. doi: 10.1029/95WR02966

Loucks DP, Van Beek E, Stedinger JR, et al (2005) Water resources systems planning and management: an introduction to methods, models and applications. UNESCO, Paris

Maurer EP, Wood AW, Adam JC, et al (2002) A {Long}-{Term} {Hydrologically} {Based} {Dataset} of {Land} {Surface} {Fluxes} and {States} for the {Conterminous} {United} {States}*. J Clim 15:3237–3251. doi: 10.1175/1520-0442(2002)015<3237:ALTHBD>2.0.CO;2

Meko DM, Woodhouse CA, Touchan R (2014) Klamath/San Joaquin/Sacramento Hydroclimatic Reconstructions from Tree Rings.

Sicke WS, Lund JR, Medellín-Azuara J, Madani K (2013) Climate change adaptations for California's San Francisco Bay Area water supplies. Br J Environ Clim Chang 3:292–315. doi: 10.9734/BJECC/2013/2708

Silva AT, Portela MM (2012) Disaggregation modelling of monthly streamflows using a new approach of the method of fragments. Hydrol Sci J 57:942–955. doi: 10.1080/02626667.2012.686695

Srikanthan R, McMahon TA (2001) Stochastic generation of annual, monthly and daily climate data: A review. Hydrol Earth Syst Sci 5:653–670. doi: 10.5194/hess-5-653-2001

Steinschneider S, Brown C (2013) A semiparametric multivariate, multisite weather generator with low-frequency variability for use in climate risk assessments. Water Resour Res 49:7205–7220. doi: 10.1002/wrcr.20528

Taylor KE, Stouffer RJ, Meehl GA (2012) An overview of CMIP5 and the experiment design. Bull Am Meteorol Soc 93:485–498. doi: 10.1175/BAMS-D-11-00094.1

Thomas H, Burden R (1963) Operations research in water quality management.

Torrence C, Compo GP (1988) A Practical Guide to Wavelet Analysis.

Vicuna S, Maurer EP, Joyce B, et al (2007) the Sensitivity of California Water Resources To Climate Change Scenarios 1.

APPENDIX I – Historical Statistics of Weather Variables in the Study Region

Annual precipitation (inches)

Station name	**Region**	**Mean**	**Coefficient of Variation**	**Minimum**	**Maximum**
Alameda East Portal	East Bay	19.40	0.37	0.00	33.83
Buck Meadows	Upcountry	34.57	0.38	11.57	67.67
Calaveras	East Bay	20.06	0.34	0.00	46.56
Cherry Valley	Upcountry	46.49	0.36	0.25	94.70
Davis Tunnel	Peninsula	36.91	0.40	2.20	67.88
Half Moon Bay	Peninsula	24.26	0.38	2.43	53.57
Mt Hamilton	East Bay	23.86	0.38	6.56	46.44
Hetch Hetchy	Upcountry	35.70	0.31	12.60	75.62
Early Intake	Upcountry	33.24	0.32	9.14	67.73
Lower Crystal Springs	Peninsula	25.35	0.35	0.13	51.43
Livermore Airport	East Bay	14.08	0.35	4.56	32.37
Moccasin	Upcountry	27.95	0.32	8.50	52.19
Moffett Federal Airfield	South Bay	12.85	0.36	3.08	31.40
Newark	East Bay	13.73	0.63	3.36	76.04
North San Andreas	Peninsula	29.75	0.38	5.77	59.90
Pilarcitos	Peninsula	37.19	0.35	0.00	65.45
Rose Peak	East Bay	20.94	0.32	5.65	32.93
San Andreas Res	Peninsula	31.91	0.33	6.86	61.38
San Antonio R	East Bay	17.87	0.35	4.81	40.31
Sawyer Camp	Peninsula	33.04	0.41	6.60	64.80
San Francisco Int. Airport	Peninsula	19.23	0.36	3.38	38.34
San Jose	East Bay	11.68	0.32	2.71	17.15
Sonora	Upcountry	31.20	0.37	5.26	62.04
Sunol	East Bay	19.29	0.33	0.05	45.01
Tuolumne Meadows	Upcountry	25.05	0.35	7.51	53.88
Upper Crystal Springs	Peninsula	26.24	0.35	0.00	52.70
Yosemite	Upcountry	35.73	0.35	9.46	66.28

Annual temperature (°F)

Station name	Region	Mean	Coefficient of Variation	Minimum	Maximum
Buck Meadows	Upcountry	55.88	0.08	44.78	63.87
Burlingame	Peninsula	57.17	0.04	52.27	68.35
Cherry Valley	Upcountry	52.87	0.05	39.36	57.66
Half Moon Bay	Peninsula	54.79	0.02	52.21	57.78
Mt Hamilton	East Bay	54.53	0.04	43.46	58.45
Horse Meadows	Upcountry	36.12	0.12	23.18	40.06
Hetch Hetchy	Upcountry	53.71	0.04	41.41	59.11
Early Intake	Upcountry	57.37	0.04	46.58	63.56
Livermore Airport	East Bay	59.22	0.03	53.71	63.73
Moccasin	Upcountry	60.56	0.04	49.10	65.23
Moffett Federal Airfield	South Bay	59.30	0.03	54.15	64.00
Newark	East Bay	58.80	0.03	53.16	62.26
Paradise Meadow	Upcountry	36.78	0.11	26.03	43.72
San Francisco Int. Airport	Peninsula	57.36	0.03	54.19	62.28
San Jose	East Bay	60.29	0.03	54.60	62.38
Slide Canyon	Upcountry	35.44	0.13	21.29	39.66
Tuolumne Meadows	Upcountry	37.28	0.09	23.87	39.78

APPENDIX II – Historical Trends in Average Monthly Temperature

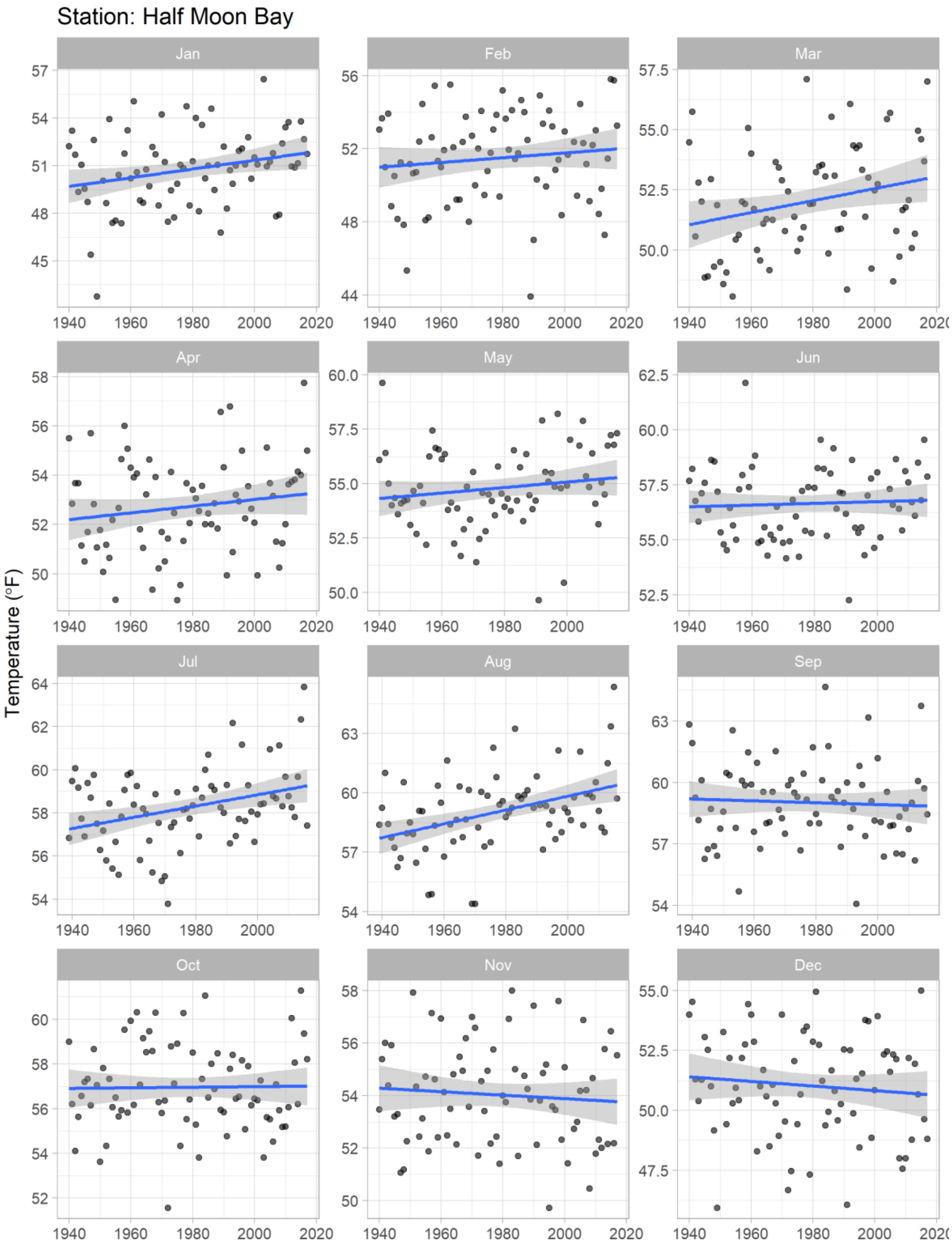

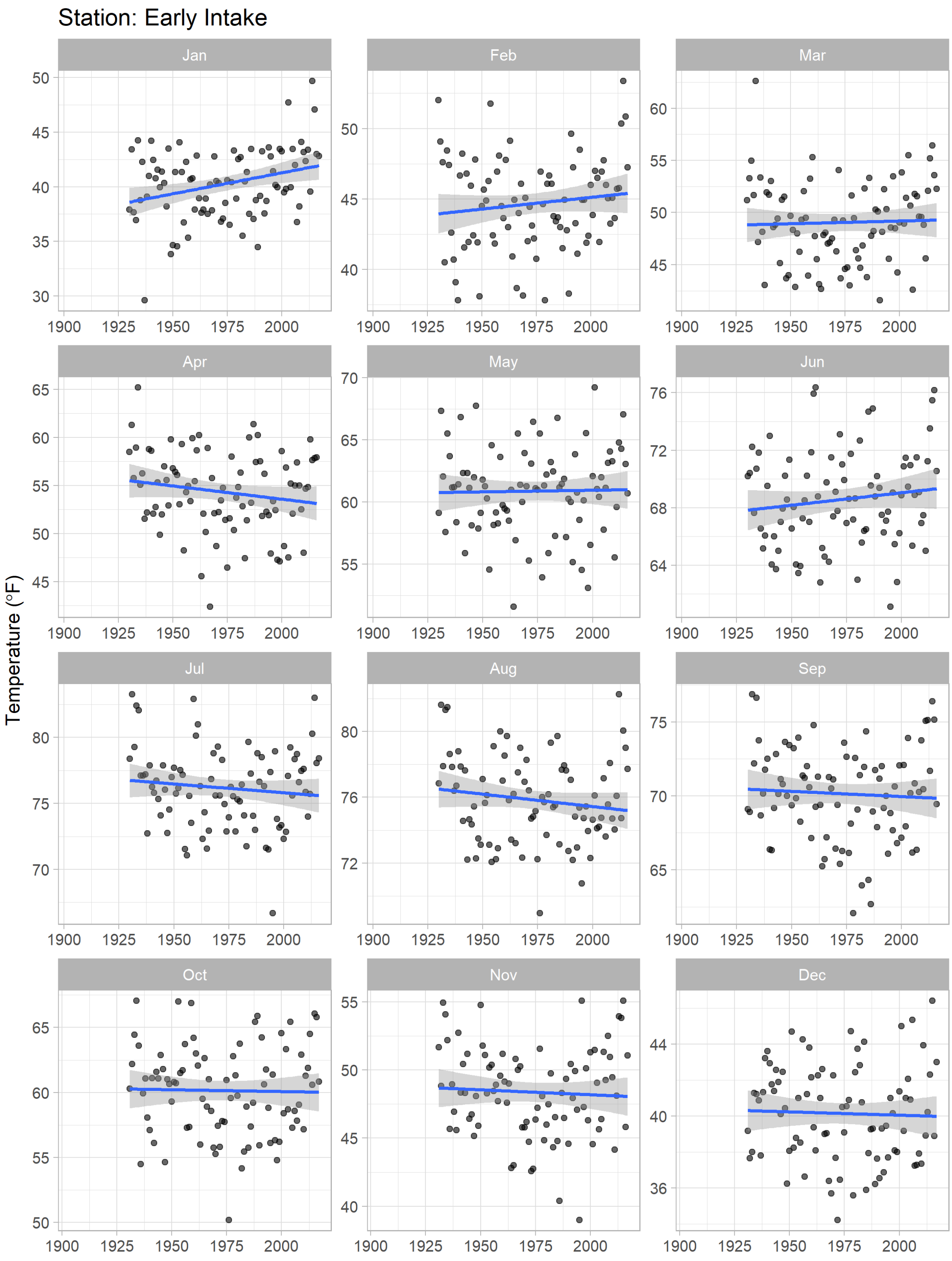
Station: Early Intake
Temperature (°F)
Jan
50
45
40
35
30
Feb
50
45
40
Mar
60
55
50
45
Apr
65
60
55
50
45
May
70
65
60
55
Jun
76
72
68
64
Jul
80
75
70
Aug
80
76
72
Sep
75
70
65
Oct
65
60
55
50
Nov
55
50
45
40
Dec
44
40
36
1900
1925
1950
1975
2000

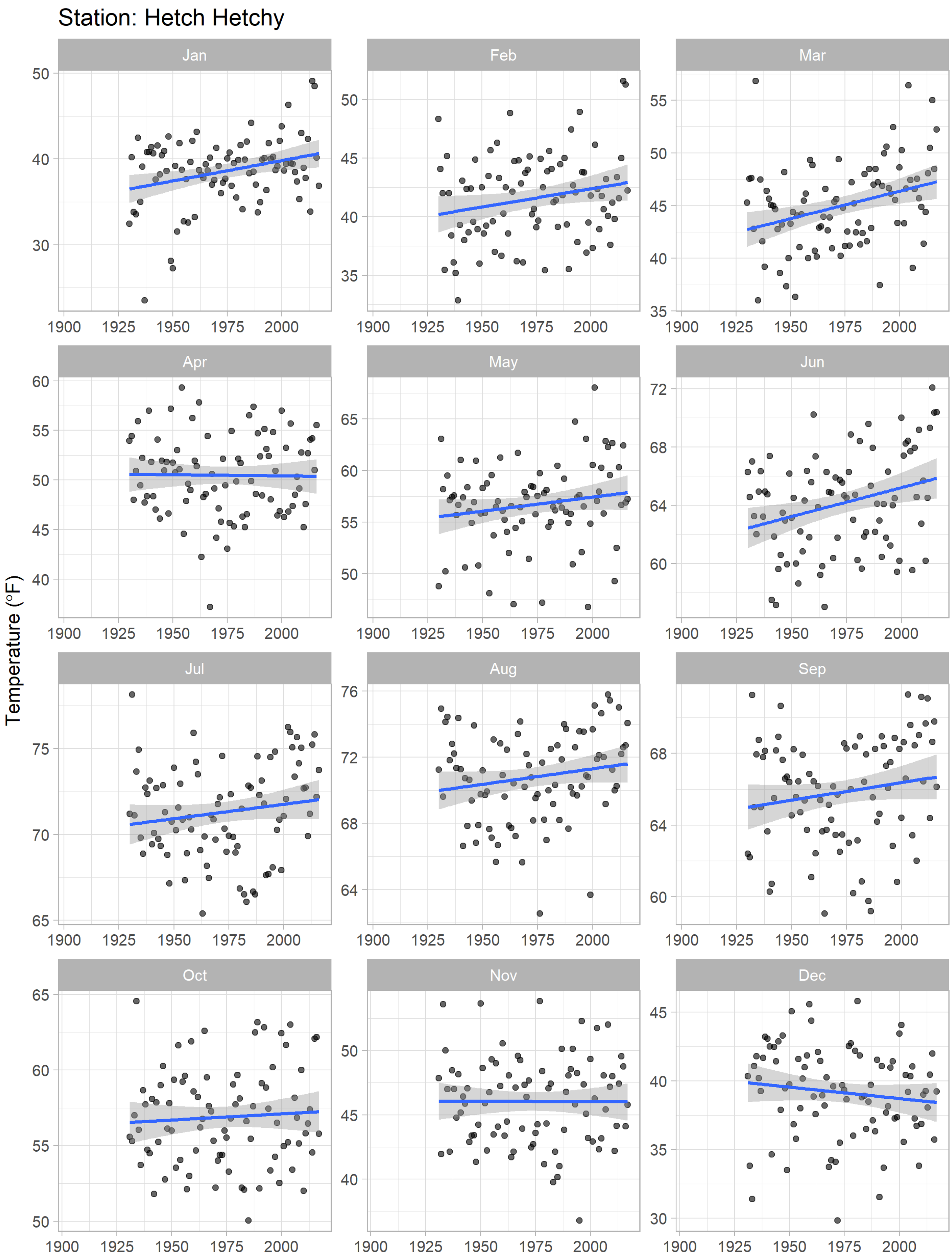
Station: Hetch Hetchy
Temperature (°F)
Jan
50
40
30
Feb
50
45
40
35
Mar
55
50
45
40
35
Apr
60
55
50
45
40
May
65
60
55
50
Jun
72
68
64
60
Jul
75
70
65
Aug
76
72
68
64
Sep
68
64
60
Oct
65
60
55
50
Nov
50
45
40
Dec
45
40
35
30
1900
1925
1950
1975
2000

Station: Mt Hamilton

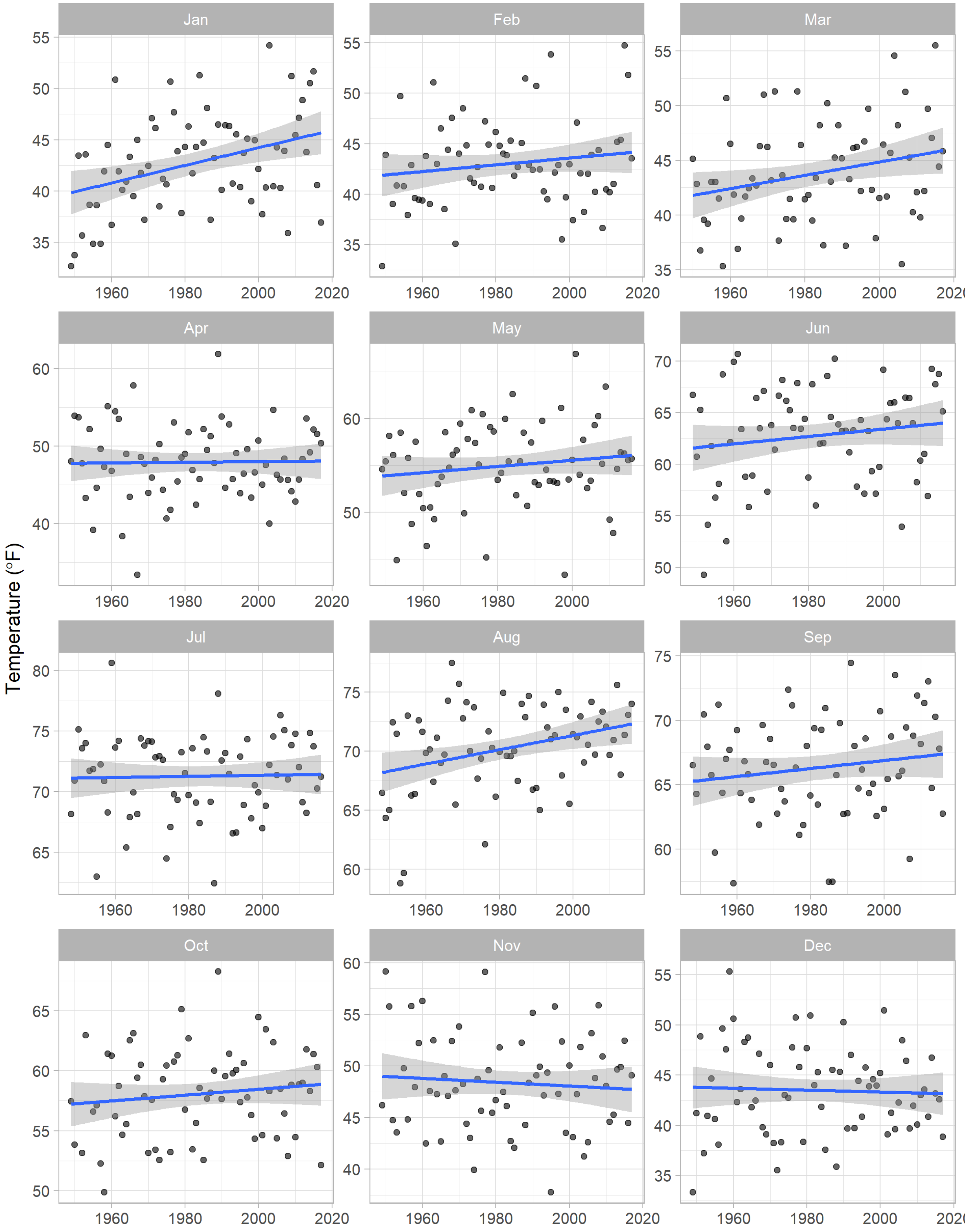

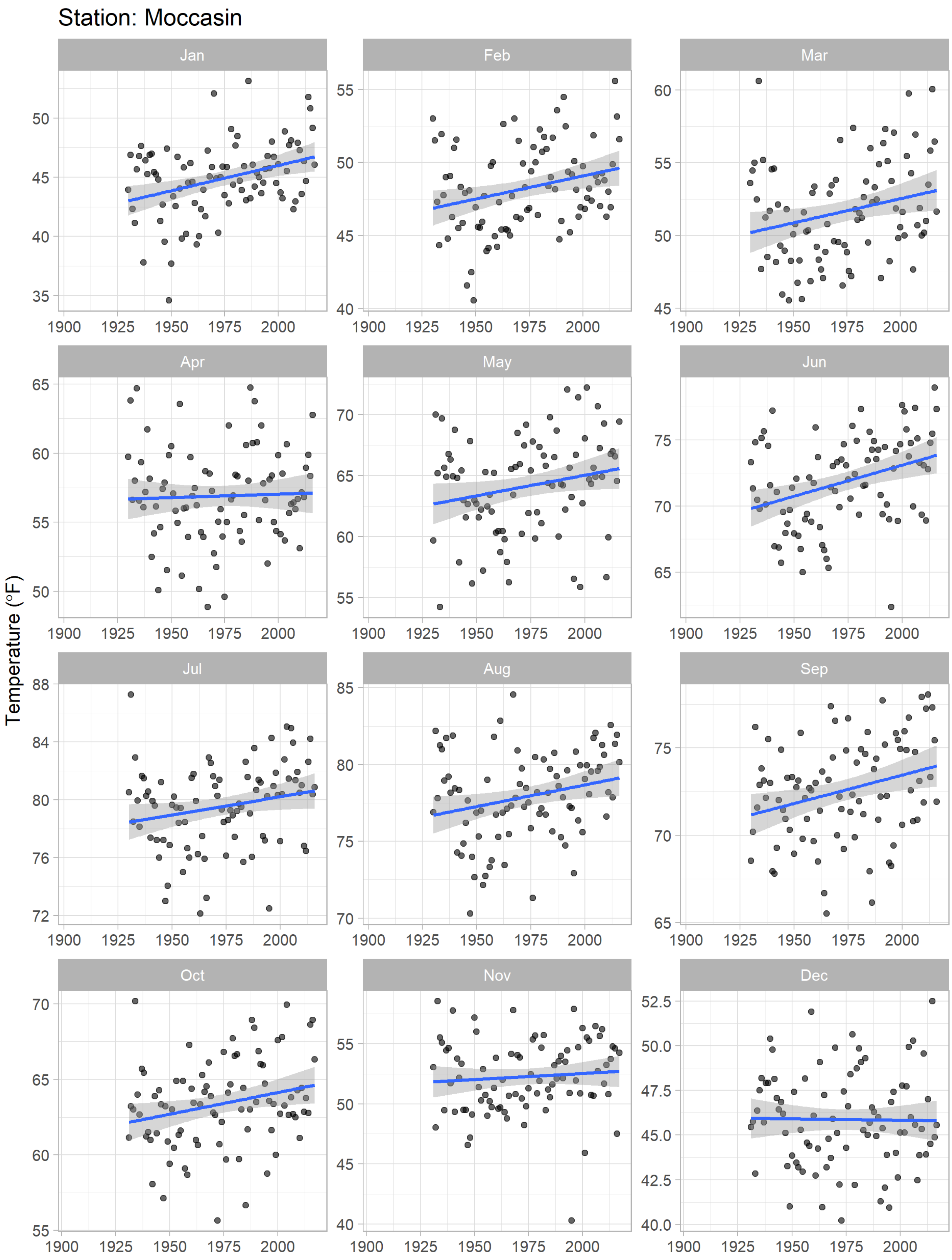
Station: Moccasin
Temperature (°F)
Jan
Feb
Mar
Apr
May
Jun
Jul
Aug
Sep
Oct
Nov
Dec
35
40
45
50
55
60
65
70
72
75
76
80
84
85
88
47.5
52.5
42.5
1900
1925
1950
1975
2000

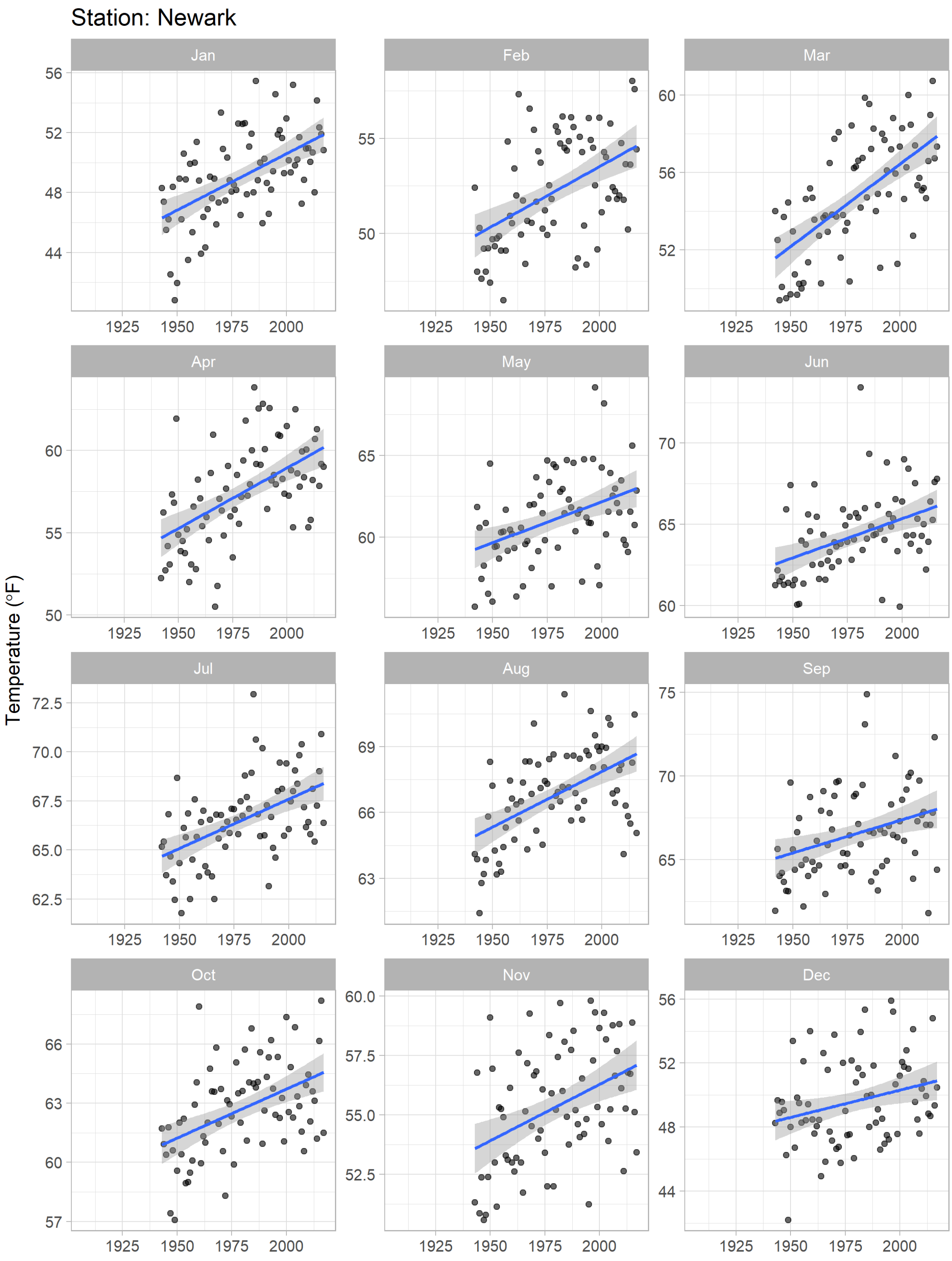
Station: Newark
Temperature (°F)
Jan
56
52
48
44
Feb
55
50
Mar
60
56
52
Apr
60
55
50
May
65
60
Jun
70
65
60
Jul
72.5
70.0
67.5
65.0
62.5
Aug
69
66
63
Sep
75
70
65
Oct
66
63
60
57
Nov
60.0
57.5
55.0
52.5
Dec
56
52
48
44
1925
1950
1975
2000

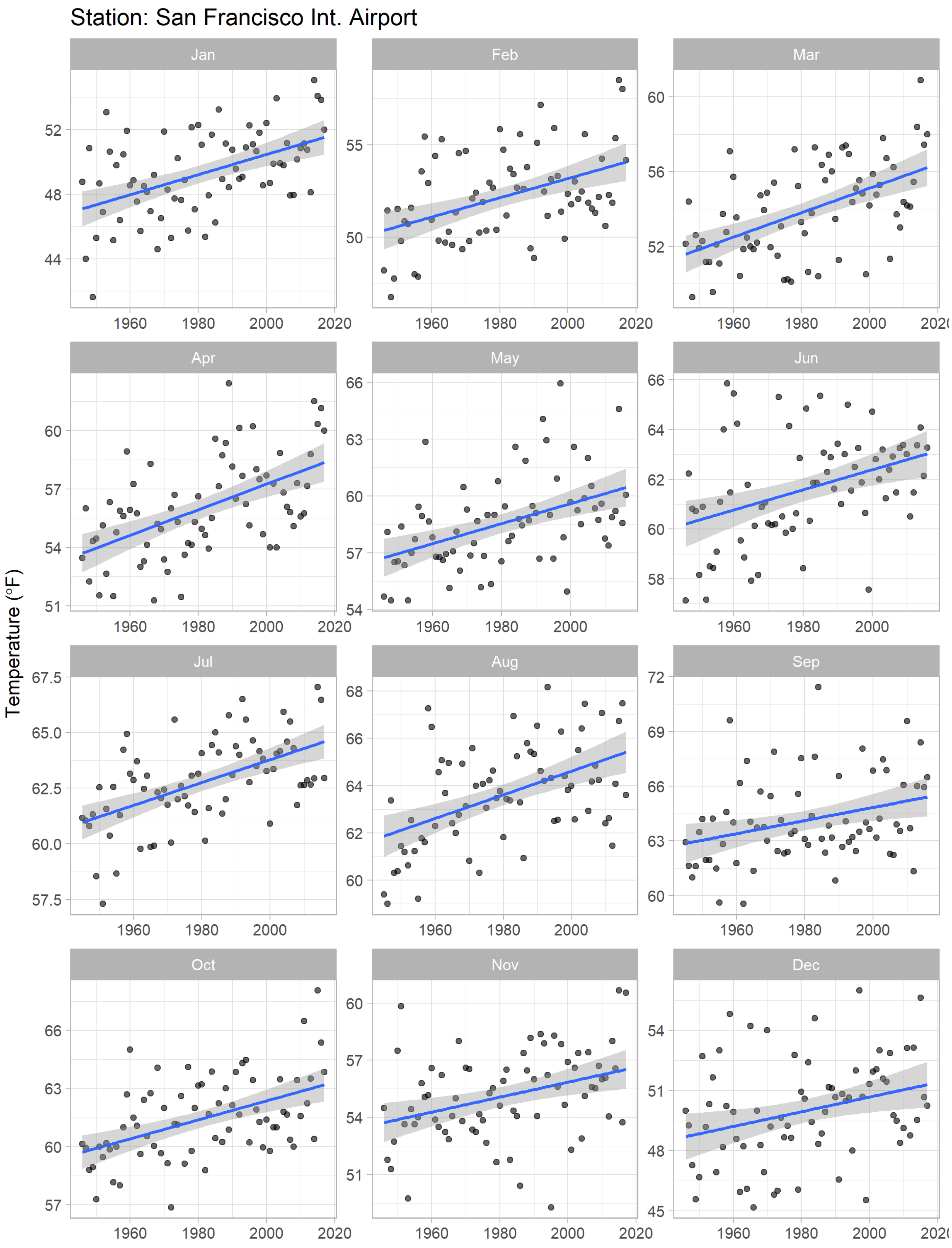
Station: San Francisco Int. Airport

APPENDIX III – Historical Trends in Monthly Precipitation (Selected Gages)

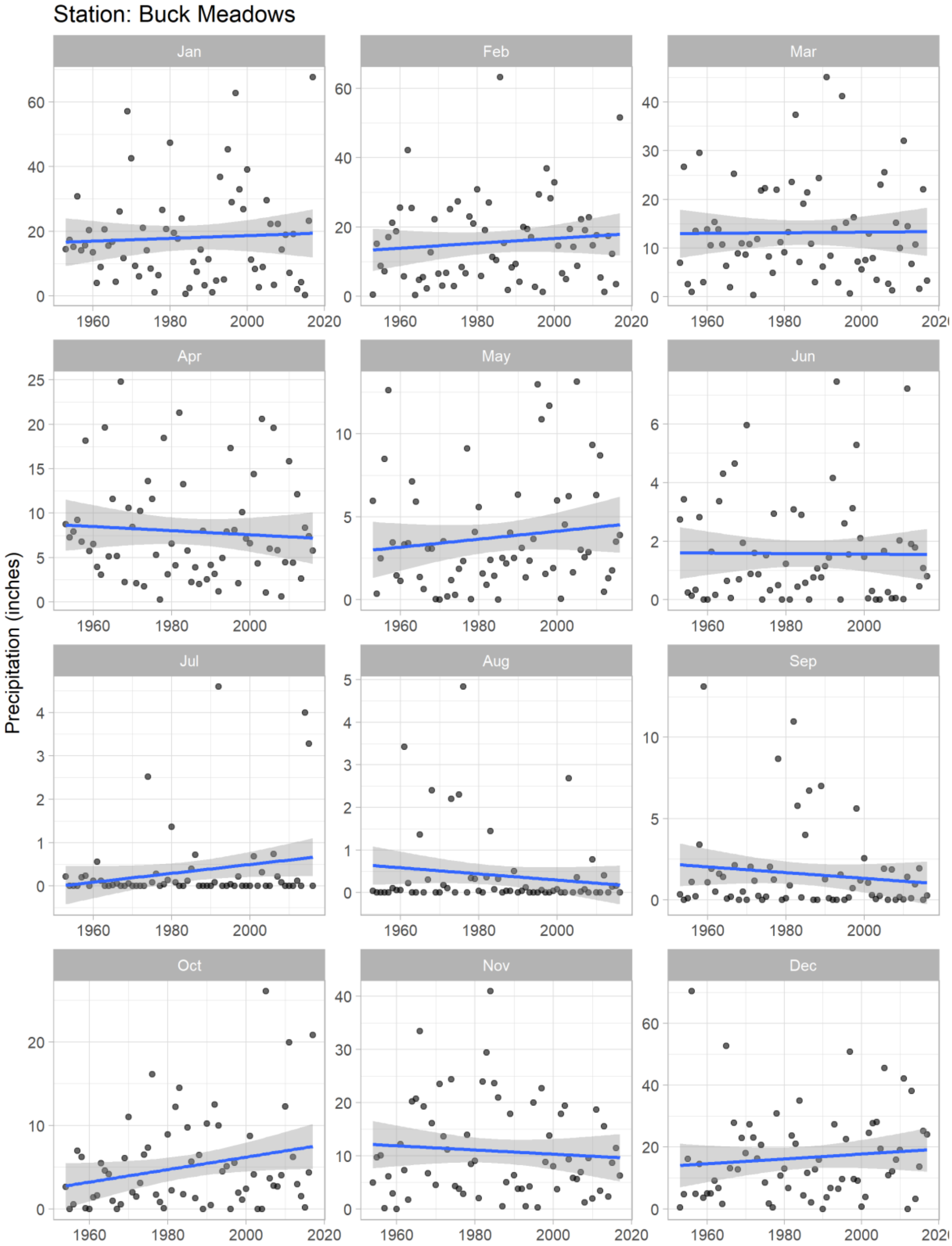

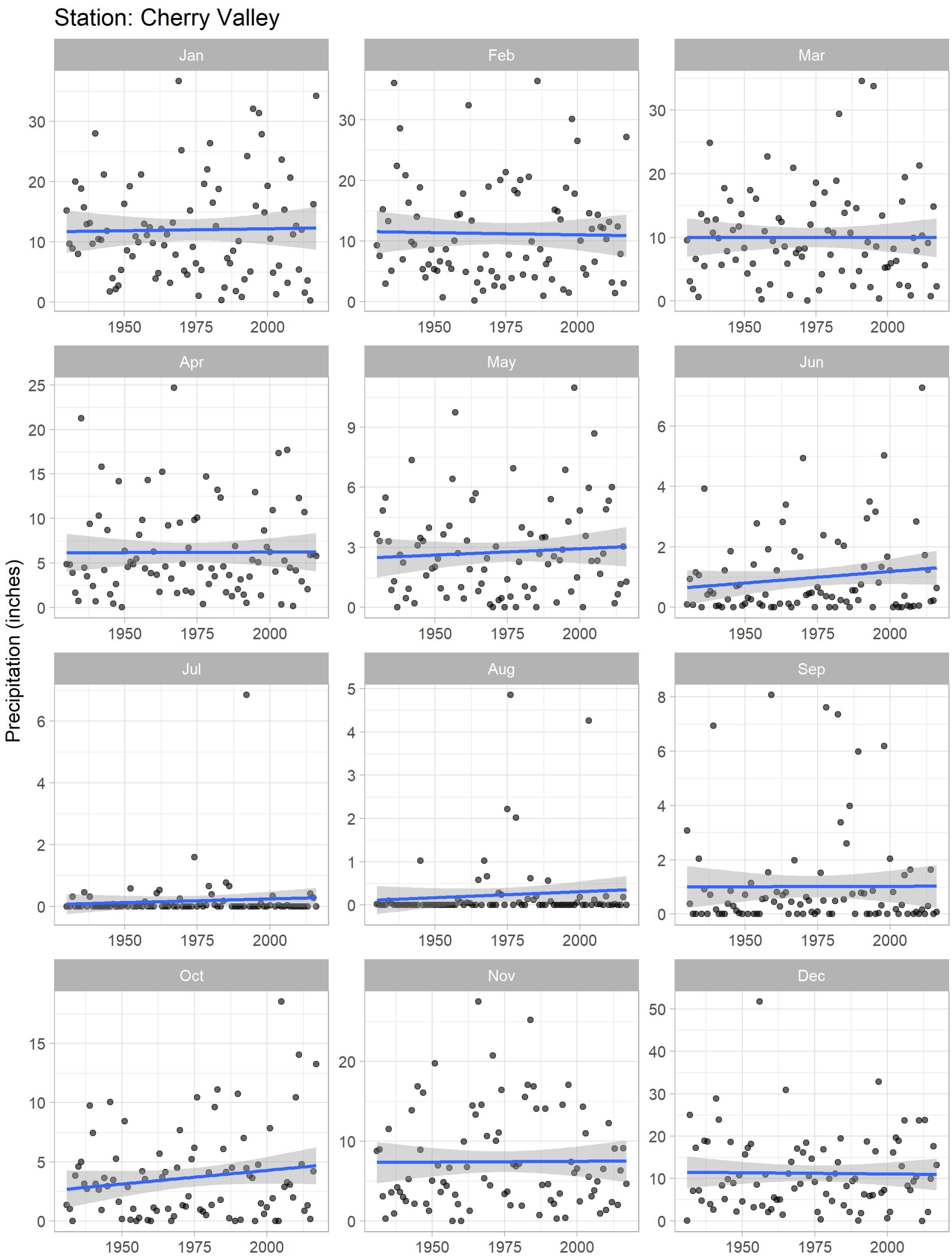
Station: Cherry Valley
Precipitation (inches)
Jan
Feb
Mar
Apr
May
Jun
Jul
Aug
Sep
Oct
Nov
Dec
0
10
20
30
0
5
10
15
20
25
0
3
6
9
0
2
4
6
0
1
2
3
4
5
8
40
50
1950
1975
2000

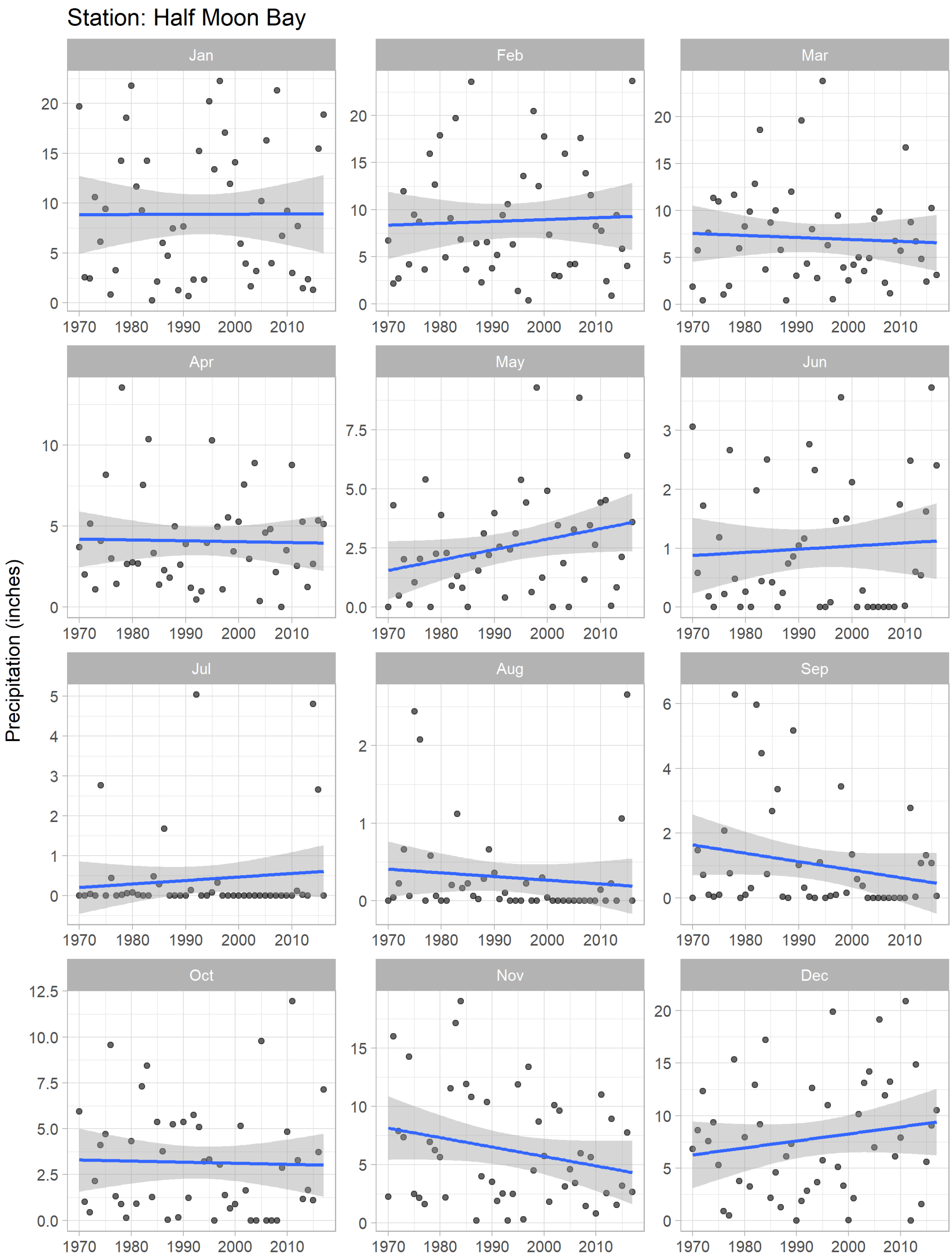

Station: Half Moon Bay
Jan
Feb
Mar
Apr
May
Jun
Jul
Aug
Sep
Oct
Nov
Dec
Precipitation (inches)
1970
1980
1990
2000
2010
0
5
10
15
20
0.0
2.5
5.0
7.5
10.0
12.5

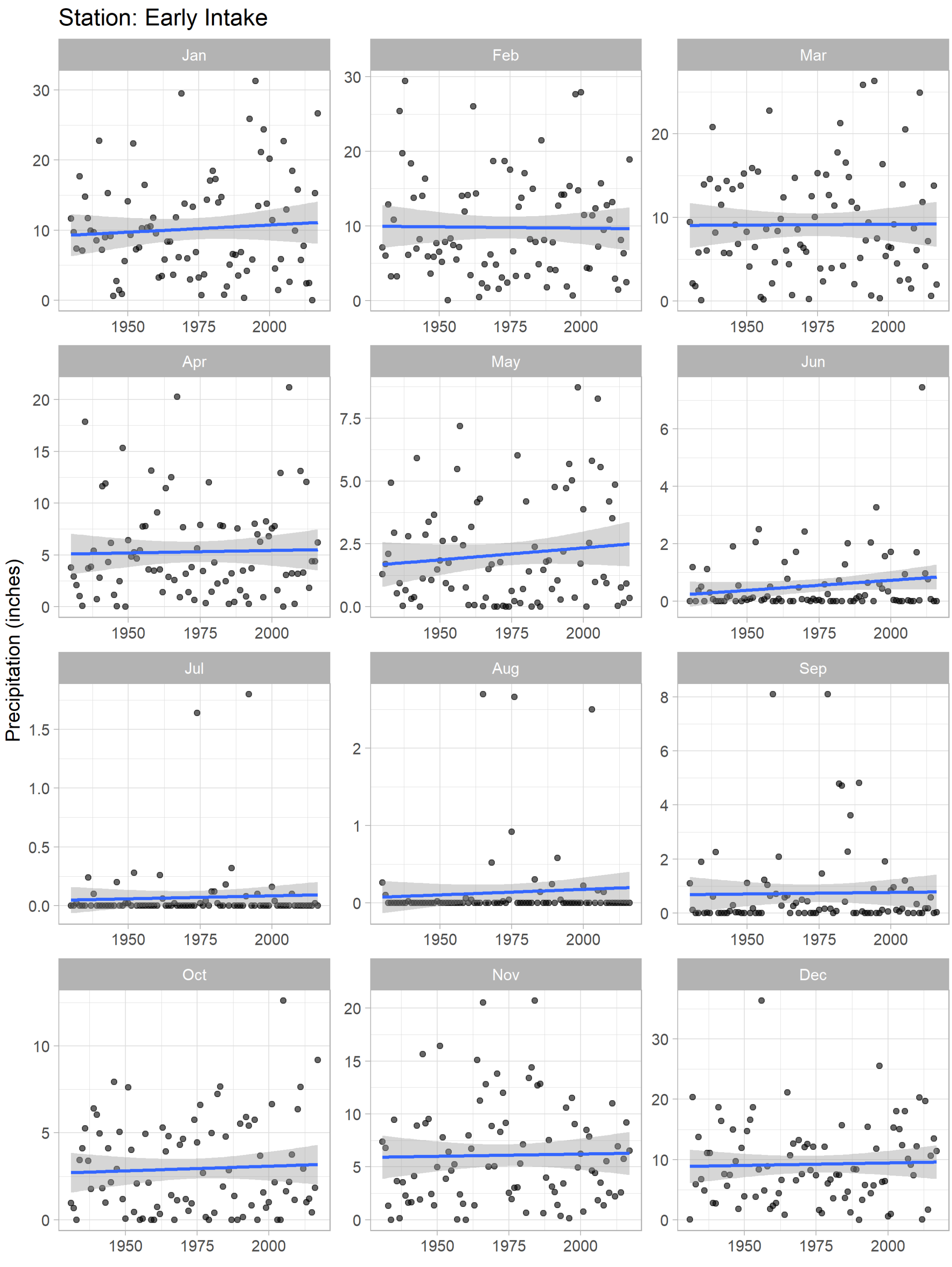
Station: Early Intake
Precipitation (inches)
Jan
Feb
Mar
Apr
May
Jun
Jul
Aug
Sep
Oct
Nov
Dec
0
10
20
30
0.0
2.5
5.0
7.5
0
2
4
6
8
0.5
1.0
1.5
0
1
2
0
5
10
15
20
1950
1975
2000

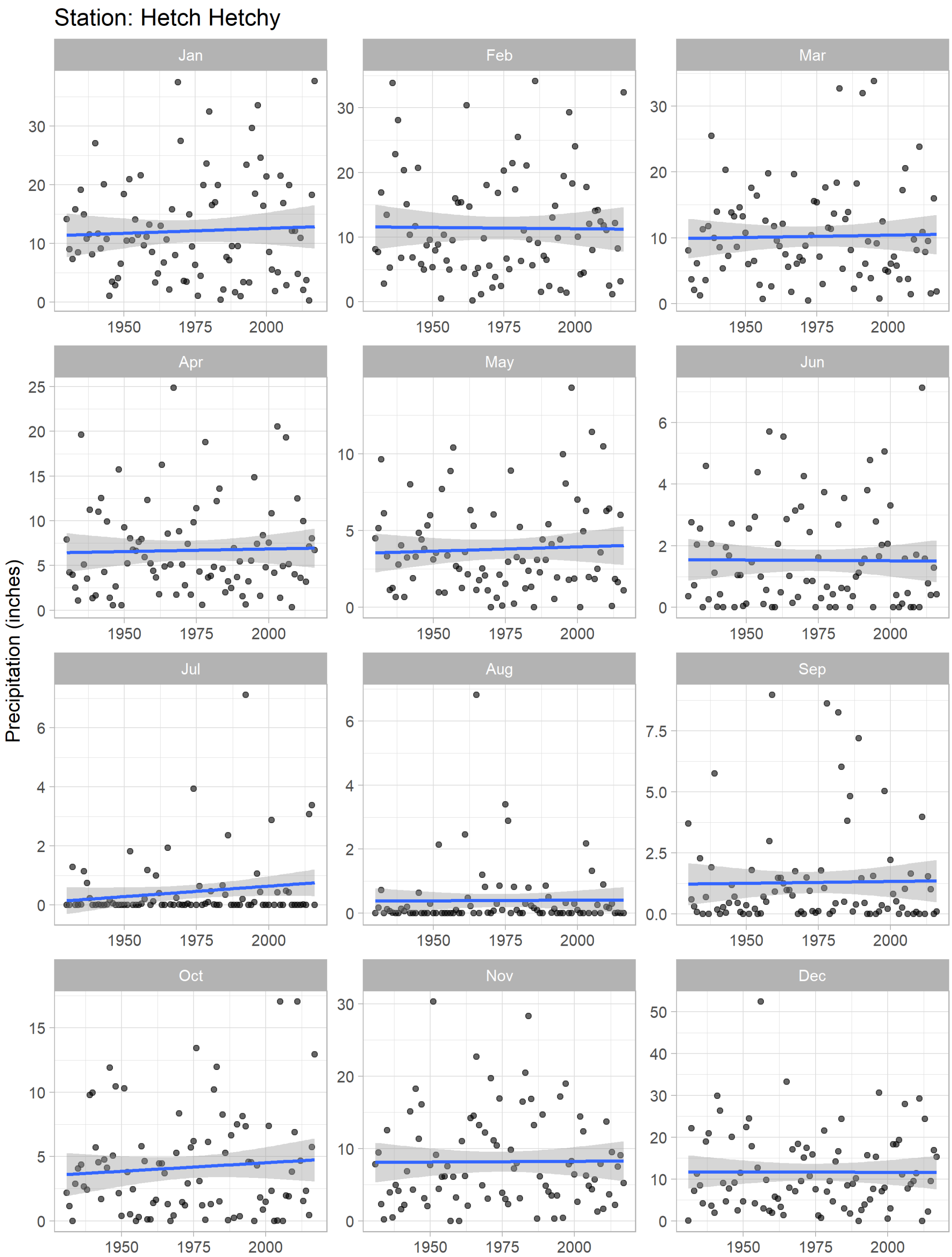

Station: Hetch Hetchy
Precipitation (inches)
Jan
Feb
Mar
Apr
May
Jun
Jul
Aug
Sep
Oct
Nov
Dec
0
10
20
30
0
5
10
15
20
25
2
4
6
2.5
5.0
7.5
0.0
40
50
1950
1975
2000

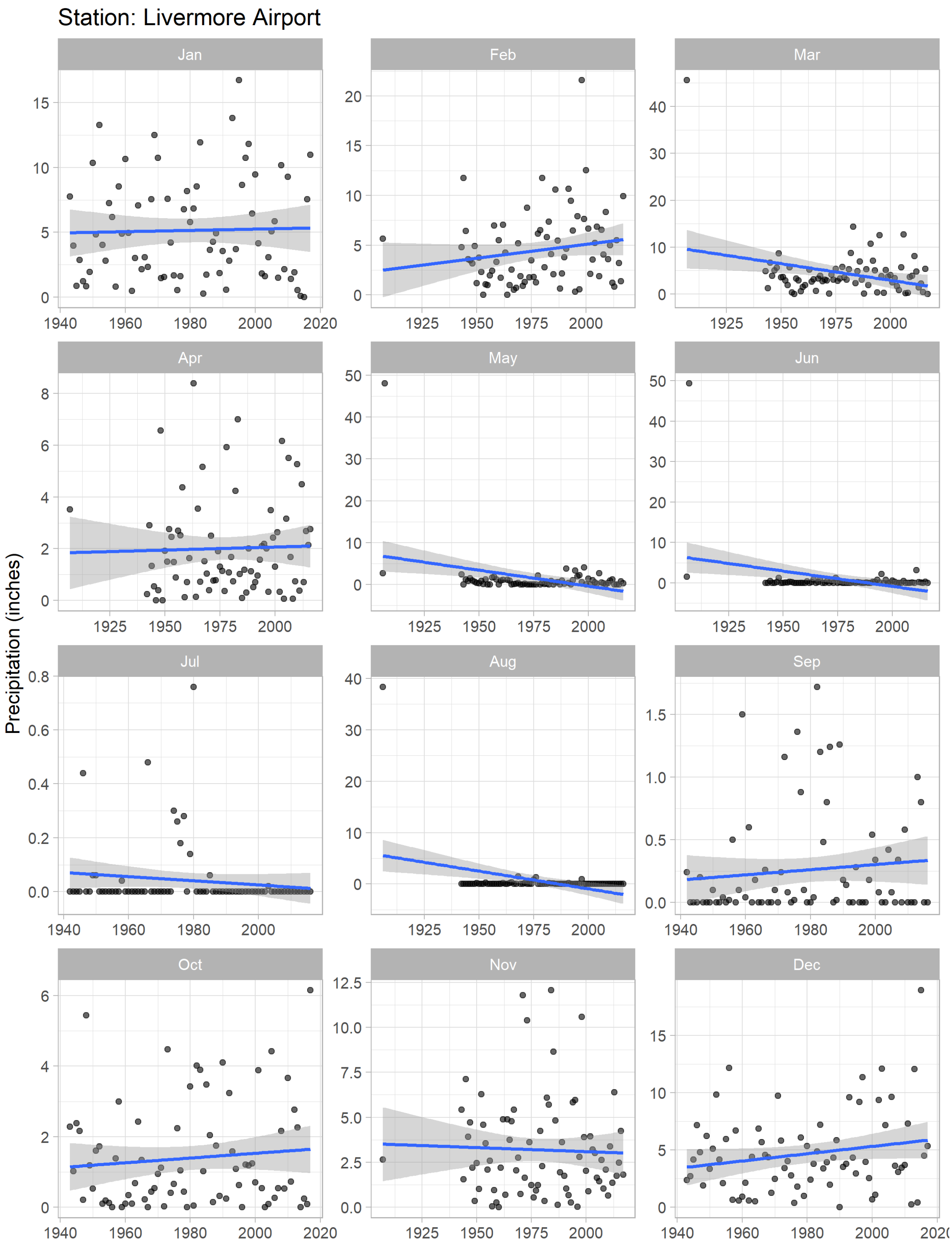
Station: Livermore Airport
Precipitation (inches)
Jan
Feb
Mar
Apr
May
Jun
Jul
Aug
Sep
Oct
Nov
Dec
0
5
10
15
20
30
40
50
0.0
0.2
0.4
0.6
0.8
0.5
1.0
1.5
2
4
6
8
2.5
5.0
7.5
10.0
12.5
1925
1940
1950
1960
1975
1980
2000
2020

Station: Moccasin

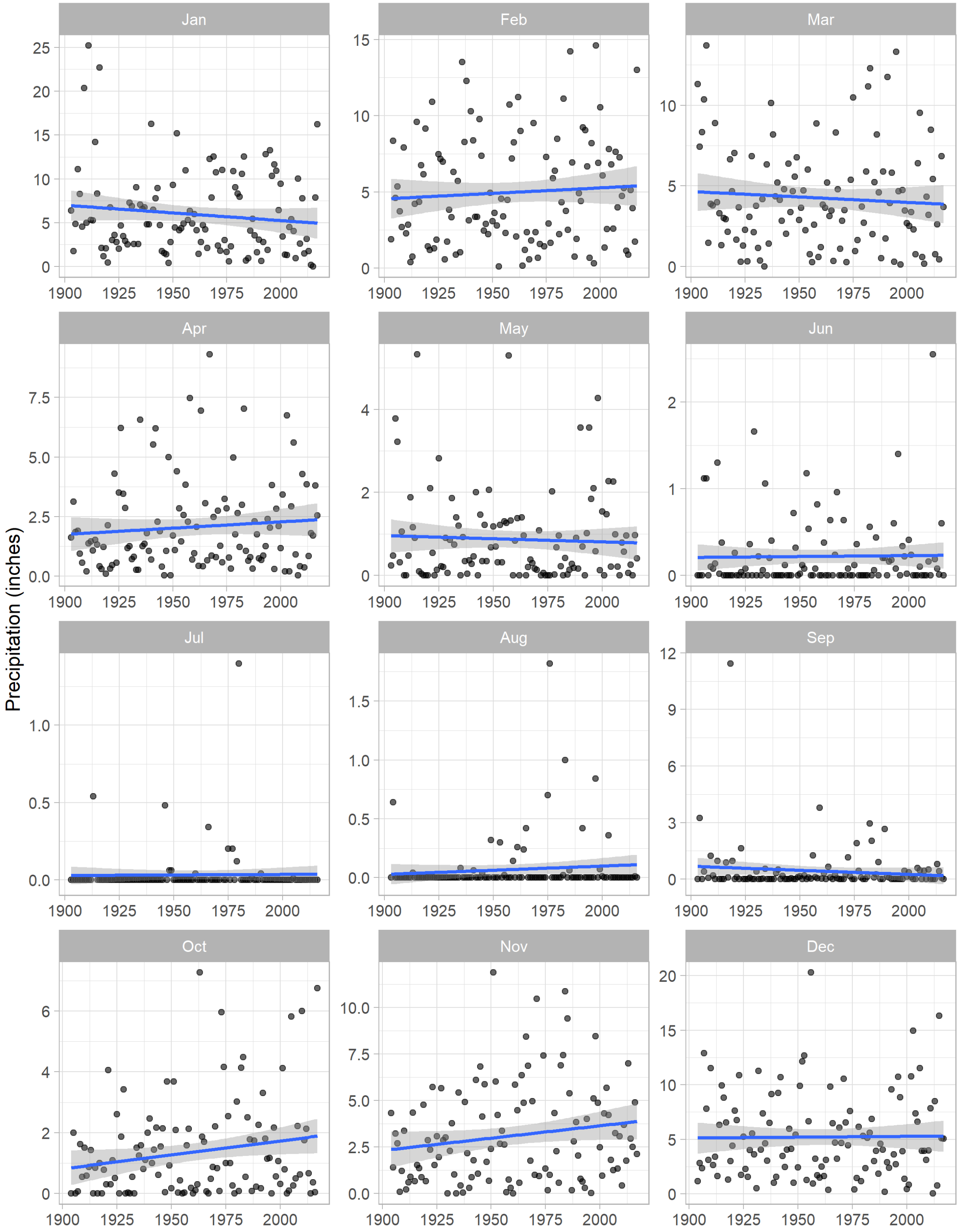

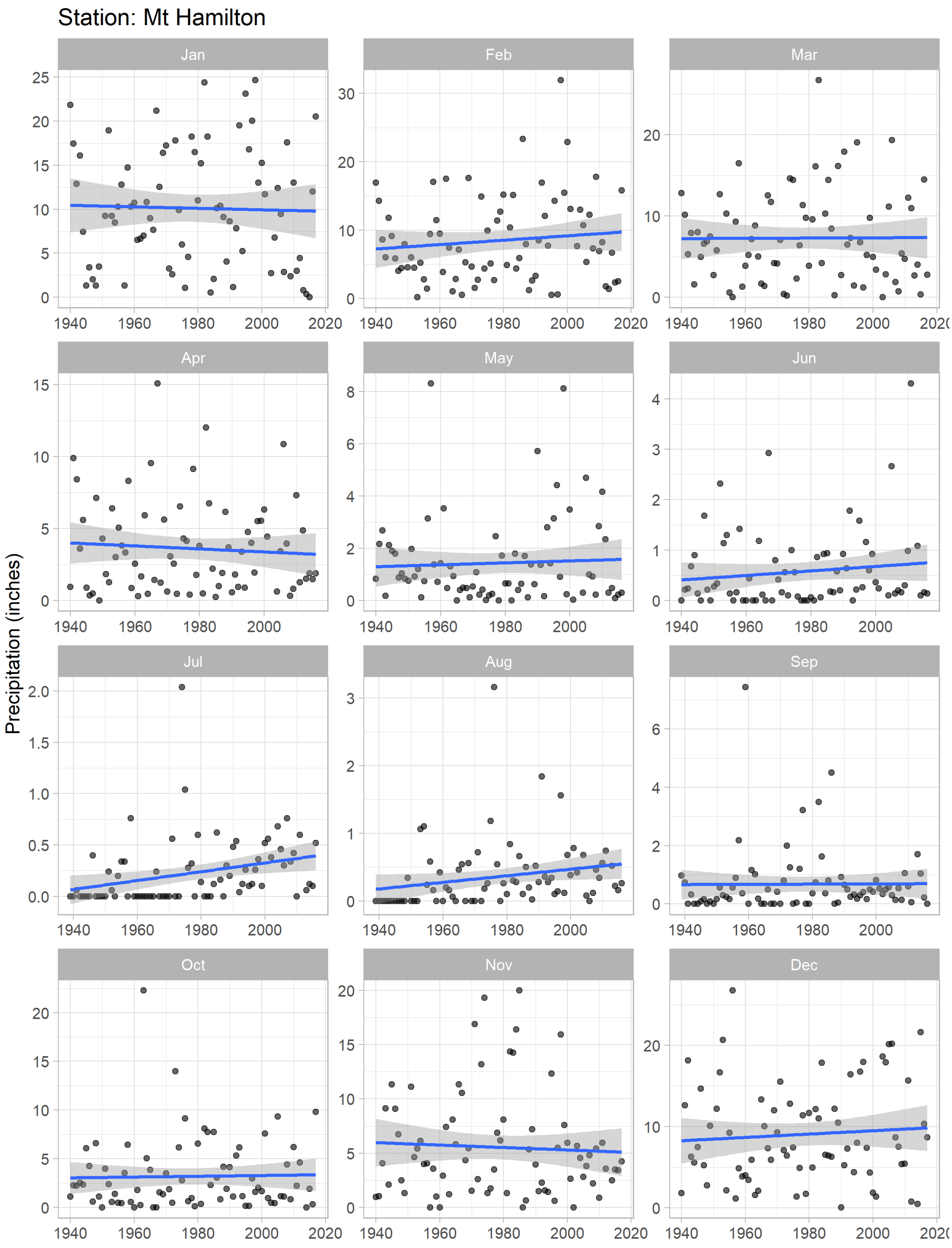
Station: Mt Hamilton
Precipitation (inches)
Jan
0
5
10
15
20
25
1940
1960
1980
2000
2020
Feb
0
10
20
30
1940
1960
1980
2000
2020
Mar
0
10
20
1940
1960
1980
2000
2020
Apr
0
5
10
15
1940
1960
1980
2000
May
0
2
4
6
8
1940
1960
1980
2000
Jun
0
1
2
3
4
1940
1960
1980
2000
Jul
0.0
0.5
1.0
1.5
2.0
1940
1960
1980
2000
Aug
0
1
2
3
1940
1960
1980
2000
Sep
0
2
4
6
1940
1960
1980
2000
Oct
0
5
10
15
20
1940
1960
1980
2000
2020
Nov
0
5
10
15
20
1940
1960
1980
2000
2020
Dec
0
10
20
1940
1960
1980
2000
2020

Station: Poverty

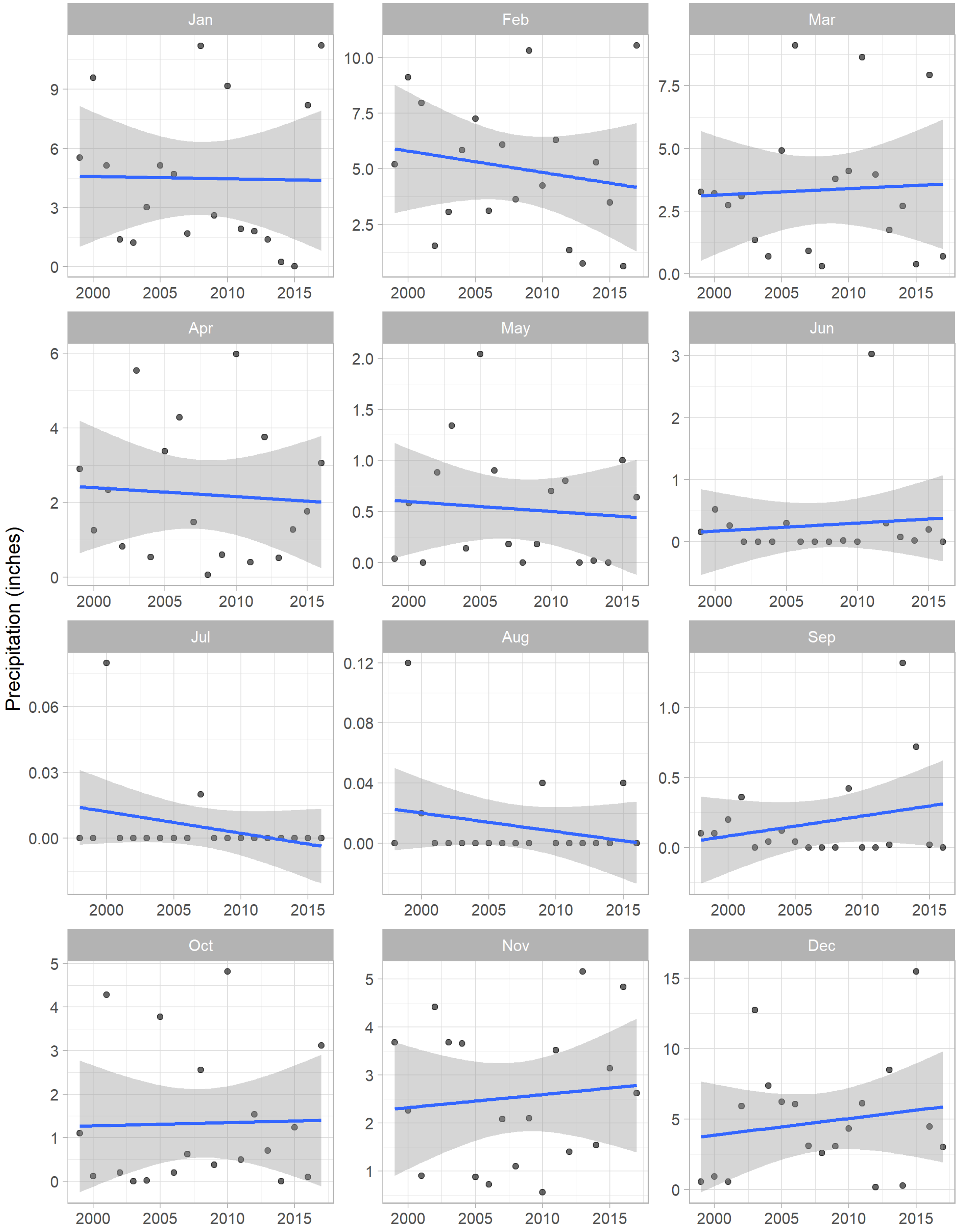

Station: Rose Peak

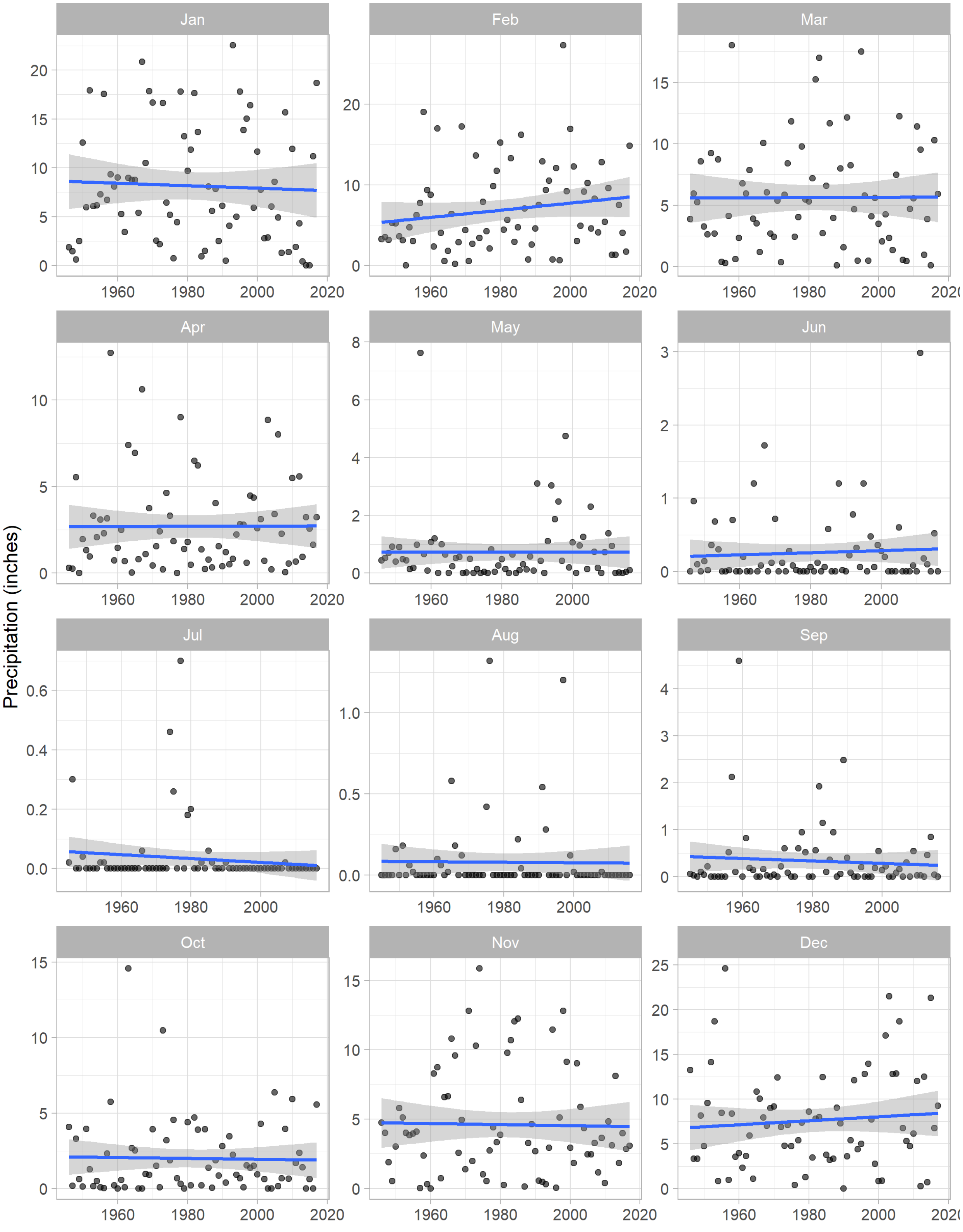

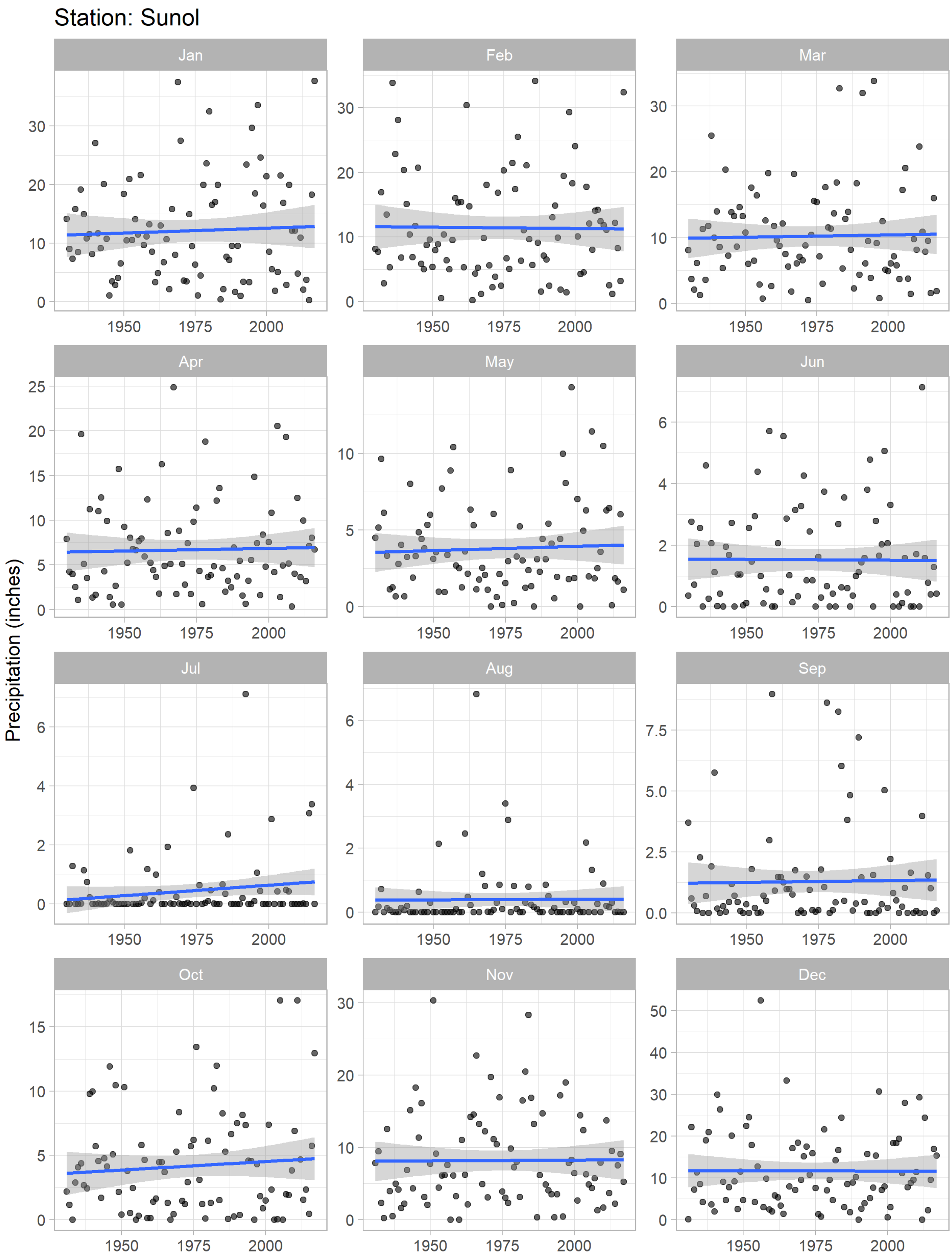
Station: Sunol
Precipitation (inches)
Jan
30
20
10
0
1950
1975
2000
Feb
30
20
10
0
1950
1975
2000
Mar
30
20
10
0
1950
1975
2000
Apr
25
20
15
10
5
0
1950
1975
2000
May
10
5
0
1950
1975
2000
Jun
6
4
2
0
1950
1975
2000
Jul
6
4
2
0
1950
1975
2000
Aug
6
4
2
0
1950
1975
2000
Sep
7.5
5.0
2.5
0.0
1950
1975
2000
Oct
15
10
5
0
1950
1975
2000
Nov
30
20
10
0
1950
1975
2000
Dec
50
40
30
20
10
0
1950
1975
2000

Station: San Jose

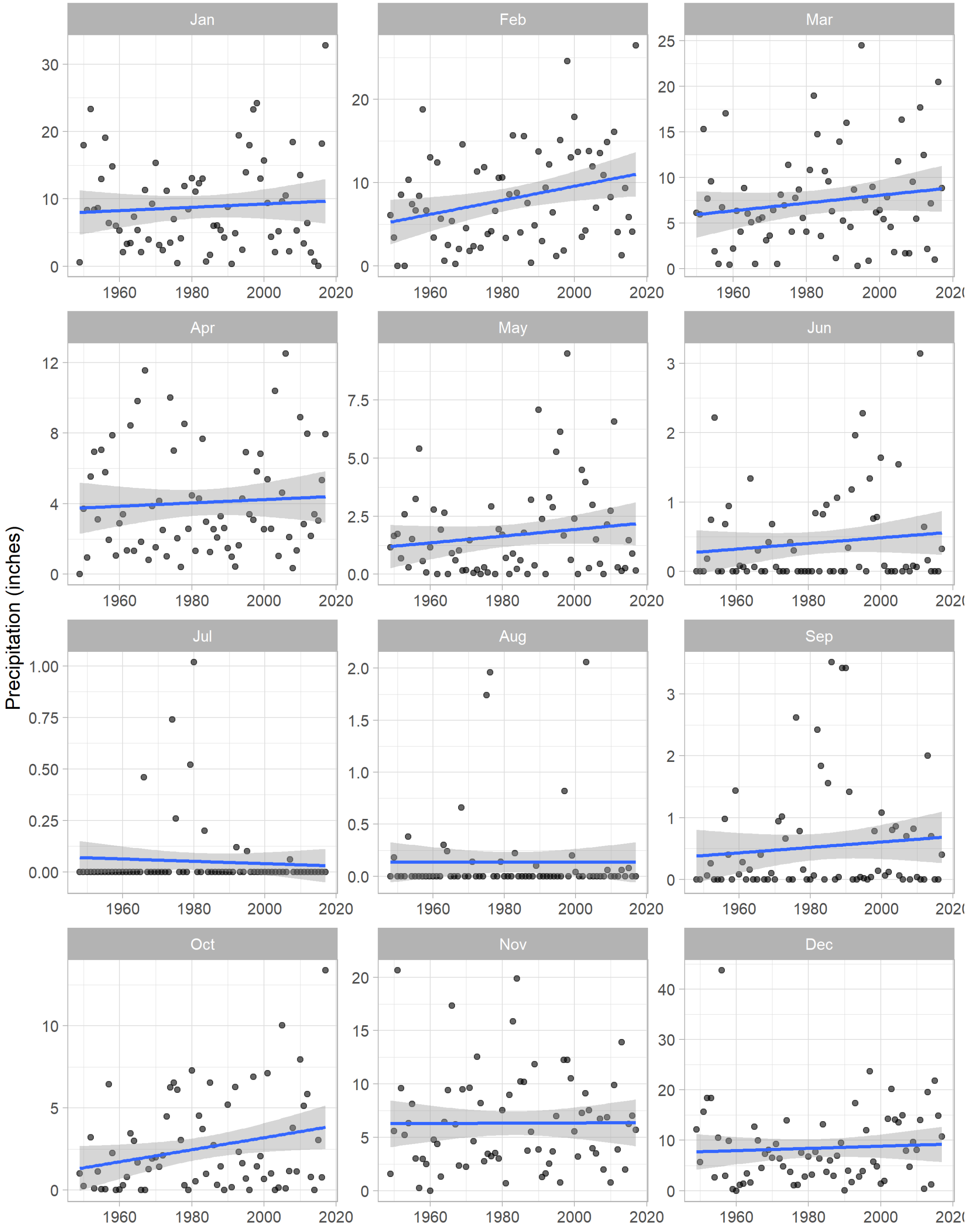

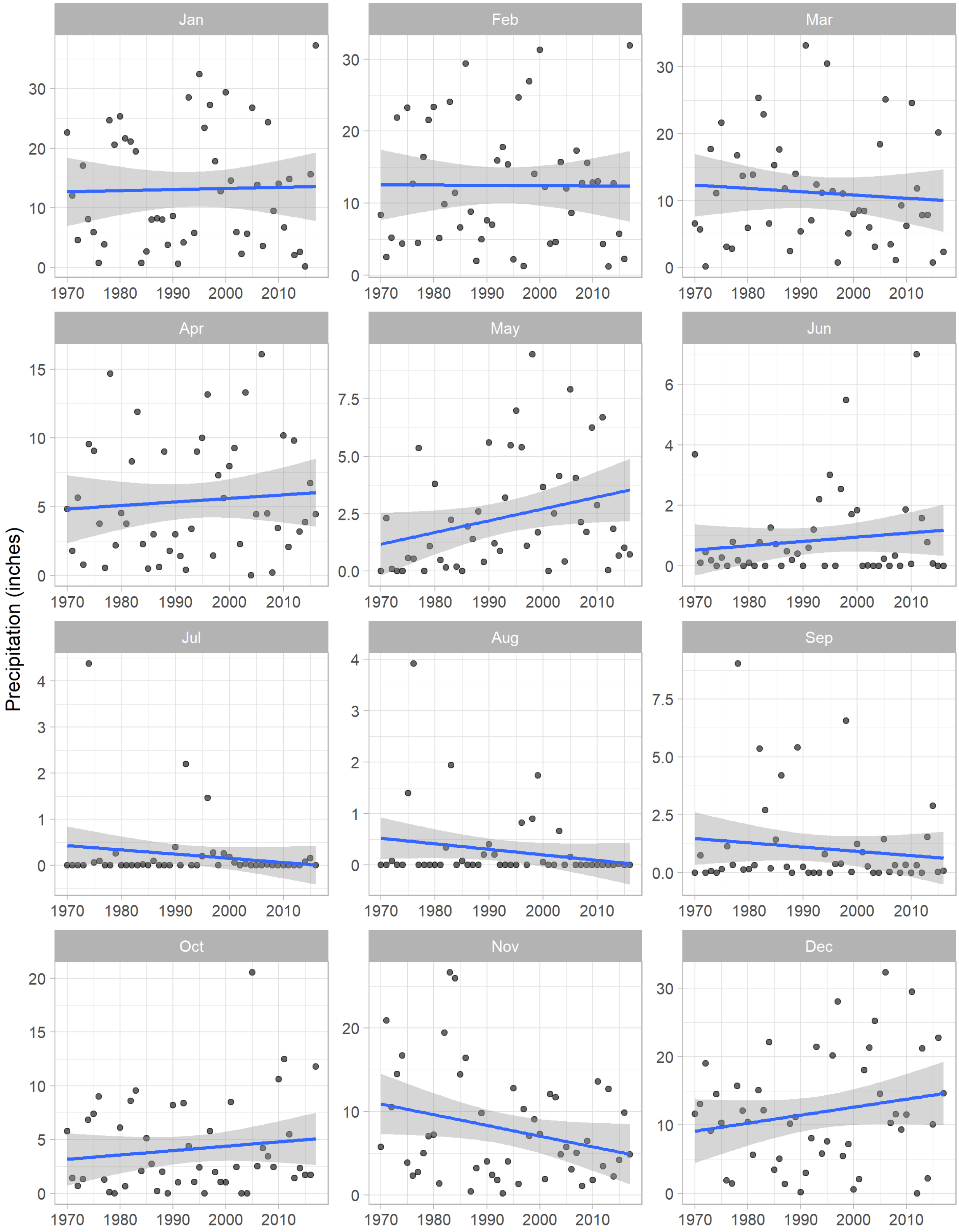

Station: Tuolumne Meadows